5-2017

Multidisciplinary Shape Optimization of A Composite Blended Wing Body Aircraft

Charles Maxwell Boozer
University of South Carolina

MULTIDISCIPLINARY SHAPE OPTIMIZATION OF A COMPOSITE BLENDED WING BODY AIRCRAFT

by

Charles Maxwell Boozer

Bachelor of Science
University of South Carolina, 2014

Submitted in Partial Fulfillment of the Requirements

For the Degree of Master of Science in

Aerospace Engineering

College of Engineering and Computing

University of South Carolina

2017

Accepted by:

Michel J. L. van Tooren, Director of Thesis

Tanvir I. Farouk, Reader

Ramy Harik, Reader

Cheryl L. Addy, Vice Provost and Dean of the Graduate School

ACKNOWLEDGEMENTS

The work presented here is in thanks to the support and academic and professional opportunities provided to me by Dr. van Tooren. With his help, I was fortunate to study the field of my choice and explore a new engineering discipline. I also thank Dr. Elham for mentoring me at the Delft University of Technology during my time abroad. Finally, I thank my family, friends, and colleagues for their continued support throughout my academic career.

ABSTRACT

A multidisciplinary shape optimization tool coupling aerodynamics, structure, and performance was developed for battery powered aircraft. Utilizing high-fidelity computational fluid dynamics analysis tools and a structural wing weight tool, coupled based on the multidisciplinary feasible optimization architecture; aircraft geometry is modified in the optimization of the aircraft's range or endurance. The developed tool is applied to three geometries: a hybrid blended wing body, delta wing UAS, the ONERA M6 wing, and a modified ONERA M6 wing. First, the optimization problem is presented with the objective function, constraints, and design vector. Next, the tool's architecture and the analysis tools that are utilized are described. Finally, various optimizations are described and their results analyzed for all test subjects. Results show that less computationally expensive inviscid optimizations yield positive performance improvements using planform, airfoil, and three-dimensional degrees of freedom. From the results obtained through a series of optimizations, it is concluded that the newly developed tool is both effective at improving performance and serves as a platform ready to receive additional performance modules, further improving its computational design support potential.

TABLE OF CONTENTS

LIST OF TABLES

LIST OF FIGURES

LIST OF SYMBOLS

α	Geometric angle of attack [degrees]
β^2	Artificial compressibility parameter
δ	Kronecker delta function
η_{total}	Total efficiency
Λ	Leading edge sweep angle [degrees]
v	Kinematic viscosity [Pa·s]
ρ	Density [kg/m^3]
∞	Subscript denoting freestream value for fluid properties
A	Optimization constant
AR	Wing aspect ratio
b	Wing span [m]
c	Design constraint(s)
c	Airfoil chord [m]
c_r	Wing root chord [m]
c^c	Consistency constraint(s)
C	Specific fuel consumption
C_{batt}	Battery capacity [Ah]
C_D	Drag coefficient
C_f	Skin friction coefficient
C_L	Lift coefficient

C_M Moment coefficient

D Drag force [N]

E Endurance [h]

E^* Mass specific energy content [Wh/kg]

$\boldsymbol{FFD}$ Vector of freeform deformation control point displacements

Fr Froude number

g Acceleration due to gravity [m/s^2]

J Objective function

L Lift force [N]

m Mass of aircraft [kg]

m_{batt} Mass of battery [kg]

M Mach number

M_y Pitching moment [Nm]

n_{batt} Number of individual battery cells

P Pressure [Pa]

P_{avail} Power available [W]

P_{req} Power required [W]

q Dynamic pressure [Pa]

R Range [km]

Rt Battery hour rating [h]

S Wing reference area [m^2]

t Airfoil thickness [m]

u x-component of velocity [m/s]

u_τ	Friction velocity [m/s]
U	Conservative vector
S_{wet}	Wetted wing area [m^2]
v	y-component of velocity [m/s]
V	Flow velocity [m/s]
V_{batt}	Battery output power [V]
w	z-component of velocity [m/s]
W	Gross weight [N]
$\boldsymbol{x}$	Design vector
$\boldsymbol{y}$	Coupling vector
y	Dimensional wall distance [m]
$\widehat{\boldsymbol{y}}$	Copies of the coupling variable(s)
y^+	Wall unit

LIST OF ABBREVIATIONS

AVL ..... Athena Vortex Lattice

BWB ..... Blended Wing Body

CFD ..... Computational Fluid Dynamics

CFL ..... Courant–Friedrichs–Lewy

CST ..... Class Shape Transformation

DNS ..... Direct Numerical Simulation

EMWET ..... Elham Modified Weight Estimation Technique

FFD ..... Free-Form Deformation

IDF ..... Individual Discipline Feasible

LES ..... Large Eddy Simulation

MAC ..... Mean Aerodynamic Chord

MDF ..... Multidisciplinary Feasible

MDO ..... Multidisciplinary Design Optimization

MTOW ..... Maximum Take-Off Weight

RANS ..... Reynolds-Averaged Navier-Stokes

Re ..... Reynolds number

SA ..... Spalart-Allmaras

SST ..... Menter Shear Stress Transport

SU2 ..... Stanford University Unstructured

UAS ..... Unmanned Aerial System

UCAV ..... Unmanned Combat Aircraft Vehicle

XDSM .....Extended Design Structure Matrix

CHAPTER 1

INTRODUCTION

Unconventional aircraft configurations are appearing more and more over the conventional tube-and-wing design, especially in unmanned aerial systems (UAS). Many of these configurations represent blended wing bodies (BWB) and non-slender delta wings. Several examples of larger UAS include Boeing's X-45, BAE Systems' Taranis, and Lockheed Martin's UCLASS, which are unmanned combat aircraft vehicles (UCAV) from the defense industry and smaller UAS include AgEagle's AgEagle and senseFly's eBee, which are unmanned observation drones for monitoring land, such as large farms. Companies including Boeing [1] and Airbus [2] have also investigated BWB configurations as an alternative to the conventional tube-and-wing design for large passenger and transport aircraft. These unconventional configurations have improved aerodynamic properties, but are hindered by instabilities and their difficulty to be designed.

1.1 AIRCRAFT DESIGN

There are three main phases for aircraft design: conceptual, preliminary, and detailed. During the conceptual design phase, the aircraft continuously evolves through exploration of design alternatives and trade studies. By the end of conceptual design, the primary unknowns of the aircraft's configuration and performance have been determined. The preliminary design phase marks the period after the conceptual phase and is when discipline specific design and analyses are performed. In this phase, the quantitative values of the aircraft's defining parameters are decided and the aircraft is lofted: when the outer

surface is mathematically modelled to sufficient accuracy [3]. Finally, in the detailed design phase, the aircraft configuration is completed, down to the size and position of the fasteners.

Aircraft design, especially wing design, is a complex task due to the tight coupling of several engineering disciplines: aerodynamics, structures, propulsion, and controls. The shape of the aircraft must provide favorable aerodynamic performance and allow structural integrity for acceptable cost and weight, and most importantly, provide enough lift for the aircraft. To quantify the required lift, the weight of the aircraft needs to be known and is strongly influenced by the structural weight. The aircraft structure depends on the loads it must resist and the shape the structure is contained within, causing the weight to change for each aerodynamic shape. The structure also deforms due to the aerodynamic loads, e.g. the wingtips deflecting upwards and twisting during flight changes the effective aerodynamic shape leading to different lift distributions and potentially different stall behavior. Lastly, control surface dimensions depend on the size of the wing, weight of the aircraft, and local flow characteristics. Simply, aircraft design is an iterative task and the design problem can have many possible solutions. The individual disciplines, large number of parameters, and iterative nature make aircraft design especially difficult, time-consuming, and an excellent opportunity to implement optimization techniques to support exploration of the design domain.

1.2 BLENDED WING BODIES AND DELTA WINGS

1.2.1 Configuration

The BWB configuration is characterized by airfoil-shaped fuselage and wings that are blended into a single body, creating a near seamless outer shape that integrates payload

accommodation, lifting surface, propulsion system, and control surfaces. The BWB concept has several superior aerodynamic characteristics over conventional aircraft layouts. Most notably, the BWB concept reduces wetted surface area which reduces skin friction drag. Wing loading is reduced for BWB configurations because the fuselage produces lift along with the wings, providing a more continuous spanwise lift distribution. The reduced wing load offers improved stall characteristics, making heavy high-lift devices redundant [4]. These advantages culminate into a more energy efficient aircraft at the cost of a stability penalty.

The aircraft studied in this work, the VX KittyHawk, also has characteristics of a non-slender delta wing. Delta wings come in a variety of configurations, but typically have high sweep angles, sharp leading edges, and allow flight in supersonic conditions as well as deliver enough lift at low speed flight. Non-slender delta wings are delta wings with a leading edge sweep angle less than 60° [5]. Delta wings benefit from vortex lift at increased angles of attack, allowing them to achieve higher lift coefficients at higher angles of attack, where many conventional wings would stall.

1.2.2 Aerodynamic Challenges

Both BWB and non-slender delta wing configurations present challenges typically not met in the standard tube-and-wing design. BWBs lack a horizontal stabilizer, presenting stability issues such that the pitching moment must be controlled in another way. The aircraft can be trimmed, but this may lead to a large trim drag depending on the strength of the pitching moment. As a solution, the BWB airfoil sections may be designed with a reflexed camber along the latter portion of the chord. Trimming the aircraft with

trailing edge devices change the overall camber, influencing the drag and pitching moment much more than an elevator mounted on a horizontal tail plane.

The flow over delta wings can differ greatly from wings with little or no sweep, primarily due to the formation of leading edge vortices. The strong leading edge vortices cause reduced surface pressure along the leading edges of the upper surface, generating an increase in lift. This increase in lift also carries a drag penalty like wing tip vortices [6]. While the flow over delta wings differ from non-swept wings and wings with low sweep, it is also significantly different from that of non-slender delta wings [7]. The primary vortex on non-slender delta wings has a stronger effect on the wing boundary layer than slender delta wings and can affect the stall modes. More information regarding the stall phenomena of non-slender delta wing can be found in References [5], [8], and [9]. Verhaagen [5] also shows that the leading edge radius of delta wings, typically sharp, is also a key factor as to how the flow behaves. Finally, there has also been less research focused on the flow phenomena over subsonic non-slender delta wings, making this area of research relatively immature.

1.3 MULTIDISCIPLINARY DESIGN OPTIMIZATION

Multidisciplinary design optimization (MDO) is a field of engineering that focuses on the use of numerical optimization techniques from calculus, operations research, and other related fields of mathematics and computer science to solve and support solutions of the design problem for multidisciplinary systems. Using computational optimization tools, the design space, easily consisting of tens or hundreds of design variables, can be explored quickly and accurately. Optimization tools can be used for almost any discipline of aircraft design, including aerodynamics, propulsion, structures, and performance. The greatest

benefit is achieved when the disciplines are analyzed together, due to their coupled nature. The simultaneous multidisciplinary capabilities of MDO make it the preferred choice of computational design support, especially during the preliminary design phase.

1.4 DESIGN PROBLEM

Many of the small and large UAS described earlier share similar design requirements: they must have enough range to reach their target or observation zone and they must have enough endurance to observe their target or maintain air presence. Each aircraft's mission is different; thus, they have specific range and endurance requirements. An aircraft that is deployed near its target may need less range and the design can be focused on increasing its observation endurance at a specific velocity to avoid detection. An aircraft that is deployed far from its target, for instance, a military UCAV as described above, may have to travel long distances to cross ocean and country borders and range becomes the key factor.

For each aircraft, optimal range and endurance flight conditions can be established. Figure 1.1 shows examples of drag versus velocity and power required versus velocity plots and the maximum range and endurance locations. For propeller aircraft, the maximum range occurs at the velocity in which the drag is minimum. The minimum drag condition can be related to power required from the power required versus flight velocity graph by a line drawn through the origin and its point of tangency on the power required curve. Maximum endurance occurs at the velocity in which the power required is minimum. For an existing aircraft, this means changing parameters such as flight speed or altitude to modify the operating conditions to that for maximum performance. During the design phase, one has the capability to tailor the aircraft parameters to operate at the optimal

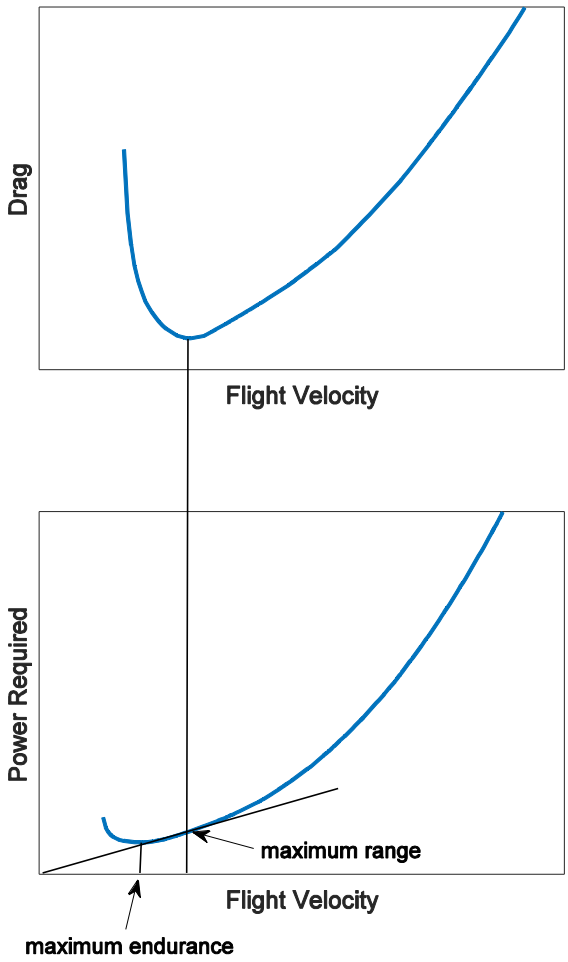

Figure 1.1 Relationship between drag, power, endurance, and range.

conditions. This is especially helpful when there are constraints on the available propulsion system or flight speed.

1.5 OBJECTIVE OF WORK AND RESEARCH GOALS

The objective of this work is to develop a MDO tool to optimize range or endurance performance of battery powered aircraft during the preliminary design phase and to utilize that tool to perform optimization of a composite, blended wing body aircraft. Secondary objectives include observing the effects of specific design variables and parameters including planform, airfoil, and fully three-dimensional.

1.6 THESIS OUTLINE

The thesis is structured as follows: Chapter 2 discusses the definition of the MDO problem and the optimization architecture for the tool. Chapters 3 describes the analysis tools and hardware used for analyses and is concluded with a detailed workflow of the completed MDO tool. Chapter 4 describes the key inputs for the MDO tool, and how they were chosen. In Chapter 5, the MDO tool is applied to three test geometries, the KittyHawk, the ONERA M6, and a modified ONERA M6 and the optimization results are discussed and compared. Finally, Chapter 6 holds the conclusions of the work and plans for future work.

CHAPTER 2

MDO PROBLEM DEFINITION AND TOOL DEVELOPMENT

MDO problem formulation is marked by the selection of several components including the discipline analyses, the optimization framework, the algorithm driving the optimization, the objective function, (the function to be optimized), constraint functions, and the design space in which the problem is defined. The methods used to define, structure, and solve the MDO problem in this work are described in this chapter.

2.1 OBJECTIVE FUNCTION

Perhaps the most crucial element of an optimization problem is the objective or cost function which defines what is being optimized. As stated in Section 1.5, the optimization performed is intended to improve endurance or range for a battery powered UAS, thus the objective function is defined by either endurance or range.

Range (R) for liquid fuel based aircraft can be computed using:

$$R = \int_{W_i}^{W_f} -\frac{V_\infty}{CW}\left(\frac{L}{D}\right) dW \tag{2.1}$$

where W is the gross weight of the aircraft, C is the specific fuel consumption, V_∞ is the freestream velocity, L and D are the lift and drag forces, and the subscripts i and f represent initial and final respectively [3]. It is easily recognized that for a battery powered aircraft, which does not change gross weight during flight due to fuel burn, Eq. (2.1) cannot be used since the initial and final weights are identical. Assuming a constant flight speed, endurance

(E) is simply range divided by the freestream velocity, however, the optimal conditions or configuration for endurance may not be the same for range.

$$E = \frac{R}{V_\infty} = \int_{W_i}^{W_f} -\frac{1}{CW}\left(\frac{L}{D}\right) dW \tag{2.2}$$

An alternative formulation for range, specific to battery powered aircraft, was obtained from the work of Hepperle [10] and is as follows:

$$R = E^* \cdot \eta_{total} \cdot \frac{1}{g} \cdot \frac{L}{D} \cdot \frac{m_{batt,total}}{m}$$
$$\text{where} \qquad E^* = \frac{V_{batt} \cdot C_{batt}}{m_{batt}} \tag{2.3}$$

In Eq. (2.3) m is the total mass of the aircraft and the battery parameters are: E^*, the battery's mass specific energy content, m_{batt}, the battery's mass, V_{batt}, the battery output power, and C_{batt}, the battery capacity. η_{total} is the total efficiency of the propulsion system. The subscript *total* represents the total mass of all the individual battery packs. m_{batt}, V_{batt}, C_{batt}, and, η_{total}, come from the product manufacturers and performance testing and are kept constant during the optimization. Grouping the constants together and nondimensionalizing the aerodynamic forces to obtain their coefficients (C_L and C_D), Eq. (2.3) is rewritten as:

$$R = A_R \cdot \frac{1}{W} \cdot \frac{C_L}{C_D}$$
$$\text{where} \qquad A_R = E^* \cdot \eta_{total} \cdot m_{batt} \tag{2.4}$$

The definitions of the lift and drag coefficients are as follows, where q is the dynamic pressure, S is the wing reference area, and ρ is the density of the flow.

$$C_L = \frac{L}{qS} \tag{2.5a}$$

$$C_D = \frac{D}{qS} \tag{2.5b}$$

where $$q_\infty = \frac{1}{2} \cdot \rho_\infty \cdot V_\infty^2 \tag{2.5c}$$

Similarly, for endurance at a constant velocity, Eq. (2.4) can be written as:

$$E = A_E \cdot \frac{1}{W} \cdot \frac{C_L}{C_D}$$

where $$A_E = \frac{E^* \cdot \eta_{total} \cdot m_{batt}}{V_\infty} \tag{2.6}$$

The goal of the optimization is to maximize the aircraft's endurance or range; however, the problem must be posed as a minimization problem. The equations above for range and endurance differ only by the constant factor, *A*, such that the general objective function is:

minimize $$J(C_L, C_D, W) = \frac{W}{A} \cdot \frac{C_D}{C_L} \tag{2.7}$$

where *A* is either A_R or A_E depending on the user's desired optimization. In Eq. (2.7) the lift and drag coefficients are provided by the aerodynamic analysis module and the gross weight is calculated by the weight estimation module, both discussed in Chapter 3.

2.2 CONSTRAINTS

Several constraints were considered to solve the optimization problem, including two inequality constraints and one equality constraint. Equality constraints are more difficult to satisfy since the solution must fall onto a specified line, rather than to one side as for inequality constraints.

The first constraint is that the gross weight of the aircraft must be less than or equal to the maximum take-off weight (MTOW), or:

$$W \leq MTOW \tag{2.8}$$

The second constraint is that the power required (P_{req}) must be less than the power available (P_{avail}). P_{avail} and P_{req} are expressed below where n_{batt} is the number of batteries and Rt is the battery hour rating.

$$P_{avail} = n_{batt} \cdot V_{batt} \cdot \frac{C_{batt}}{Rt} \tag{2.9}$$

$$P_{req} = D \cdot V_{\infty} \tag{2.10}$$

In this optimization, the propulsion system parameters are constants and assumed constant through time, thus power available is constant. This means that the optimizer must manipulate the power required. Since the aerodynamic analysis module provides the drag coefficient, Eq. (2.10) can be rewritten using the definition of the drag coefficient in Eq. (2.5b).

$$P_{req} = q_{\infty} \cdot S \cdot C_D \cdot V_{\infty} \tag{2.11}$$

The wing reference area is obtained from the computational grid surface mesh of the aircraft during the aerodynamic analysis. The second inequality constraint becomes:

$$q_{\infty} \cdot S \cdot C_D \cdot V_{\infty} \leq P_{avail} \tag{2.12}$$

The final constraint is that the lift must equal the gross weight of the aircraft. The optimization is being conducted at the cruise or loiter condition of the aircraft, so this constraint is used to ensure steady, level flight. Using Eq. (2.5a) to obtain lift, the equality constraint is written as:

$$q_{\infty} \cdot S \cdot C_L = W \tag{2.13}$$

2.3 DESIGN VECTOR

The design vector for an optimization problem contains all the design variables, or the parameters that can be manipulated to change the design. Using a simple box for an example, one possible design vector could be the overall length, width, and height. This design vector could effectively control the volume of the box, but allows little overall control of the geometry. For more control over the box, a design vector could include the length of each edge. This design vector would be able to control the size and proportions of the box, but also change the shape entirely. The complexity of a design vector is determined by the requirements of the optimization problem and the control desired by the user.

2.3.1 Shape Parameterization

Controlling the three-dimensional smooth shape of an aircraft is very different from a cube, therefore, shape parameterization becomes useful, if not necessary. Shape parameterization is an important aspect of aerodynamic shape optimization due to the large number of design variables. When performing two-dimensional optimization of a wing, one may look at airfoil sections at specific spanwise locations. These airfoils are commonly defined by hundreds of Cartesian coordinates, where the addition of another airfoil increases the size of the design vector drastically, increasing the number of required computations. Another problem with using these Cartesian coordinates is that it becomes difficult to make smooth changes to the geometry by moving one point at a time. This problem is exacerbated when working with a three-dimensional surface. Shape parameterization techniques parameterize the complex shape of the aerodynamic body into

a smaller number of variables that can be manipulated while ensuring smoothness of the shape being manipulated.

Two forms of shape parameterization were considered for this work: class shape transformation (CST) and free-form deformation (FFD). The CST surface parametrization method can model a wide array of smooth geometries with a small number of equations and parameters. Shapes are classified into different categories based on class functions. The categories form a base from which all other shapes in that class are derived from. The shape function, a set of Bernstein polynomials, determines the specific shape of the geometry within its class as specified by the class function [11], [12]. The airfoil can then be represented by as few or as many CST coefficients as desired, however, it has been found by the author that at least eight coefficients, four on the upper and lower surface each, should be used for accurate results. Some of the most significant advantages of using the CST method is that the derivatives of the shape functions are finite and when plotted, display physical information about the airfoil.

The FFD strategy parameterizes a three-dimensional object as a Bézier solid [13]. Mathematically, the FFD box is defined in terms of a tensor product trivariate Bernstein polynomial, the order of which determines the number of control points on the surface of the box. These control points determine the deformation of the box and the Cartesian coordinates within [14]. The control points replace the Cartesian coordinates of the three-dimensional surface in the design vector. The FFD boxes can make arbitrary changes to the geometrical parameters of the wing such as thickness, sweep, span, chord, etc. Like with the CST method, the FFD shape parameterization method is useful in that the FFD coordinates, as well as the FFD boxes themselves, represent a physical quantity. While the

exact modification to the shape under forced deformation is unknown, the general direction of the deformation can be easily understood.

The FFD method was used as the shape parameterization strategy in this work. The CST method was successfully utilized during early optimizations utilizing two-dimensional airfoil analyses, but the tool was limited to more conventional wing shapes with lower sweep angles and round leading edges. The FFD method was already implemented in the computational fluid dynamics (CFD) tool used in this work, so the migration to the new method was easy. One key note of the FFD's behavior in the CFD tool is that to maintain first or second derivative continuity with intersecting surfaces, the first two rows of control points adjacent to the intersecting plane are frozen. Figure 2.1 shows an example of a non-deformed and deformed FFD box where each intersection of the lattice represents a control point. The lower portion of Figure 2.1 also shows the result of surface intersection, causing the control points to remain stationary.

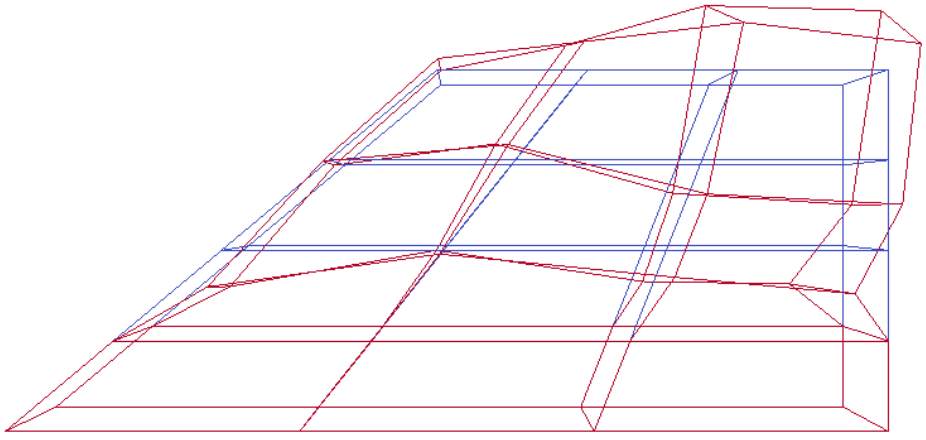

Figure 2.1 Top-down view of a non-deformed (blue) and deformed (red) FFD box.

2.3.2 Design Vector for Multidisciplinary Shape Optimization

The design vector for the problem in this work consists of the FFD box control point displacements in the x, y, and z directions.

$$\boldsymbol{x} = \left[\boldsymbol{FFD}_x, \boldsymbol{FFD}_y, \boldsymbol{FFD}_z\right] \tag{2.14}$$

In Eq. (2.12), $\boldsymbol{x}$ is the design vector comprised of vectors $\boldsymbol{FFD}_x$, $\boldsymbol{FFD}_y$, and $\boldsymbol{FFD}_z$, which are vectors of the x, y, and z-displacements of the FFD control points respectively. The upper and lower bounds of the design vector for the x and y-displacements of the FFD points were set so that two adjacent points could not overlap each other. The bounds are also set to minimize or eliminate the possibility of the lattice faces intersecting the body.

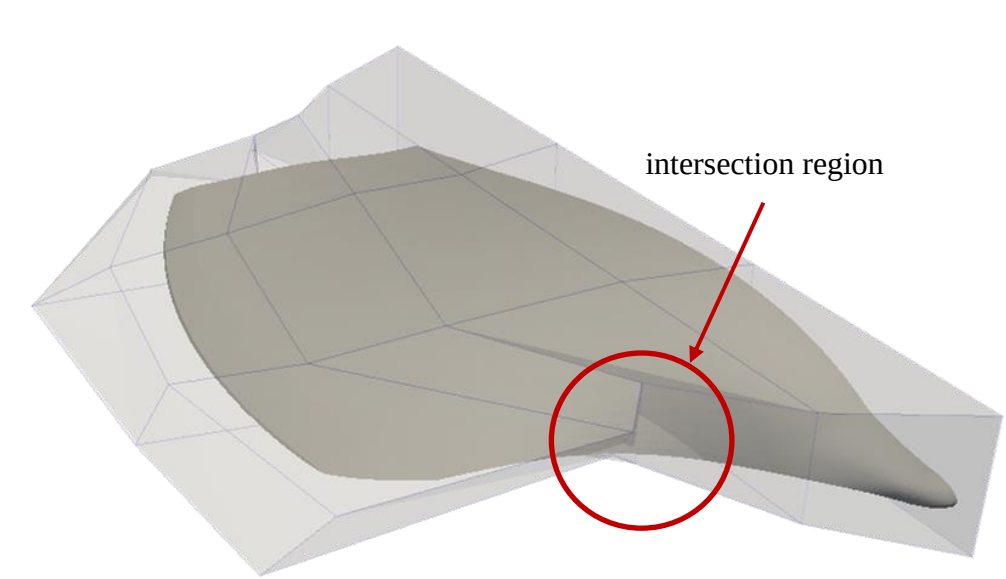

Figure 2.2. Example of a deformed FFD box with an intersecting face.

2.4 THE OPTIMIZATION PROBLEM

With the objective function, design vector, and constraints defined, the final optimization problem can be expressed. Since the objective function and constraints must be a function of the design vector, one additional vector is required. The coupling vector

contains the variables required to model the interactions between disciplines, all of which are functions of the design vector. From Eq. (2.7), Eq. (2.12), and Eq. (2.13), the coupling vector ($\boldsymbol{y}$) is defined as the lift and drag coefficients, the weight, and the wing reference area and is shown below.

$$\boldsymbol{y} = [C_L, C_D, W, S] \tag{2.15}$$

The full MDO problem is finally expressed as:

$$\begin{aligned}
\text{minimize:} \quad & J(\boldsymbol{y}(\boldsymbol{x})) = \frac{W}{A} \cdot \frac{C_D}{C_L} \\
\text{with respect to:} \quad & \boldsymbol{x} = \left[\boldsymbol{FFD}_x, \boldsymbol{FFD}_y, \boldsymbol{FFD}_z\right] \\
\text{where:} \quad & \boldsymbol{y} = [C_L, C_D, W, S] \\
\text{such that:} \quad & c_1 = \frac{W}{MTOW} - 1 \leq 0 \\
& c_2 = \frac{q_\infty \cdot S \cdot C_D \cdot V_\infty}{P_{avail}} - 1 \leq 0 \\
& c^c = \frac{q_\infty \cdot S \cdot C_L}{W} - 1 = 0
\end{aligned} \tag{2.16}$$

In Eq. (2.16), c are design constraints and c^c are consistency constraints.

2.5 GRADIENT-BASED OPTIMIZATION

Gradient-based optimization methods were used to obtain a solution to the problem described above. Gradient-based optimization methods use the objective function and its gradient with respect to the design vector to guide the optimization towards a minimum value. As the name entails, gradient-based methods require the gradients of the functions defining the optimization problem. This is the method's greatest disadvantage, as the derivatives can be difficult to compute efficiently and even be undefined for discrete values or non-continuous objective spaces. However, when considering large numbers of design

variables, as commonly found in aerodynamic shape optimization, gradient-based methods can reach a minimum value in fewer steps than other methods such as grid searching or genetic-based optimization.

2.6 OPTIMIZATION ARCHITECTURES

The MDO architecture is the combination of the problem decomposition and the computational solution scheme. The selection of an MDO architecture is important, as it determines how analyses are performed and how constraints are satisfied. An architecture can be monolithic, where a single optimization problem is solved, or distributed, where the same problem is portioned into multiple sub-problems [15]. All monolithic architectures solve the MDO problem as a single optimization problem, but each one uses a different strategy. Martins and Lambe [15] describe several optimization architectures in their publication, two of which are considered here. In the architectures described below, input variables include the design vector and the copies of the coupling vector ($\widehat{\boldsymbol{y}}$). Design variables and the copies of the coupling variables are controlled by the optimizer.

2.6.1 Individual Discipline Feasible

The Individual Discipline Feasible architecture (IDF) [16] is mathematically expressed as:

$$
\begin{aligned}
\text{minimize} \quad & f_0(\boldsymbol{x}, \boldsymbol{y}(\boldsymbol{x}, \widehat{\boldsymbol{y}})) \\
\text{with respect to} \quad & \boldsymbol{x}, \widehat{\boldsymbol{y}} \\
\text{subject to} \quad & c_0(\boldsymbol{x}, \boldsymbol{y}(\boldsymbol{x}, \widehat{\boldsymbol{y}})) \geq 0 \\
& c_i\big(x_0, x_i, y_i(x_0, x_i, \hat{y}_{j\neq i})\big) \geq 0 \quad \text{for } i = 1, \ldots, N \\
& c_i^c = \hat{y}_i - y_i(x_0, x_i, \hat{y}_{j\neq i}) = 0 \quad \text{for } i = 1, \ldots, N
\end{aligned}
\tag{2.17}
$$

Coupling between the disciplines is enforced by the coupling variable copies and consistency constraints, allowing the discipline analyses to be performed in parallel because they are solved exactly at each iteration. Problems can arise if the number coupling variables become too large, negating the advantages of the IDF architecture. Gradient computation for gradient-based optimization methods can also become an issue when the disciplines are complex due to their increased computational cost.

Below, Figure 2.3 shows the extended design structure matrix (XDSM) for the IDF architecture. Analysis modules are represented by rectangles located along the diagonal of the matrix, with the rounded rectangle being the driver which controls each iteration of the optimization. The gray and black lines represent the data flow and process flow respectively. The other parallelograms represent inputs if the data flow is vertical and outputs if the data flow is horizontal. The white parallelograms denote the initial and optimized variables, variables with superscript *0* and * respectively. More detail can be found in the work of Lambe and Martins [17].

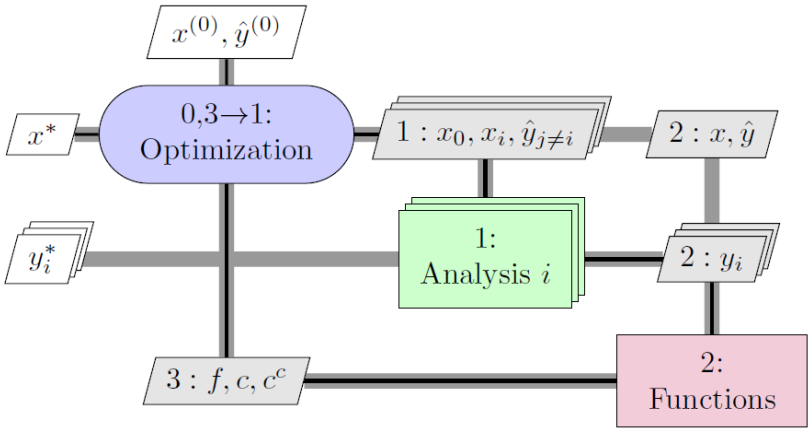

Figure 2.3 XDSM of the IDF architecture [15].

2.6.2 Multidisciplinary Feasible

The Multidisciplinary Feasible (MDF) architecture differs from the IDF architecture by eliminating consistency constraints [16]. In MDF, each discipline is solved in turn using a fixed-point iteration method, which often yields slow convergence rates. This requires that a consistent set of coupling variables be produced and handled by the optimizer every time the objective and constraint functions are re-evaluated. The MDF sensitivities are also coupled, requiring information of one discipline to compute the gradients of the other. However, the MDF problem is as small as possible for a monolithic architecture. MDF also retains inter-disciplinary consistency for every iteration, even when terminated early [15]. The MDF problem statement is expressed below and Figure 2.4 shows the XDSM.

$$\begin{aligned} \text{minimize} \quad & f_0(\boldsymbol{x}, \boldsymbol{y}(\boldsymbol{x}, \boldsymbol{y})) \\ \text{with respect to} \quad & \boldsymbol{x} \\ \text{subject to} \quad & c_0(\boldsymbol{x}, \boldsymbol{y}(\boldsymbol{x}, \boldsymbol{y})) \geq 0 \\ & c_i\big(x_0, x_i, y_i(x_0, x_i, y_{j\neq i})\big) \geq 0 \quad \text{for } i = 1, \ldots, N \end{aligned} \tag{2.18}$$

2.6.3 Architecture Selection

As discussed previously, aerodynamic loading and wing deflection are coupled, as one influences the other. During initial structural studies of the subject aircraft, the required wing-box panel thicknesses were consistently estimated to have the minimum allowed thickness. The trend held true even when the aircraft was subjected to maneuver load factors of 6. These results and the low aspect ratio and robust construction of the BWB delta wing hybrid lead to the conclusion that wing deflection would not be significant during the optimization, and was subsequently eliminated from the problem statement.

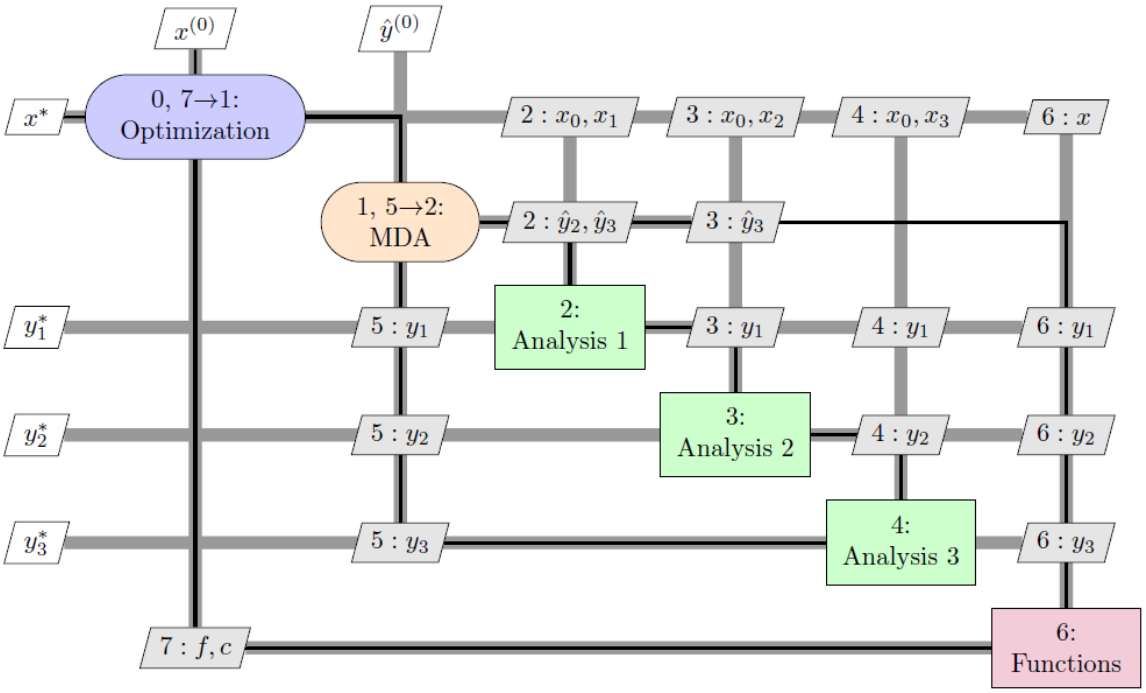

Figure 2.4 XDSM of the MDF architecture [15].

Since wing deflection is not considered, wing deflection coupling variables are not required nor is parallel analysis, thus greatly simplifying the optimization.

The IDF architecture was considered first, but due to the removal of wing deflection and parallel analyses, the architecture simplified to a simple optimization method where the analysis modules were executed sequentially. At the core, the architecture was no longer IDF since parallel analyses were not executed and more closely resembled the MDF architecture without fixed point iteration. With this architecture, the geometric angle of attack (α) was part of the design vector and the optimizer controlled the solution consistency with the consistency constraint, however, the optimizer could not satisfy the equality constraint. Sensitivities were scaled to try and manipulate the optimizer, but it continued to make only small changes to the angle of attack, causing the planform area to decrease to compensate for an excess of lift and to provide a consistent solution.

The architecture used in the current formulation of the tool is based on the MDF architecture. Due to the consistency constraint being eliminated, an additional variable, α, is introduced for the fixed iteration loop. This is controlled by the multidisciplinary analysis driver to obtain a converged solution where the lift of the newly shaped aircraft is equivalent to the weight of the structure required to resist the forces and the fixed weight items such as the propulsion system. Below, Figure 2.5 shows the XDSM for the MDO problem in this work based on the MDF architecture.

2.6.4 Sensitivity Calculation

As explained in Section 2.5, gradient-based optimization requires the computation of derivatives of both the objective function and the constraints. The sensitivity of the objective function with respect to the design vector is expressed using the chain rule as:

$$\frac{dJ}{d\boldsymbol{x}} = \frac{d\boldsymbol{x}}{d\boldsymbol{x}}\frac{\partial J}{\partial \boldsymbol{x}} + \frac{d\boldsymbol{y}}{d\boldsymbol{x}}\frac{\partial J}{\partial \boldsymbol{y}} \tag{2.19}$$

The first two terms in Eq. (2.19) are eliminated since the derivative of $\boldsymbol{x}$ with respect to itself is unity and *J* is not an explicit function of $\boldsymbol{x}$. The third term of Eq. (2.19) can be expanded using Einstein notation as shown below, where it is known that $\partial \boldsymbol{y}/\partial y_i$ is a sparse 1 x *i* vector with the value 1 in the *i*th column, yielding the sensitivity matrix of the coupling variables.

$$\frac{d\boldsymbol{y}}{d\boldsymbol{x}} = \frac{dy_i}{d\boldsymbol{x}}\frac{\partial \boldsymbol{y}}{\partial y_i} = \left[\frac{dC_L}{d\boldsymbol{x}} \quad \frac{dC_D}{d\boldsymbol{x}} \quad \frac{dW}{d\boldsymbol{x}} \quad \frac{dS}{d\boldsymbol{x}}\right] \tag{2.20}$$

The sensitivities of the aerodynamic coefficients are obtained from the aerodynamic analysis tool using the discrete adjoint method while the sensitivities of weight and reference area are obtained using the finite difference method. Like that shown in Eq. (2.20), the final term of Eq. (2.19) can be expanded as shown below. Here, $dy_i/d\boldsymbol{y}$ is

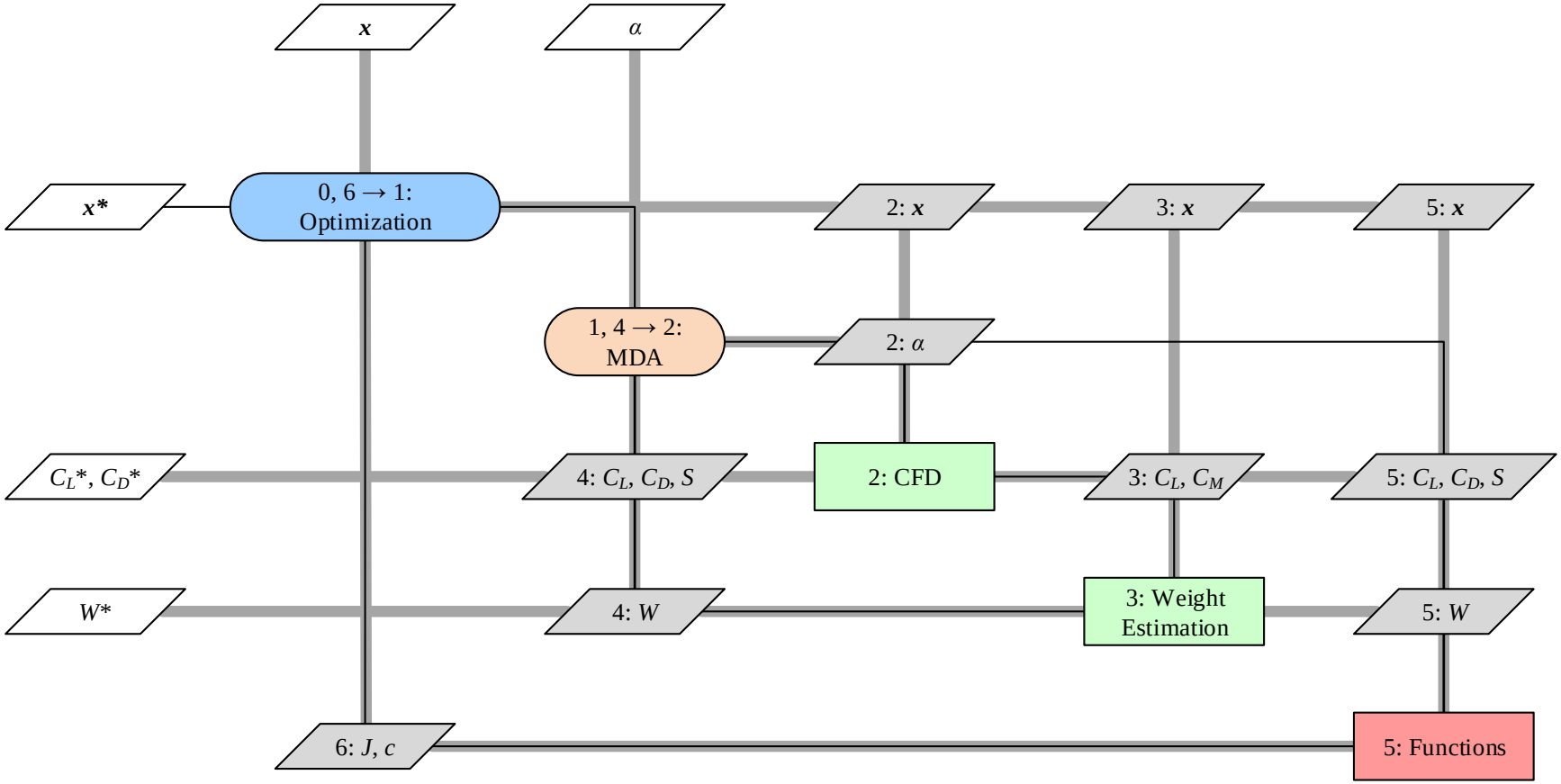

Figure 2.5. XDSM of MDO problem.

exactly the transpose of $\partial \boldsymbol{y}/\partial y_i$, such that

$$\frac{\partial J}{\partial \boldsymbol{y}} = \frac{dy_i}{d\boldsymbol{y}} \frac{\partial J}{\partial y_i} = \begin{bmatrix} \frac{\partial J}{\partial C_L} \\ \frac{\partial J}{\partial C_D} \\ \frac{\partial J}{\partial W} \\ \frac{\partial J}{\partial S} \end{bmatrix} \tag{2.21}$$

Due to the simplicity of the objective function, $\partial J/\partial \boldsymbol{y}$ is easily obtained analytically. The sensitivities of the inequality constraints of Eq. (2.16) share the same form as Eq. (2.19). Since the equality constraint is satisfied differently, only the sensitivities of the aerodynamic coefficients and weight with respect to the angle of attack are required. These sensitivities are obtained with the finite difference method.

CHAPTER 3

COMPUTATIONAL TOOLS

Several computational tools were used in the development of the MDO shape optimization tool and are described in this chapter. The tools include the aerodynamic solvers, the structural analysis tool, the computational software used as the framework for the tool, and the computational hardware used to perform the optimizations.

3.1 AERODYNAMIC ANALYSIS

The choice in aerodynamic analysis tool proved to be a key factor in the optimization of the BWB delta wing UAV. Common tools such as XFOIL [18], a two-dimensional analysis tool, could not cope with the sharp leading edges and slender airfoil sections found on the test subject aircraft. Likewise, while it is not certain whether the vortex lift inherent to delta wings will be present on the KittyHawk operating at low subsonic speeds, it is necessary to be able to resolve the vortex phenomena because of its potentially large influence on performance. The work of Qin et al. [19] shows that while 2D airfoil optimization is beneficial, the results are less significant when considering the 3D problem. Significant 3D effects at areas of high sweep make 3D optimization necessary to obtain the maximum potential from an optimized shape. To determine the significance of the spanwise flow on the KittyHawk, two inviscid simulations were conducted at 0° angle of attack: one of the half the body, using symmetry, and one of a two-dimensional airfoil section at one-quarter of the half-span. Next, the 2D analysis results of airfoil section along the span of the aircraft were compared to results from the 3D analysis at the same

span location. Figure 3.1 shows a comparison of the pressure coefficients at these locations for the 2D and 3D simulations where the section lift coefficient for the 2D analysis was nearly three times that of the 3D analysis. Figure 3.2 shows the surface velocity for the 3D simulation, where the vectors clearly show the spanwise flow, causing the increase in

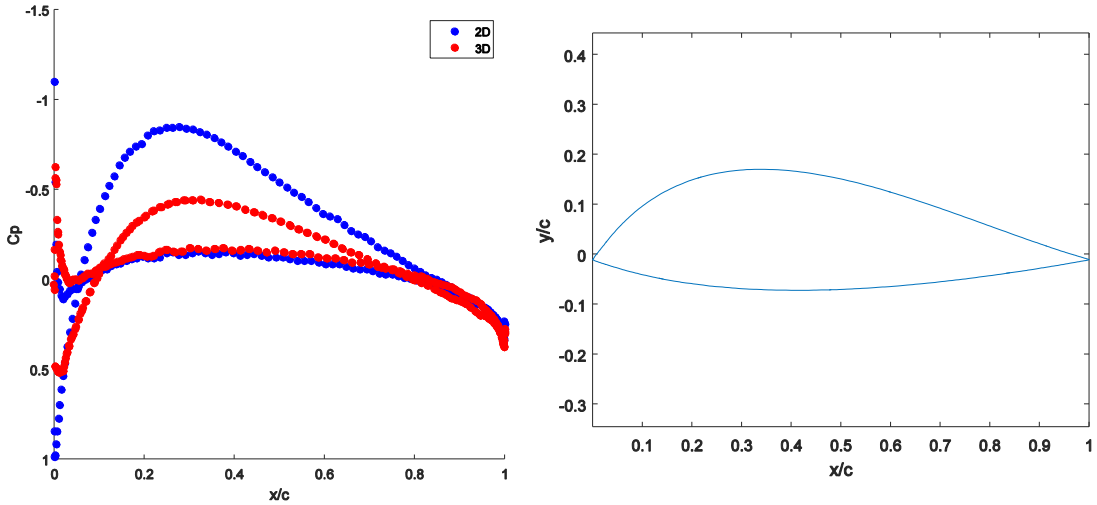

(a) (b)

Figure 3.1 (a) 2D and 3D pressure coefficient comparison for airfoil at y = 0.2125 m. (b) Airfoil section at span position y = 0.2125 m.

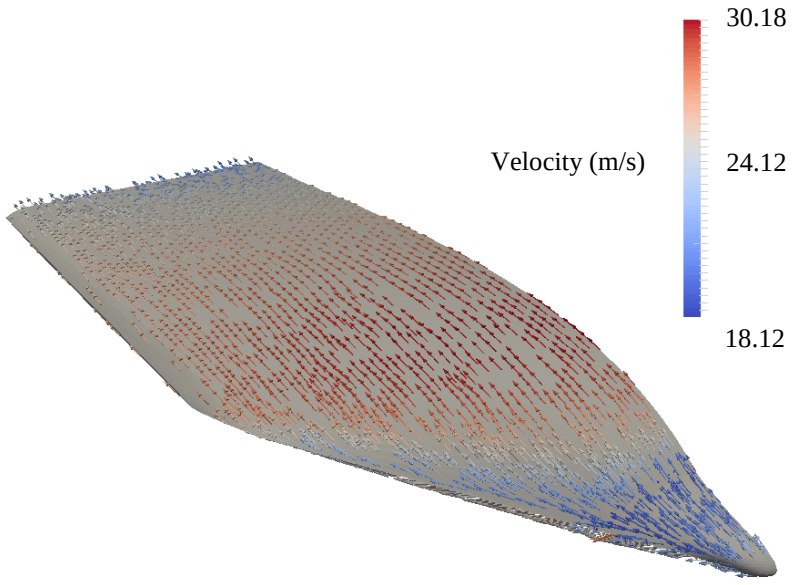

Figure 3.2 Near-surface velocity plot from 3D simulation.

pressure on the upper surface and the overall decrease in lift. The 2D and 3D simulation results shown in Figure 3.1 and Figure 3.2 were obtained using the Stanford University Unstructured CFD suite discussed next.

3.1.1 Stanford University Unstructured

The primary CFD tool used for the aerodynamic analyses in this work is the Stanford University Unstructured tool suite, or SU2. SU2 is a computational analysis and design software collection for solving complex, multiphysics analysis and optimization problems on unstructured meshes. SU2 is comprised of several C++ open-source modules primarily designed for computational fluid dynamics and aerodynamic shape optimization [13].

The version of SU2 used in this work is 4.1.1 “Cardinal” and the utilized modules and their functions of the standard version are described below [20]. SU2 analyzes the full flowfield domain and can resolve leading edge vortices and wake and model turbulence effects. The tool utilizes the FFD shape parameterization method and can perform sensitivity analyses for a number of parameters such as lift, drag, and pitching moment. More detailed information regarding SU2 can be found in References [13], [21], [22], and [23].

- SU2_CFD is the computational fluid dynamics code and can solve the Euler, Navier-Stokes, and Reynolds-Averaged Navier-Stokes (RANS) equations. The finite volume method is used with explicit and implicit time integration methods and can run in serial or parallel.

- SU2_DEF is the mesh deformation code for defining and controlling the free form deformation boxes used for shape parameterization. Manipulation of the volume mesh is performed using the linear spring method.
- SU2_DOT is the gradient projection code used for computing the partial derivative of a functional with respect to variations in the aerodynamic surface.
- SU2_GEO is the geometry definition code for preprocessing and defining the geometry and calculates the geometric constraints for shape optimization.
- SU2_PRT is the domain partitioning code which decomposes the domain for parallel computations.
- SU2_SOL is the solution export code and produces volumetric and surface solution files for third-party post-processing software.

Two additional modules include SU2_CFD_AD and SU2_DOT_AD and are built during compilation of the SU2 source for algorithmic differentiation. These two modules perform the same tasks as their counterparts above, except they perform the sensitivity analysis using the discrete adjoint method. The required inputs for SU2 suite are the unstructured mesh and an extensive configuration file containing all flow, solver, geometry, and gradient details as well as all FFD design variables.

3.1.2 AVL

The Athena Vortex Lattice (AVL) tool [24] was used during the development and debugging phases of the architecture implementation. AVL utilizes an extended vortex lattice method where lifting surfaces are modeled using horseshoe vortices and bodies using lines of sources and doublets [24]. These potential flow features do not account for friction drag, and consequently, there is profile drag caused by separation. While AVL does

not compute viscous drag or consider the entire flowfield, it does consider a three-dimensional, finite body and its induced drag caused by lift generation. This allowed AVL to be used in place of SU2 during the construction of the MDO tool, essentially eliminating computational cost when compared to SU2. The AVL results were not of the highest fidelity, but accuracy was high enough to produce physical results useful for testing the objective function derivation and optimization architecture.

3.1.3 Friction Drag Approximation

If computationally expensive viscous simulations are not feasible for the computational hardware available, friction drag estimates can be used in conjunction with the induced drag found from inviscid simulations. The friction drag coefficient of the wing can be estimated using a simple flat plate estimate expressed by the following equation:

$$C_{D,friction} = \frac{C_f \cdot S_{wet}}{S} \tag{3.1}$$

where $C_{D,\,friction}$ is the friction drag coefficient, C_f is the skin friction coefficient and S_{wet} is the wetted wing area. The skin friction coefficient can be calculated using the flat plate assumptions for laminar and turbulent boundary layers [6]:

laminar: $$C_f = \frac{1.328}{\sqrt{\mathrm{Re}_c}} \tag{3.2a}$$

turbulent: $$C_f = \frac{0.074}{\mathrm{Re}_c^{1/5}} \tag{3.2b}$$

where Re_c is the Reynolds number calculated using the chord length as the reference length. Transition between the laminar and turbulent boundary layers can be approximated by the critical Reynolds number. The boundary layer transition location can be found by solving

the Reynolds number equation with a value of 500,000 at the specified altitude and velocity.

3.2 STRUCTURAL ANALYSIS

The wing weight estimator used in the current work is a MATLAB program named EMWET (Elham Modified Weight Estimation Technique) [25]. The program utilizes a structural sizing method and is composed of a wing box weight estimator module, a non-optimum and secondary weight estimator module, and a simple module that sums all the weight contributions. EMWET requires geometrical, physical, material, and aerodynamic load inputs which are summarized in Table 3.1.

Table 3.1 EMWET inputs

Geometry	wing reference area
	wing span
	airfoil geometry
	airfoil location
Physical	maximum take-off weight
	maximum zero fuel weight
Material	Young's modulus
	density
	tensile yield stress
	compressive yield stress
Aerodynamic	spanwise load distribution

The wing box weight estimation module applies class II & 1/2 methods which use the strength and stiffness of the material and elementary, physics-based structural analysis to determine the amount of material required to resist the given loads. The main wing box structural elements are the upper and lower skin panels and spar webs and are illustrated in Figure 3.3.

The non-optimum and secondary weight estimator module computes the weight contributions of the ribs and all other non-optimum and secondary structures, such as joints,

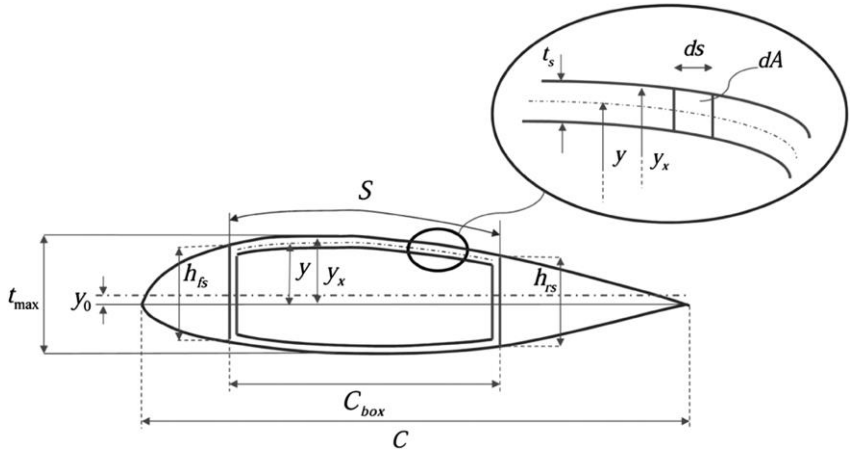

Figure 3.3 EMWET wing box [25].

using semi-empirical methods and statistics [25] proposed by Torenbeek [26]. The final module computes the total wing weight determined by the sum of all previous weight contributions [25].

As described above, the weight of the wing is a function of all the inputs listed in Table 3.1. During the optimization, the maximum take-off and zero fuel weights and material properties remain constant, such that the wing weight becomes a function expressed below:

$$W_{wing} = f\left(S, b, airfoils, L_{span}, M_{y,span}\right) \tag{3.3}$$

In Eq. (3.3) b is the wing span, *airfoils* is the data for each airfoil section from the wing, M_y is the pitching moment, and the subscript *span* denotes the spanwise distribution of the quantity. The variable *airfoils* contains several different parameters for each airfoil section along the wing and includes the normalized xz-coordinates of the profile, the airfoil's leading edge coordinates, the chord, and the normalized spanwise location. The xz-coordinates are normalized with the chord length and the spanwise positions are normalized with half of the span length. Figure 3.4 shows an example of an airfoil before

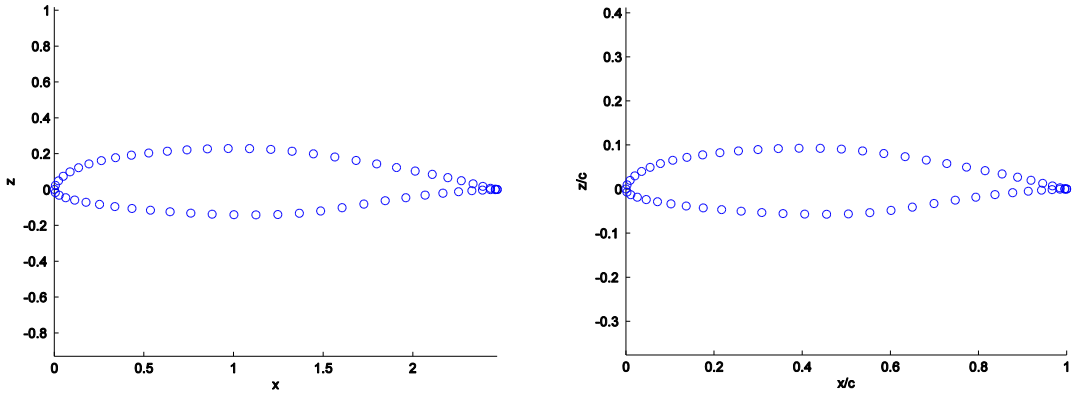

(a) (b)

Figure 3.4 (a) Dimensional airfoil in base units. (b) Nondimensional airfoil normalized by chord.

and after normalization with the chord. All three geometry parameters, *S*, *b*, and *airfoils*, are obtained from the computational surface grid, which is controlled by the design vector. The aerodynamic forces are calculated from their coefficients, which are provided by the aerodynamic analysis tool. Using the wing weight calculated by EMWET, the gross weight of the aircraft becomes the sum of the wing, propulsion, and equipment weights as shown below:

$$W = W_{wing} + W_{propulsion} + W_{equipment} \tag{3.4}$$

The propulsion weight consists of the engine, battery, propeller, and their associated wiring, fasteners, mounts, etc. The equipment weight consists of servos, avionics, ESC, and the weight of their associated parts.

3.3 GEOMETRY EXTRACTION

Obtaining accurate planform parameters proved to be a difficult task early in the development of the MDO tool. The accuracy of the reference area is important since it is used to dimensionalize all the aerodynamic coefficients to obtain forces. Its inclusion in the coupling vector also means that its derivatives are required to solve the optimization

problem. The wetted area is also important for when friction drag estimates are used. The solution to accurate reference areas was to import the entire computational surface grid into MATLAB [27], discussed below, and to find the convex hull of the nodes in the x-y plane. A convex hull is defined by the points that envelope the remaining points. The area of the convex hull is then calculated and used as the reference area of the wing. An example of a convex hull is shown below in Figure 3.5.

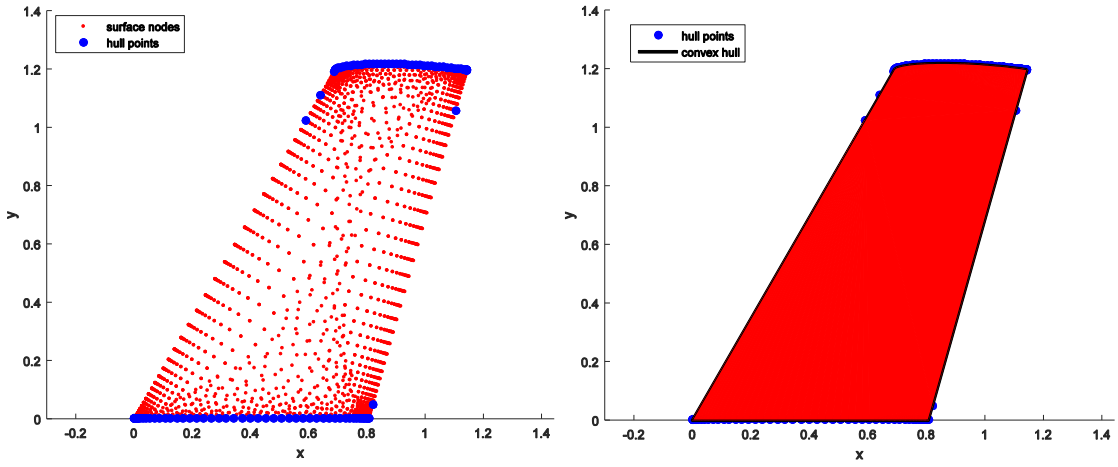

(a) (b)

Figure 3.5. (a) Surface nodes of a wing with the convex hull points shown in blue. (b) The hull points are connected to form the convex hull.

The wetted area was calculated using a similar method. From the imported surface grid, the triangular element connectivity was recreated so that the area of each element could be computed and summated. The area of each element was computed using the expression below where $\boldsymbol{a}$ is the vector of one edge of the element and $\boldsymbol{b}$ is the vector of the adjacent edge. An example of a surface element is shown in Figure 3.6.

$$area = \frac{1}{2} \cdot |\boldsymbol{a} \times \boldsymbol{b}| \tag{3.5}$$

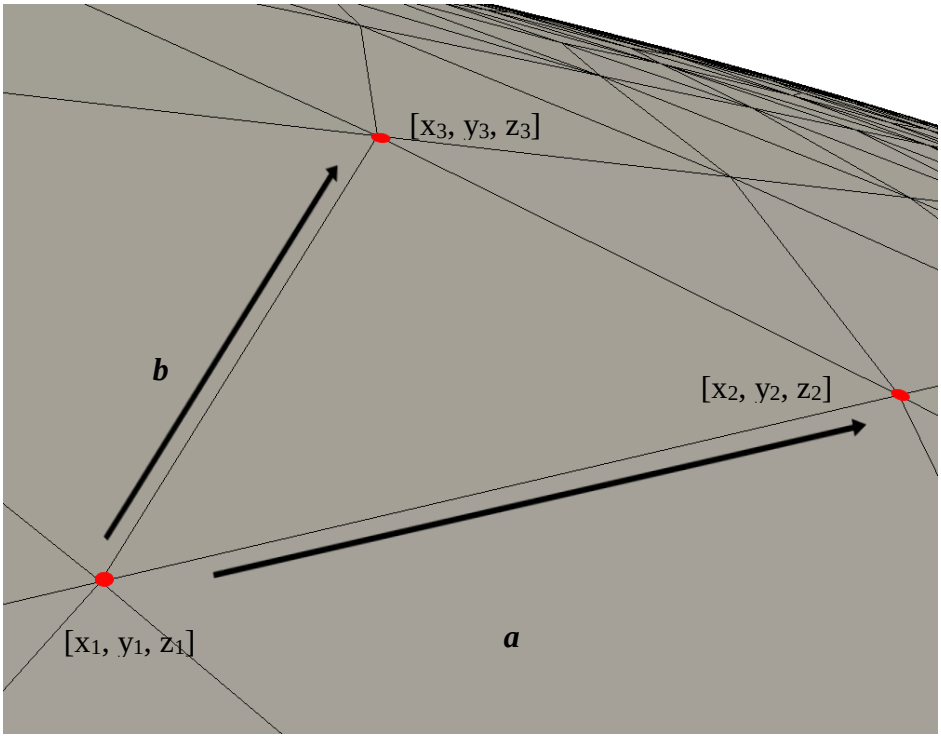

Figure 3.6. Example of surface element.

Up to five equally spaced airfoil profiles were also extracted. The profiles are written to a single text file by SU2 and the data is imported into MATLAB where the points are separated into individual airfoil sections. After the airfoils are separated, they are modified so that the Cartesian coordinates are in the correct order for the wing weight estimation tool: counterclockwise from trailing edge to leading edge and back to the trailing edge. A level of filtering is performed to remove any coordinates that may end up on the wrong surface, e.g., a point from the upper surface being listed with the lower surface points. Next, the nondimensional airfoil coordinates clipped from the surface grid are interpolated using 101 cosine-spaced points along the x-axis, creating a clean airfoil coordinate file for the weight tool.

3.4 OPTIMIZATION FRAMEWORK

The MATLAB computational software package [27] and its Optimization Toolbox were used to perform the optimization of the objective function. The Optimization Toolbox has several optimization functions to choose from based on the type of optimization problem which can be linear or nonlinear, continuous or discrete, and bounded or unbounded. The objective function in this work is smooth, nonlinear, subjected to linear constraints, and bounded. Based on this information, the fmincon function was selected.

fmincon is a nonlinear programing solver for minimization of multivariable, constrained functions. There are several different algorithms available for fmincon which include interior-point, sequential quadratic programming, and trust-region-reflective. Information regarding the details of each algorithm can be found in the MATLAB documentation [27]. The sequential quadratic programming (SQP) algorithm was chosen due to its strict feasibility with respect to the bounds, meaning that every iteration is performed within in the set bounds of the problem. Respecting bounds is important because the design vector cannot exceed the specified values without risk of intersecting the geometry it is controlling. This can lead to numerical errors during the gradient projection stage, yielding invalid sensitivity results.

3.5 COMPUTATIONAL HARDWARE

Optimizations and analyses were performed on three different machines. Much of the optimization architecture and optimization problem was developed and debugged on a laptop computer with an Intel Core i5 processor and 8 GB of RAM. This system was more than powerful enough for performing optimization using AVL, but was not sufficient for efficient SU2 computations. Optimizations using AVL on the laptop took between 50 to

90 seconds to complete. Once the architecture and framework were developed, AVL was replaced with SU2, and computational work moved to a desktop with 2 Intel Xeon processors and 64 GB of RAM. On the desktop, all modules of SU2 were performed using parallel computing utilizing all available processors. Depending on the number of design variables considered, inviscid optimization runs with SU2 required between 60 to 150 minutes for 24 to 72 design variables respectively. The computation of the sensitivities required most of the computational effort while the aerodynamic and structural analyses remained relatively constant. Once the MDO tool was developed and debugged, optimizations were moved to the university-owned Bolden cluster. Only one node was used due to the number of MATLAB licenses available. The node is comprised of 20 cores and an Intel Xeon processor with 64 GB of RAM [28]. On this machine, inviscid optimization runs with SU2 required between 47 to 77 minutes for 24 to 72 design variables respectively. Hardware specifications of all three machines are listed below in Table 3.2.

Table 3.2. Computational hardware specifications

machine	specification
laptop	Intel Core i5-4210H CPU @ 2.90 GHz 2 cores and 4 threads 8.0 GB RAM
desktop	2 Intel Xeon CPU E5-2603 v3 @ 1.60 GHz 6 cores and 6 threads per processor 64.0 GB RAM
cluster node	Intel Xeon @ 2.8 GHz 20 cores 64 GB RAM

3.6 MDO SHAPE OPTIMIZATION TOOL

This section explains in detail the workings of the MDO shape optimization tool developed in this work. The optimization tool is comprised of three main stages in addition to setting up the inputs. One of the key inputs to the tool is the CFD mesh of the original aircraft with a FFD box constructed around the region to be manipulated. The computational mesh must be constructed with triangular surface elements. Other required FFD information includes the order of the FFD box's edges and a list of the FFD control points that form the design vector. The remaining inputs include the freestream properties of the flow, the battery and propulsion parameters, and the fixed weight items of the aircraft. The constant inputs are organized and distributed among seven text files and an excel file, with examples shown in Appendix A, which are all read by the MDO tool at the start of the optimization. The other key inputs, such as the configuration file and the mesh are discussed in further detail in Chapter 4.

The initialization module, Stage 1, is the first component of the MDO tool. Here, the base CFD mesh is deformed per the displacements of the design vector. After deformation, the planform parameters and airfoil shapes are extracted from the deformed mesh and stored for later computations for the same shape. The final step in Stage 1 is the initialization of the CFD solution. The initialized solution is later used to restart the simulation at a pre-converged point to decrease computation time, thus, convergence speed and eliminating low frequency errors have priority over high accuracy. Therefore, a two level multi-grid and one level multi-grid are used for inviscid and viscous simulations respectively, both with V-cycle. Convergence is also discussed in more detail in Chapter 4.

Once the initialization module is complete, the initialized solution and planform parameters are passed to Stage 2. Here, the CFD analysis is restarted using the initialized solution and an initial angle of attack. Next, the aerodynamic loads obtained from the aerodynamic analysis tool are passed to the weight estimation tool where the wing weight is calculated and the gross weight obtained. The difference between the lift and the weight is calculated and a new alpha is chosen by the multidisciplinary analysis driver, where the process is repeated until the consistency error drops below the specified convergence value. Once a consistent solution is obtained, the module produces the final flow solution file, aerodynamic coefficients, and gross weight.

Finally, Stage 3 performs all the sensitivity calculations. The module requires the final flow solution file from Stage 2 and the planform parameters from Stage 1. The adjoint sensitivity module performs the discrete adjoint sensitivity analyses of the lift and drag. Depending on the number of design variables, multi-grid may not be used for the discrete adjoint analysis due to computational memory limitations. Once an analysis is complete the gradients are projected onto the FFD box, yielding its sensitivity with respect to the FFD control points. The planform and weight sensitivity module uses a finite difference approach where each control point is displaced by the specified step size. The finite difference module is computationally costly, but the two sensitivity modules can be performed in parallel.

Once Stage 1 through 3 are completed, the objective function and its derivatives are computed, followed by the constraint functions and their derivatives. Using this information, the optimization driver changes the design vector and a new optimization iteration is started. A detailed work-flow of the MDO tool is shown in Figure 3.7.

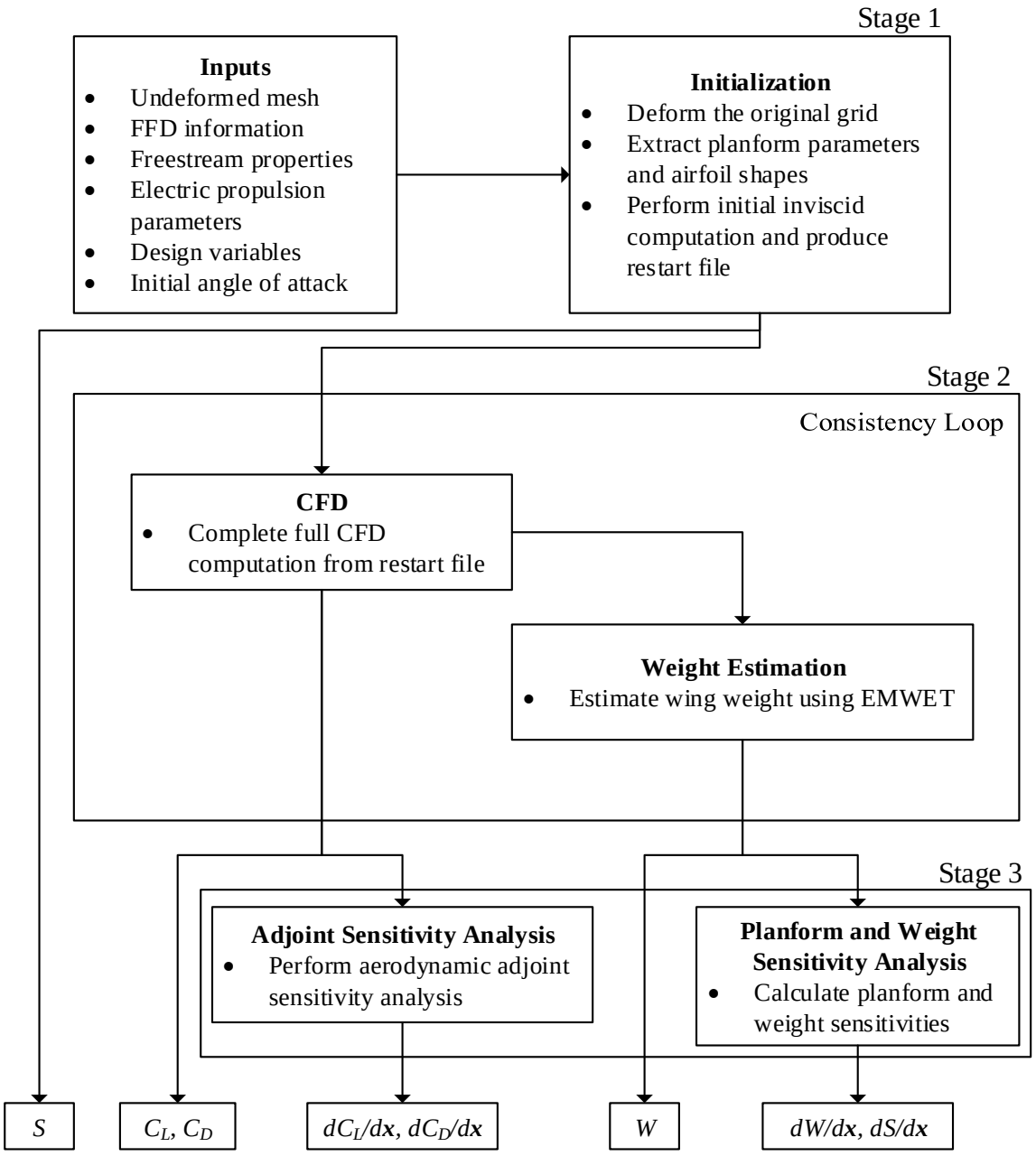

Figure 3.7. Detailed work-flow of MDO aerodynamic shape optimization tool.

CHAPTER 4

COMPUTATIONAL INPUTS

The inputs that require construction prior to the optimization are discussed in this chapter. These include the CFD mesh and the FFD box used to deform the mesh. The configuration file for the SU2_CFD module is also discussed. The configuration file is a required input, but is constructed during each optimization iteration based on the specified aerodynamic properties and the angle of attack used in Stage 2 of the MDO tool. The configuration file plays a large role in the accuracy and convergence rate of the solution.

4.1 UNSTRUCTURED MESH

The computational grid, or mesh, plays an important role in CFD simulations. The quality and level of discretization of a mesh can greatly influence the result of a simulation. Additionally, meshes created for aerodynamic shape optimization must also be robust so that when deformed, the mesh is still functional, meaning that the cell growth must be as smooth as possible and cell aspect ratios must be close to optimum. ANSYS ICEM CFD [29] was used to create all the computational meshes created by the author while the ParaView data analysis software [30] was used to visualize the CFD data on the mesh. The steps taken to create each mesh are explained in the following sub-sections.

4.1.1 Computational Domain

First, the aircraft surface was imported into ICEM where the domain was built around the aircraft. The origin of the domain is located at the leading edge of the root airfoil

with the positive x-axis oriented through the root chord line of the aircraft. The positive y-axis is perpendicular to the x-axis in the spanwise direction. Finally, the z-axis is normal to the xy-plane in the thickness direction, completing the orthogonal coordinate system. Utilizing the symmetry of the aircraft at the root chord, the aircraft and the domain where split in half with a symmetry plane in the xz-plane. An example of a domain is shown in Figure 4.1.

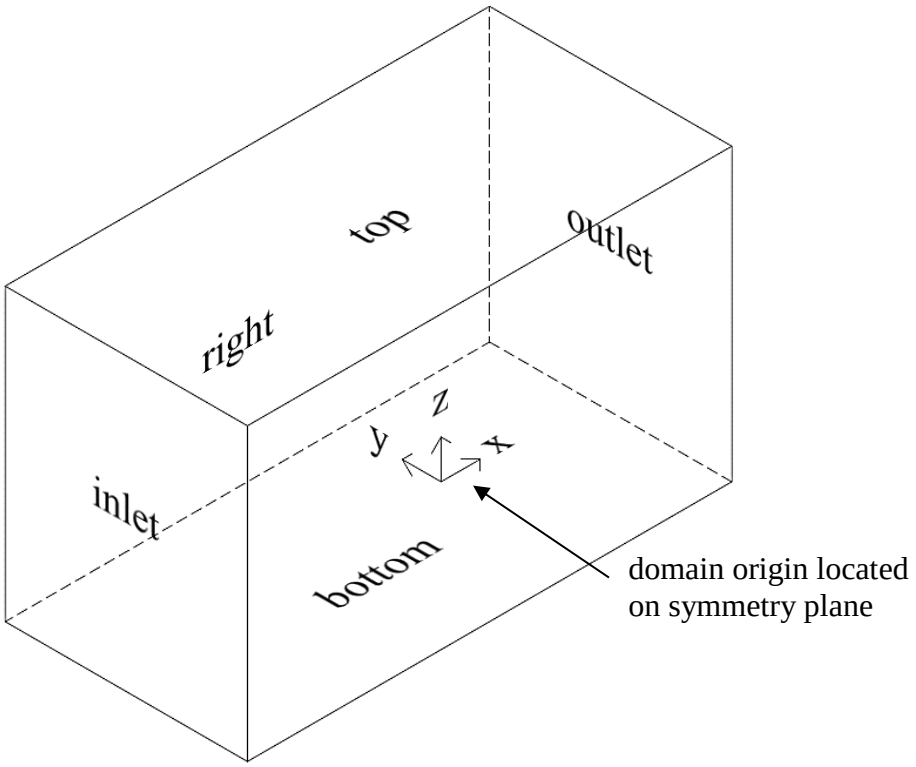

Figure 4.1 Example of computational domain.

Domain sizing is very important and must be determined based on the model under investigation. A domain that is too small will cause errors in the flow, similar to those caused by wind tunnel walls during wind tunnel experiments. During wind tunnel simulations, the finite volume of the test section causes pressure distributions, streamlines, and induced drag to differ from normal flight and corrections must be applied. CFD

boundaries and their respective boundary conditions must be placed at a distance great enough from the body to not cause similar errors. If a CFD boundary with a specified farfield pressure boundary condition is placed too close to the body, its enforcement of the pressure will be felt through the flowfield, causing the pressure distribution near the body to be inaccurate. Another example is the specification of freestream turbulence during viscous simulations with turbulence models, where the values of parameters such as kinetic turbulent energy and specific dissipation are estimated but never known. Setting these boundary conditions an appropriate distance away from the model increases the chance that any error in the initial estimation will be dissipated before reaching the body. The domain can also be too large with an unnecessary number of cells that increase simulation times. The locations of the boundaries with respect to the domain origin were determined using the relations listed in Table 4.1 where c_r is the root chord.

Table 4.1 CFD domain boundary locations

Name	Distance from origin
inlet	-10 c_r
outlet	20 c_r
right	10 c_r
top	5 c_r
bottom	-5 c_r
symmetry	xz-plane

Using the relationships in Table 4.1, a test mesh was created using the KittyHawk geometry. This mesh was used in simulations with an angle of attack range from 0° to 6°. After each simulation, the flowfield was inspected for noticeable disturbances in the pressure field and streamlines. In all of the cases checked, the contour lines corresponding to positive and negative 0.01 pressure coefficient remained within 2.5 c_r of the body and did not show signs of interaction with the domain boundary conditions.

4.1.2 Meshing

With the computational domain specified, the second step of creating a mesh was to discretize the surfaces. The surface mesh was primarily controlled by the discretization of the edges defining the surfaces. Special selection of element size and spacing was used to create smooth transitions from the refined areas near the leading and trailing edges to coarser regions along the middle of the body's upper and lower surfaces. The surface mesh away from the edges was controlled by mapping enforcement and cell growth rates. All boundary surfaces were automatically meshed by specifying the maximum element size since they are at the greatest distance from the aircraft. Only the symmetry boundary required additional attention; the transition from the maximum element sizes along the plane's perimeter to the smaller element sizes where the aircraft geometry intersects the plane had to be smoothed.

The third step of creating a mesh is to discretize the volume. This is a relatively easy process using volume-filling methods and specified growth rates. Density regions can also be added in areas where the flow may be more complex. Density regions were added along the trailing edge of the wing and extended 1/2 c_r in the streamwise direction to help resolve the wake of the aircraft.

If a viscous simulation is to be performed, a boundary layer mesh must also be created along any solid surfaces. The viscous boundary layer is comprised of several different regions: the viscous sub-layer, the buffer layer, and the outer layer. Low-Re turbulence models, such as those implemented in SU2, resolve the details of the turbulent flow through the boundary layer, thus requiring an appropriately sized grid to resolve the different sub-layers. Generally, the near-wall mesh must be discretized with a first cell

height of $y^+ \approx 1$. y^+, or wall units, are a non-dimensional unit to measure distance in the immediate proximity of a solid surface and is expressed as:

$$y^+ = \frac{yu_\tau}{\nu} \tag{4.1}$$

where y is the dimensional distance from the wall, u_τ is the friction velocity, and ν (nu) is the kinematic viscosity [31]. Achieving the correct y^+ value is often an iterative process, as information regarding the local flow is required. The boundary layer mesh can quickly increase the total cell count, so the number of layers and the growth rate need to be selected with great care.

The final step in mesh creation is the mesh independence study. Once simulations are conducted with a new mesh, the mesh should be refined and used to perform the same simulations. Once comparison between the results of the different meshes shows convergence, the solution is determined mesh independent. This process verifies that the results do not change with the computational mesh.

4.1.3 FFD Box

The construction of the FFD box around the geometry is performed by SU2 based on a construction configuration file filled by the user. Providing the necessary inputs is easy, however, the behavior of the FFD boxes should be kept in mind when creating the boxes. The first behavior to note is that FFD boxes in SU2 maintain a first or second order continuity, specified by the user, where the box intersects the surface geometry. To maintain the continuity, the SU2_DEF module locks the position of the intersecting plane and the plane perpendicular to the intersecting plane. The second behavior to note is related to the gradient projection during aerodynamic sensitivity analyses. When FFD boxes are created close to the geometry, the magnitudes of the projected gradients are greater than

when the box is further from the surface. The larger magnitudes can lead to quicker optimization convergence by causing larger displacements, however, the closer the control points are to the surface, the greater the chance that one of them will intersect the surface of the geometry. The last behavior is related to the previous one, where gradients are not fully projected, or projected at all, when control points intersect the geometry.

4.2 CONFIGURATION FILE

The configuration file for SU2 provides all the necessary information required to perform a simulation. There are many solver, stability, and convergence options which are typically fine-tuned for a given problem. However, this is difficult to accomplish during an optimization, where many different problems are being solved sequentially, meaning that the options provided to the CFD program must also work for all other problems encountered during the optimization.

4.2.1 Governing Equations

The first major decision to be made is the selection of the governing equations to be solved. As stated previously, SU2 can solve the inviscid Euler equations and the viscous Navier-Stokes equations, with or without a turbulence model. Without a turbulence model, a Navier-Stokes simulation simulates the flow with laminar boundary layers. When using a turbulence model, SU2 uses the RANS method to resolve the flow. The RANS equations are derived by decomposing the velocity into mean and fluctuating components and averaging the result. An additional set of algebraic or empirical equations that model the turbulence in the flow is added to the problem to complete the solution. Thus, the time-dependent turbulent flow is reduced to a single steady-state computation where all turbulence is modelled rather than computed [31].

Solving each set of governing equations has its advantages and disadvantages. The Euler equations require the least computational effort to solve which can lead to more simulations for a given time, or the ability to perform simulations on lower-grade computational hardware. Another advantage is a reduced computational mesh size due to the lack of a boundary layer mesh which increases the speed at which the domain can be deformed. The obvious drawback is that real flows, especially at subsonic conditions, have significant viscous effects. The friction drag component can be approximated using empirical equations. Solving the Navier-Stokes and RANS equations produce more accurate results by including viscosity and profile drag caused by flow separation, but require more computational effort, more meshing effort, and can be difficult to converge, but, when compared to the time-dependent direct numerical simulations (DNS) and large eddy simulations (LES), the Navier-Stokes and RANS methods are well suited for large-scale engineering problems such as aircraft.

If a RANS simulation is to be performed, a turbulence model must be chosen. The two turbulence models considered in this work are Spalart-Allmaras (SA) [32] and Menter Shear Stress Transport (SST) [33]. The SA model is a one equation model that solves a modelled transport equation for a viscosity-like variable. SST is a two-equation model that uses the k-ω formulation in the inner parts of a boundary layer and the k-ε formulation in the freestream. SST is widely used in industry [34] and can work better than SA in adverse pressure gradients where SA can undershoot the amount of separation [31]. However, only the SA model has been validated for the incompressible solver in SU2. The original formulation of both models are low-Re models and require a first wall cell thickness of $y^+ \approx 1$.

4.2.2 Flow Regime

The SU2 suite is primarily built as an analysis tool for compressible flows, where the Mach number is greater than 0.3. The aircraft studied in this work flies at a Mach number just below 0.1 so simulations can be run using either the compressible or incompressible options with the same flow parameters. The incompressible solver is pressure-based while the compressible solver is density-based. It should be noted that the conservative vector (U) is different for the compressible and incompressible solutions and is shown below:

$$\text{compressible:} \quad U = \begin{bmatrix} \rho \\ \rho u \\ \rho v \\ \rho w \\ \rho E \end{bmatrix} \qquad \text{incompressible:} \quad U = \begin{bmatrix} P \\ \rho u \\ \rho v \\ \rho w \end{bmatrix} \tag{4.2}$$

In Eq. (4.2) u, v, and w are the x, y, and z-velocity components, E is energy, and P is pressure. The E here should not be confused with endurance used throughout the rest of the work.

The flow problem can be solved using either the compressible or incompressible solvers, but the incompressible solver allows the use of only the Roe and Jameson-Schmidt-Turkel (JST) convective schemes. The Roe convective scheme uses the upwind method and is naturally dissipative, making it more stable, but produces excess artificial viscosity at low Mach numbers [35]. JST is a central scheme, and is computationally cheaper than the Roe schemes, but requires additional artificial dissipation terms and has lower boundary layer resolution [36]. A modification of the Roe scheme, the Turkel-preconditioned Roe scheme is conditioned to perform better at low Mach numbers [37].

For all simulations, 2nd order numerical integration was used for the flow solver to minimize additional numerical diffusion. For turbulent flows, a 1st order numerical

integration was required to achieve convergence. The final option chosen for the flow solvers was the time discretization method: explicit or implicit. Explicit time integration depends only on the current state and is fast, but has stability issues, requiring a small time step. Implicit time integration depends on the current state and the state at the next time interval, making implicit methods slower than explicit methods. An advantage of implicit methods is that the time step is not restricted by stability requirements [38]. However, implicit methods can produce large truncation errors if the time step is too large, especially for time-dependent solutions [39]. All of the simulations in this work are conducted at steady state, thus larger time steps and robustness make implicit time integration the method of choice.

4.2.3 Convergence and Stability

Depending on the governing equations and solver options chosen, the simulation will behave differently. The most important parameter determining the stability of the solution is the Courant–Friedrichs–Lewy (CFL) number. The CFL number restricts the allowable time step and states that: the numerical domain must include all of the analytical domain and the value must be as close to unity as possible [40]. For explicit time integration, the CFL number must be less than or equal to 1 to maintain solution stability but can be greater than 1 for implicit methods.

There is also a convergence acceleration method known as multi-grid implemented in SU2. On the base computational grid, high-frequency errors are eliminated quickly, while low-frequency oscillations require more time. The multi-grid method is used to eliminate low-frequency errors by coarsening the grid, causing the low-frequency error to become a high-frequency error on the coarser grid. Multi-grid methods increase the time

of each iteration but decrease the total number of iterations. Several simulations conducted with and without multi-grid showed that the multi-grid method typically reduced the number of iterations by 60 – 75% while the time of the simulation decreased by approximately 50%.

4.3 TESTING AND VALIDATION

To determine the most appropriate solver and convective scheme combination, several simulations were conducted using a NACA 0012 airfoil, the ONERA M6 wing, and the VX Aerospace KittyHawk. Detailed descriptions of the ONERA M6 wing and KittyHawk geometries are found in Chapter 5. The different combinations include: incompressible Roe, compressible Roe, incompressible JST, compressible JST, and compressible Turkel-preconditioned Roe. The different solver combinations were used in Euler and RANS simulations. In addition, the Euler results were used in combination with the skin friction estimate as the alternative to viscous simulations.

First, a NACA 0012 airfoil was simulated using the Euler governing equations an angle of attack of 3° with both SU2 and XFOIL. Next, the same simulation was conducted using RANS at a Reynolds number of 2.9 million, the Reynolds number at which the KittyHawk will typically operate. In XFOIL, the boundary layer was tripped such that transition occurred at the leading edge of the airfoil. Figure 4.2(a) shows that the Roe scheme produces a large amount of numerical drag in the inviscid simulations, while JST predicts values much closer to zero. For the RANS simulations, it is shown that incompressible Roe and JST combinations provide results nearly identical to XFOIL. Finally, when the skin friction estimate is combined with the Euler simulations, it is found that the incompressible Roe solver-scheme combination produces the most accurate results

(a)

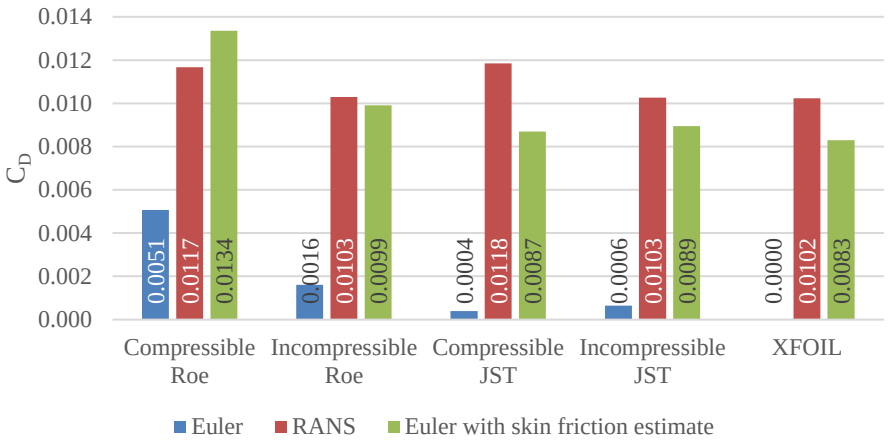

(b)

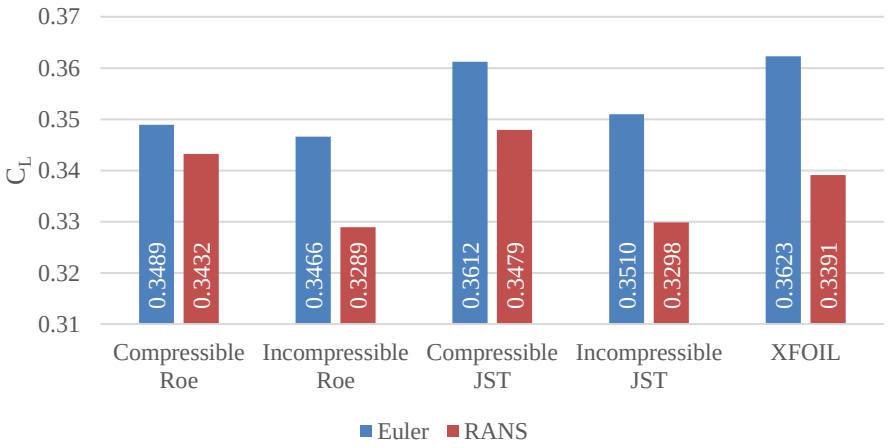

(c)

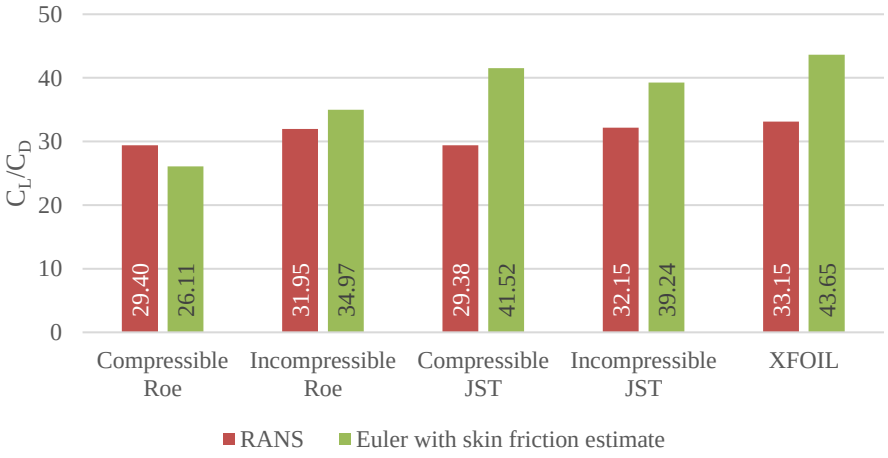

Figure 4.2 Aerodynamic coefficients from NACA 0012 simulations. (a) Drag coefficient. (b) Lift coefficient. (c) Lift to drag ratio.

due to the increased numerical drag. The compressible Turkel-preconditioned Roe combination is not shown here because its inviscid drag calculation was 0.0588, more than ten times that of compressible Roe.

Figure 4.2(b) shows that the lift coefficients from the Euler simulations are relatively close with incompressible Roe having the maximum error of 4.33% and compressible JST having the smallest error of 0.3%. Finally, Figure 4.2(c) shows the lift to drag ratio where all RANS simulations have reasonable agreement and that incompressible Roe and JST have values closest to XFOIL. Figure 4.2(c) also shows that the incompressible Roe estimate with skin friction is the most accurate Euler prediction to the viscous results. The two-dimensional simulation data yields the conclusion that the Turkel-preconditioned Roe scheme is not useful, Euler simulations with skin friction estimates should use the incompressible Roe combination, and the RANS simulations should use incompressible JST.

Next, the same simulation routine conducted for the NACA 0012 airfoil was conducted using the ONERA M6 wing except that XFOIL was replaced with AVL. AVL was used as a reference for induced drag and minimum for the induced drag with skin friction estimate. The lift coefficients from SU2 results were within 7% of each other, with the maximum, compressible Roe, 15% greater than AVL. The more concerning results were of the drag coefficients, shown in Figure 4.3(a). First, the compressible Roe combination estimated a drag coefficient of 0.0606 and thus eliminated from the comparison. In Figure 4.3 we see that incompressible Roe and compressible JST have similar values, with Roe calculating additional numerical viscosity. However, incompressible JST has values similar to AVL, with the RANS solution predicting a drag

(a)

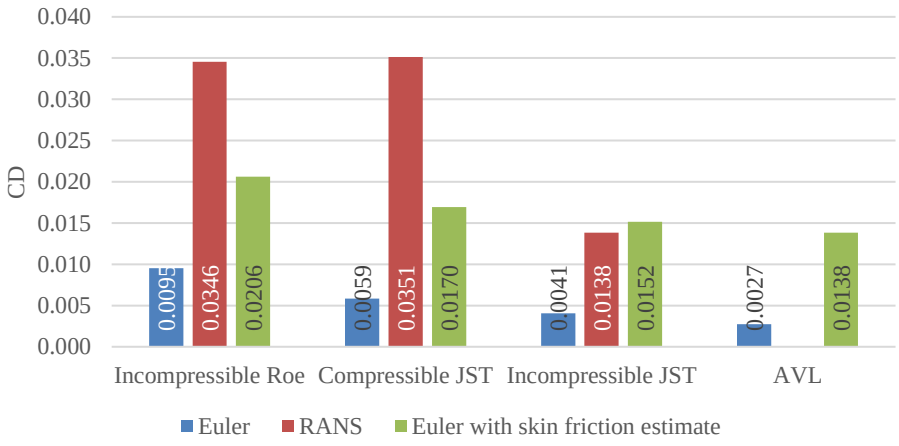

(b)

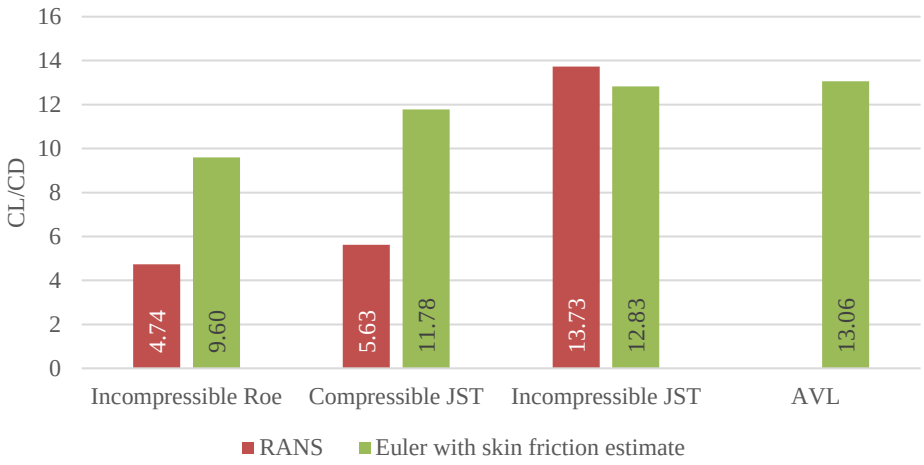

Figure 4.3 Aerodynamic coefficients from ONERA M6 simulations. (a) Drag coefficient. (b) Lift to drag ratio.

coefficient equivalent to AVL's inviscid result with skin friction estimate. From the two-dimensional comparisons, it was expected that incompressible JST would have greater inviscid drag than compressible JST. Comparing Figure 4.2(a) to Figure 4.3(a), it is seen that the relationship between incompressible Roe and compressible JST remains the same. Finally, by investigating the lift to drag ratio shown in Figure 4.3(b), it is shown that the lift to drag ratio of the RANS incompressible JST is greater than AVL. The results from the ONERA M6 simulations yield the conclusion that incompressible Roe should again be

used for Euler simulations with skin friction estimates and that it is unclear as to which solver-scheme combination is best for RANS simulations. The accompanying lift coefficient bar chart for Figure 4.3 is located in Appendix C.

Due to the questionable results of the ONERA M6 wing, a final test was conducted using the KittyHawk. CFD data from the prototype development was provided by Soltmann at North Carolina State University [41]. The provided polar was generated using ANSYS Fluent at a Reynolds number of 3.2 million with a RANS simulation utilizing the SA turbulence model. For this comparison, lift-drag polars were created using SU2 with the inviscid incompressible Roe and JST combinations at the appropriate Reynolds number and include skin friction estimates. From Figure 4.4 incompressible Roe is found to most closely match the polar from prototype development. The greatest difference is between drag coefficients is 22.2% and occurs at a lift coefficient of 0.115, which corresponds to an angle of attack of 1.86°. As the angle of attack and lift coefficient increase, the difference

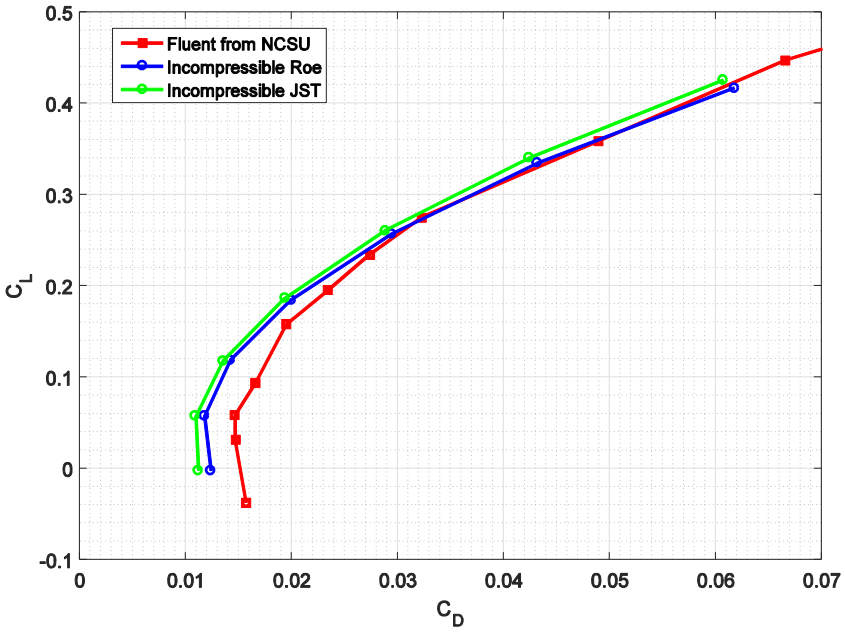

Figure 4.4 Lift-drag polar comparison for KittyHawk.

decreases to under 10% at a lift coefficient of 0.195 and angle of attack 4.27°. It was concluded from the comparison that the incompressible solver and Roe convection scheme should be used for the optimization simulations.

CHAPTER 5

APPLIED MDO SHAPE OPTIMIZATION

This chapter describes the application of the MDO tool to the different test geometries considered in this work including the VX Aerospace KittyHawk aircraft, the ONERA M6 wing, and a modified ONERA M6 wing. Each geometry's initial parameters are discussed, followed by optimizations of that geometry. The developmental results for the two architectures discussed earlier are also presented at the beginning of the chapter, illustrating the motivation to move from IDF-derived architecture to the MDF-based architecture. All the optimization results presented in this chapter are for optimizing endurance. Each optimization was conducted with an FFD box with order 3, 4, and 1 in the x, y, and z-directions respectively.

5.1 THE VX AEROSPACE KITTYHAWK PROTOTYPE

5.1.1 Configuration

The KittyHawk, shown in Figure 5.1, was designed to be a side-by-side, two-seat general aviation aircraft constructed out of a simple carbon fiber airframe. The KittyHawk's current development effort has been switched to using it as an unmanned aerial vehicle for agricultural observation. The KittyHawk's configuration is characterized by a BWB with a high leading edge sweep angle and sharp leading edges. The geometrical characteristics are listed in Table 5.1.

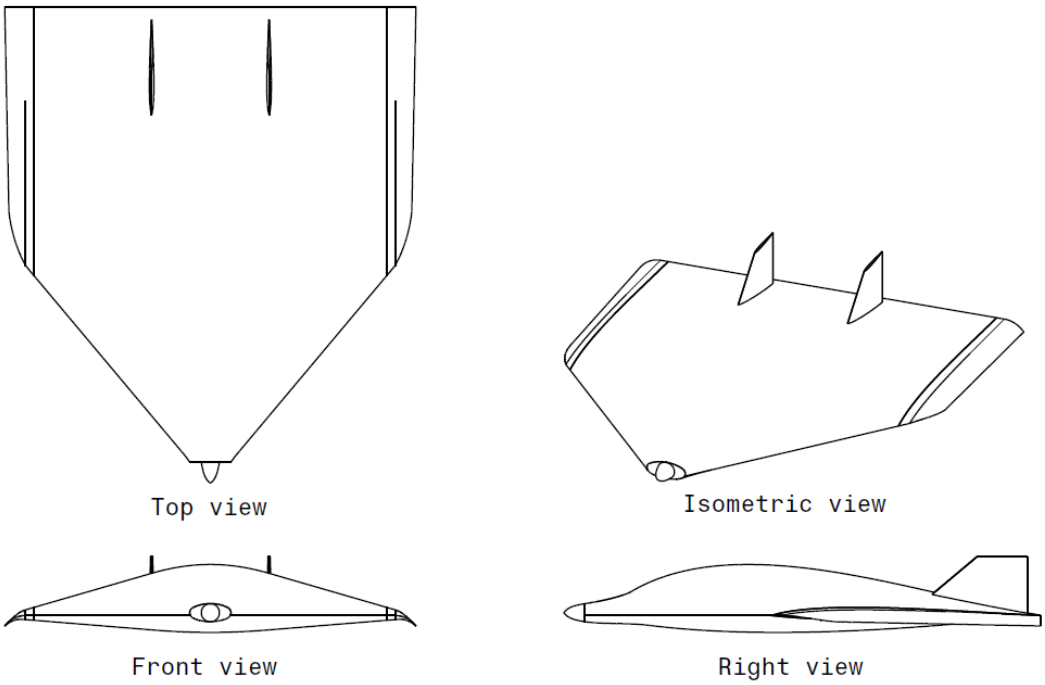

Figure 5.1 VX KittyHawk

Table 5.1 KittyHawk prototype geometrical characteristics.

Planform Parameter	Quantity
Span	1.68 m (5.50 ft)
Root chord	1.95 m (6.40 ft)
Taper ratio	0.513
Leading edge sweep angle	50°

The material used for the construction of the airframe is C-PLY BX 0/45 150 C3.4 12K HS manufactured by Chomarat [42] and the material properties used during the optimization are shown in Table 5.2. The material consists of two unidirectional sub-plies oriented at 0° and -45° that are stitched together. The laminate panel's density was calculated using the thickness of the panel, the mass of the fibers and stitching, the fiber volume fraction, and the density of the resin, Cytec MTM45-1 [43]. Three lamina layers were used as the minimum panel thickness for the optimization.

Table 5.2 Laminate properties.

Property	Value
Panel thickness	0.14 mm
Fiber and stitching mass	153 g/m^2
Fiber volume fraction	57.10%
Resin density	1.18 g/cm^3
Panel density	1.13 g/cm^3
Tensile strength	885 MPa
Tensile modulus	46.7 GPa
Compression strength	572 MPa
Compression modulus	42.9 GPa

The propulsion, navigation, and control systems, all electrical, were specified for the prototype. The essential battery propulsion parameters are listed in Table 5.3 and are kept constant during the optimization.

Table 5.3 Parameters of battery propulsion system.

Parameter	Quantity
Mass of battery	1.16 kg
Number of batteries	5
Battery capacity	5 Ah
Battery output voltage	37 V
Battery hour rating	1 h
Total efficiency	80%

A mass breakdown of the KittyHawk prototype is shown in Table 5.4. The equipment weight includes the avionics, ESC, servos, wiring, and pitot system. The propulsion weight includes the motor, propeller, and batteries. The airframe category includes the landing gear, vertical tails, and wing-body. The landing gear and vertical tails have fixed values, but the wing-body weight is calculated during the optimization. All other fixed-mass items are included in the accessory category. The initial gross mass of the aircraft is 34.2 kg.

Table 5.4 Mass breakdown

Category	Mass (kg)
Equipment	2.52
Propulsion	6.92
Airframe	16.09
Accessory	8.66

Simulations of the KittyHawk prototype in steady level flight predict that the initial lift to drag ratio is 8.9 at an angle of attack of 5.62°. With the initial gross weight, the predicted endurance is 38 minutes. A summary of the initial KittyHawk performance characteristics is listed in Table 5.5. These values are compared to the results of each optimization in the following sections.

Table 5.5 KittyHawk initial configuration characteristics.

Characteristic	Quantity
Endurance	38 minutes
C_L/C_D	6.70
Angle of attack	5.62°
Mass	34.2 kg

5.1.2 Developmental Results

The developmental results for the IDF-derived and MDF-based architectures are shown in Figure 5.2 and Figure 5.3 respectively. All optimizations are initiated from a steady level flight condition using the initial weight of the aircraft, specified velocity, and altitude. Figure 5.2(a) shows improvement to the original aircraft using the architecture derived from IDF, with the objective function decreasing by 20% caused by an increase in the lift to drag ratio and a decrease in the gross weight. Figure 5.2(b) shows that the drag was decreased and the lift increased. However, Figure 5.2(c) shows that the resulting configuration does not satisfy the equality constraint and is not a valid solution. Finally,

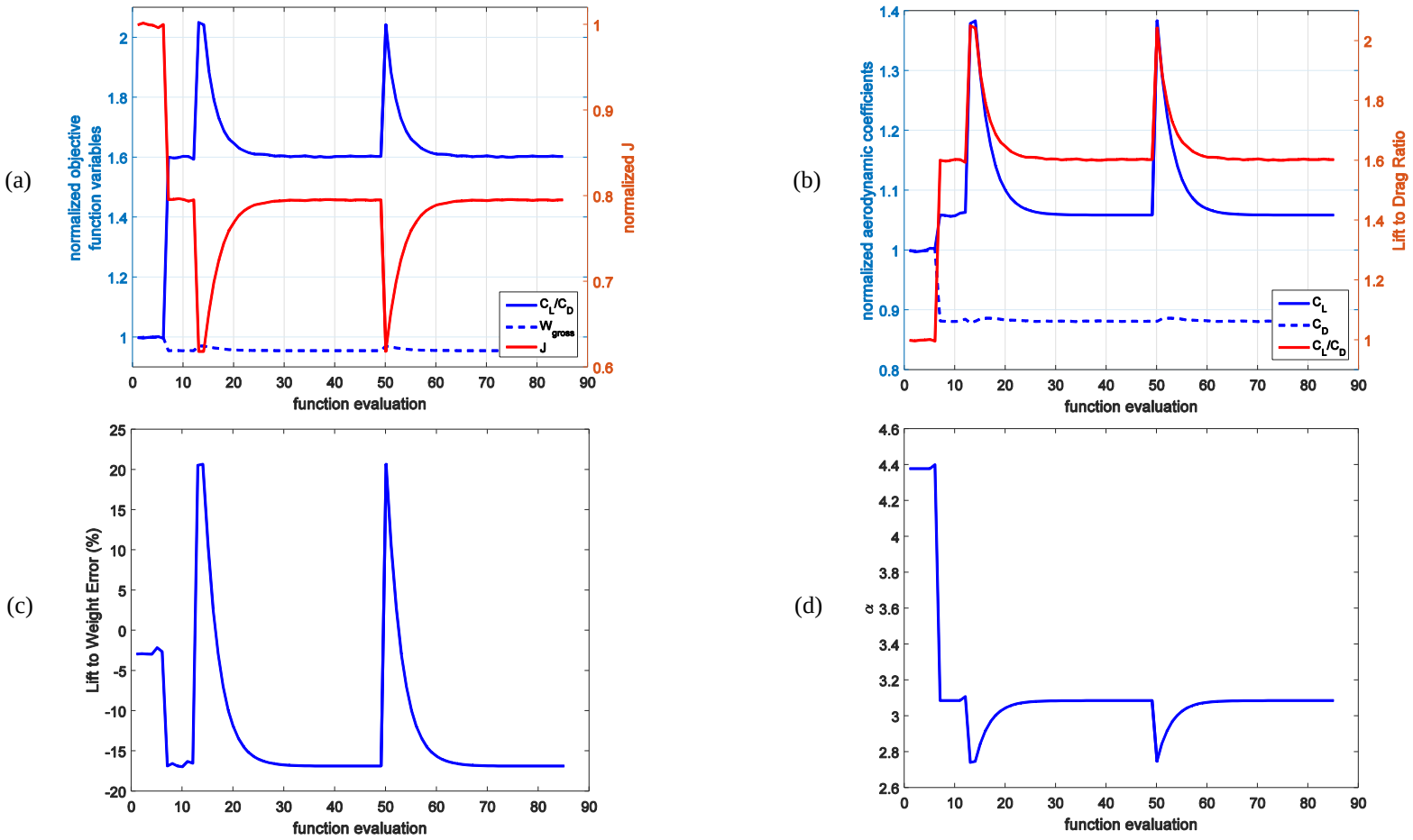

Figure 5.2 Developmental optimization results using IDF-derived architecture. (a) Primary optimization results. (b) Aerodynamic coefficients. (c) Consistency error. (d) Angle of attack.

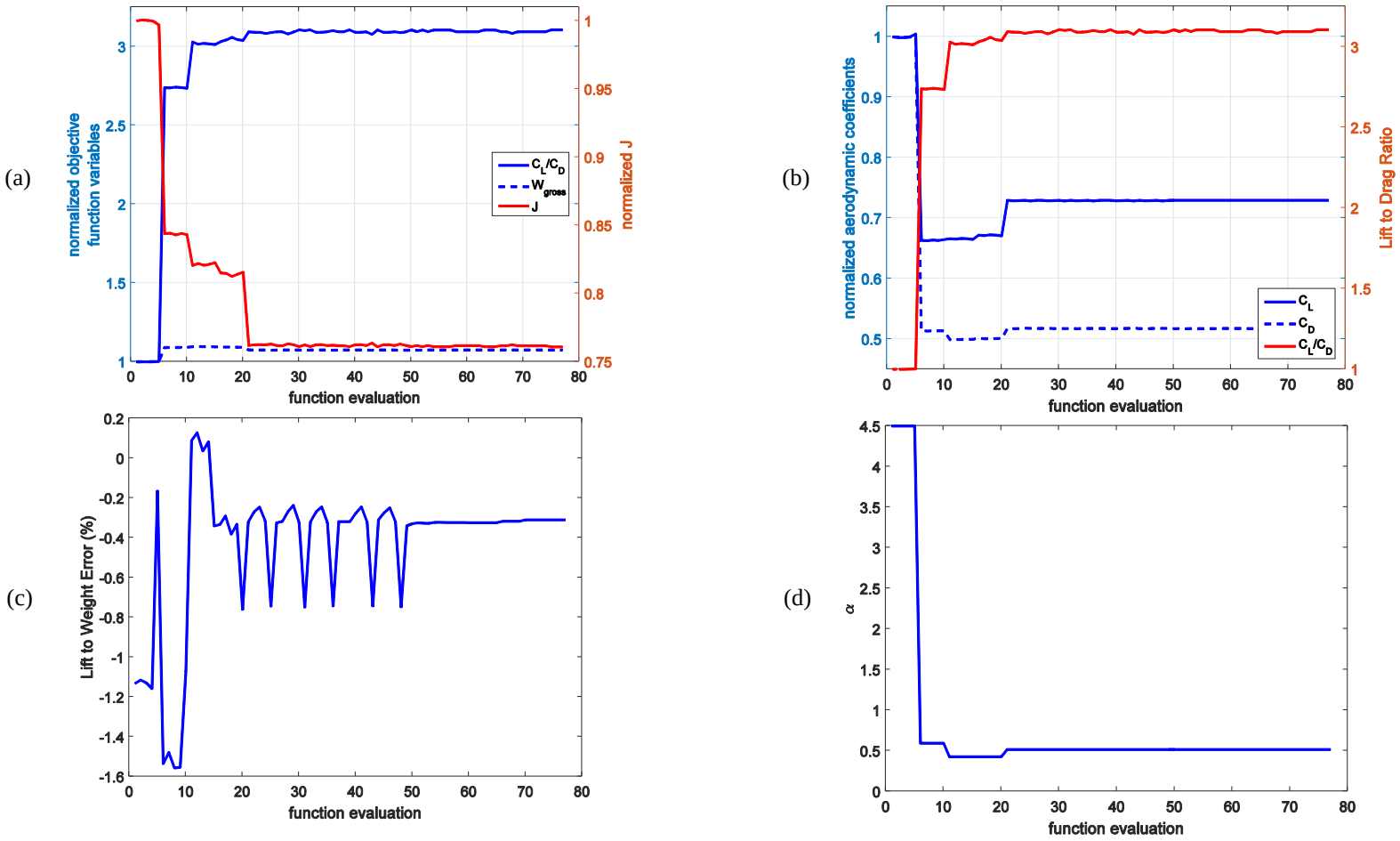

Figure 5.3 Developmental optimization results using MDF-based architecture. (a) Primary optimization results. (b) Aerodynamic coefficients. (c) Consistency error. (d) Angle of attack.

Figure 5.2(d) shows that the angle of attack fails to drop below 2.7 degrees, despite a lower bound of -5 degrees and an unsatisfied consistency constraint.

Figure 5.3(a) shows that as with initial architecture, the MDO tool using the MDF-based architecture effectively improved the endurance of the aircraft. The spanwise parameters were maximized to the allowable bounds, increasing the span by 82% and the reference area by 48%. Despite the large increase in planform, the gross weight of the aircraft increased by only 7.4%. Figure 5.3(b) shows that the lift to drag ratio was again increased, even though the lift coefficient decreased from its initial state. Unlike the results from the first optimization, the MDF-based results have consistent solutions at every function evaluation, as shown in Figure 5.3(c). Finally, Figure 5.3(d) shows the angle of attack that produces the consistent solution using the MDF-based architecture.

5.1.3 Planform Optimization

The first optimization of the KittyHawk performed with SU2 was in the planform-related degree of freedom where the FFD control points can move in only the x and y-directions. In Figure 5.4(a), it is shown that there is an initial plummet in the objective function to 0.7664 caused by a large decrease in weight and increase in the lift to drag ratio. During the first iteration of the optimization, iteration 1, the geometry remains the same as the initial condition while the weight and angle of attack change based on the aerodynamic loads provided to EMWET. The wingbox panel thicknesses were immediately reduced resulting in a 20% reduction in gross weight. A reduction in weight was expected, however, the magnitude of the reduction was predicted to be less. This is due to the current stage of the KittyHawk development, where the prototype aircraft was constructed with conservative panel thicknesses for increased robustness during flight tests.

(a)

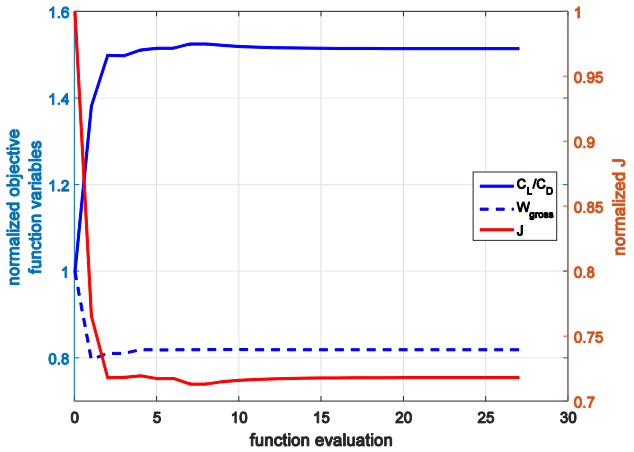

(b)

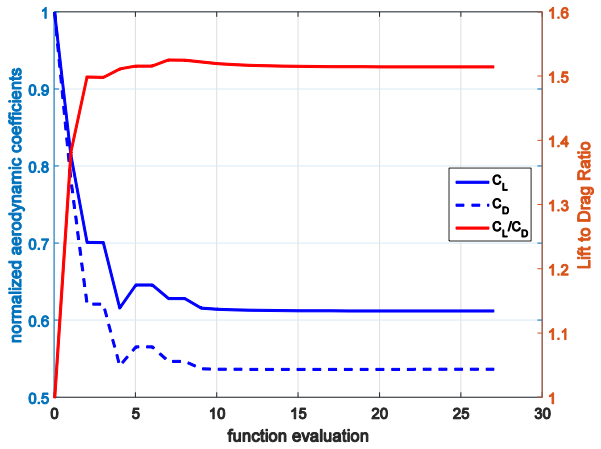

(c)

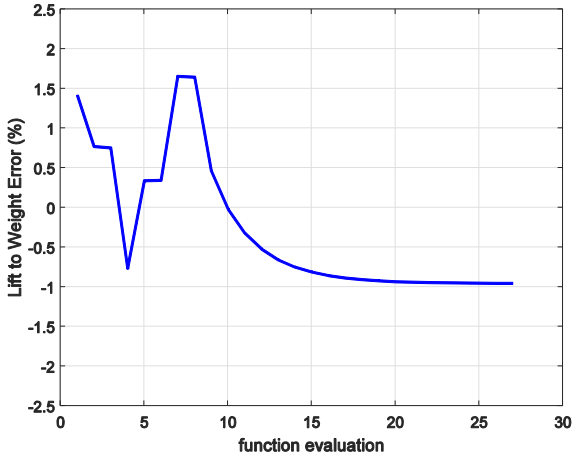

(d)

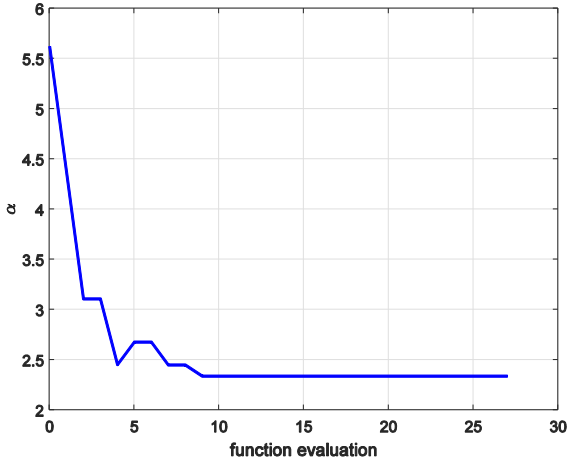

Figure 5.4 Optimization results for KittyHawk with planform-related degree of freedom. (a) Primary optimization results. (b) Aerodynamic coefficients. (c) Consistency error. (d) Angle of attack.

After this initial improvement, the optimizer continues to make progress, finding an optimum aircraft at iteration 7 with a normalized objective function value of 0.7135 through searching 27 configurations. It is also shown that the optimizer made a trade-off between weight and planform, increasing the weight after the initial decrease in favor of improved aerodynamic performance in the form of a larger planform. Figure 5.4(b) shows that the lift to drag ratio increases even though the overall lift coefficient decreases. This behavior matches the trend shown in Figure 5.4(d) since as the angle of attack was decreased so too was the lift coefficient, and more importantly, the induced drag, especially for the small wing span. Figure 5.4(b) and Figure 5.4(d) show that the changes in aerodynamic coefficients and angle of attack are directly related, as they share the same trend over the 27 iterations. Figure 5.4(c) confirms that after the transition was made from AVL to SU2 as the aerodynamic solver, the optimization solutions remain consistent.

The optimized planform hosts a 25% increase in maximum span and reduced leading edge sweep along the outer wing sections, both of which is shown in Figure 5.5. These results are expected, as the extra span increases the aspect ratio of the wing, helping reduce drag due to lift. This is also shown in Figure 5.6 where the optimized planform not only has a larger span but a larger effective span. The wingtip vortices on the original KittyHawk form further inboard on the wing while the optimized planform has the tip vortices more localized to the tip. The new light-weight planform allows the aircraft to fly at an angle of attack of 2.45° with a lift to drag ratio of 10.23, improving the endurance by 40.1%. Since the original starting point of the KittyHawk optimization was from a more burdened weight, the improvement from the first iteration was also measured and shows a 7.4% improvement. The new performance characteristics are listed in Table 5.6.

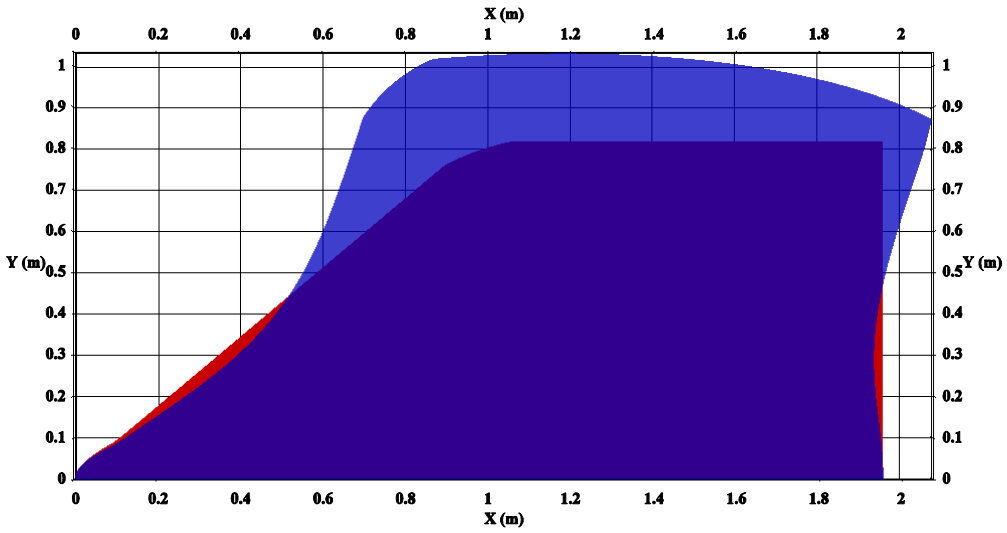

Figure 5.5 KittyHawk planform comparison for planform optimization. Original shown in red (opaque region) and optimized shown in blue.

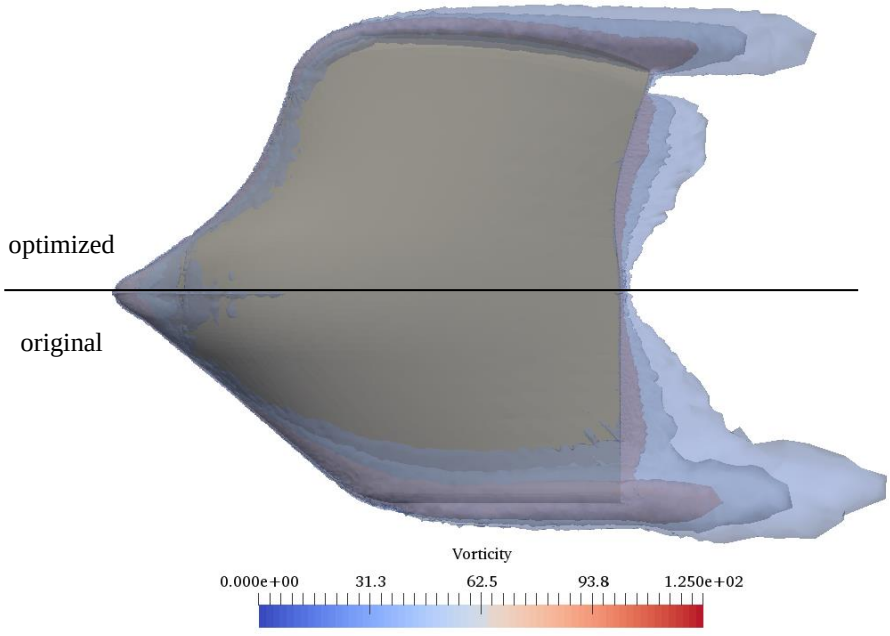

Figure 5.6 KittyHawk wing tip vortices comparison for planform optimization.

Table 5.6 KittyHawk optimized planform configuration characteristics.

Characteristic	Quantity
Endurance	53 minutes
C_L/C_D	10.23
Angle of attack	2.45°
Mass	28.0 kg
Improvement in endurance (actual)	40.1%
Improvement in endurance (from iteration 1)	7.4%

5.1.4 Airfoil Optimization

The next optimization of the KittyHawk was conducted with an airfoil degree of freedom, or where the FFD control points can move in the z-direction. The detailed iteration results of the optimization are shown in Figure 5.7. Exactly as in the planform optimization, there is an initial plummet in the normalized objective function from 1 to 0.7664, helped greatly by a 20% decrease in total weight. However, unlike the planform optimization, the optimizer is unable to further improve the aircraft significantly, decreasing the objective value to a minimum of 0.7661 on the second iteration and searching 50 total configurations. Though further improvement is not made, solution consistency is confirmed with Figure 5.7(c). The optimized configuration has an endurance improvement of 30.5 %, caused by the reduction in mass to 27.3 kg. The aircraft also flies at a new angle of attack of 4.37° with lift to drag ratio of 9.27. The optimized configuration is summarized in Table 5.7.

Unlike the planform optimization, where deformation in the outer shape yielded performance improvements, the deformations in the KittyHawk's airfoils did not produce noticeable results. Airfoil sections from 54, 72, and 90% span are shown below in Figure 5.8. It is easily seen that large deformations occurred with a clear trend of thickening

(a)

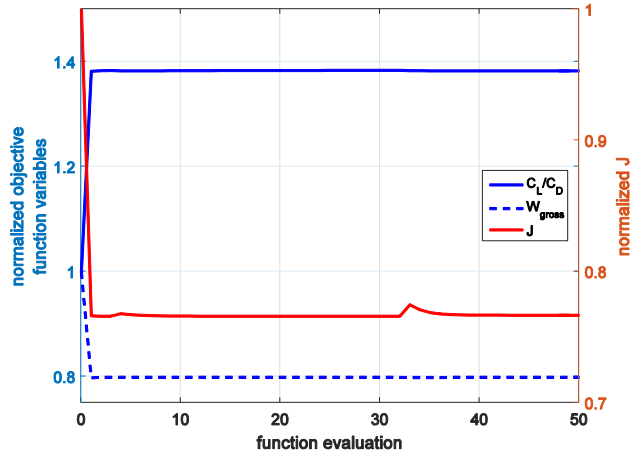

(b)

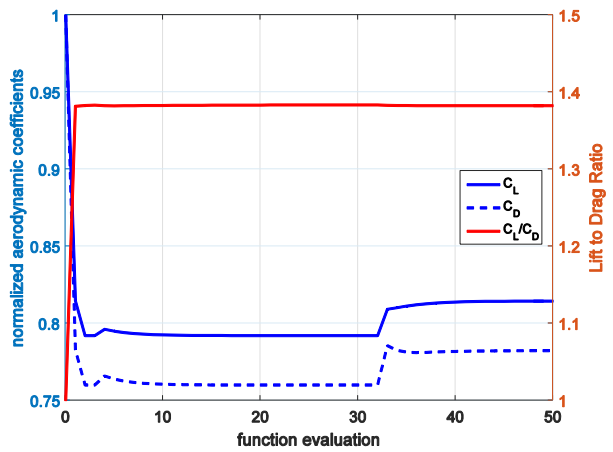

(c)

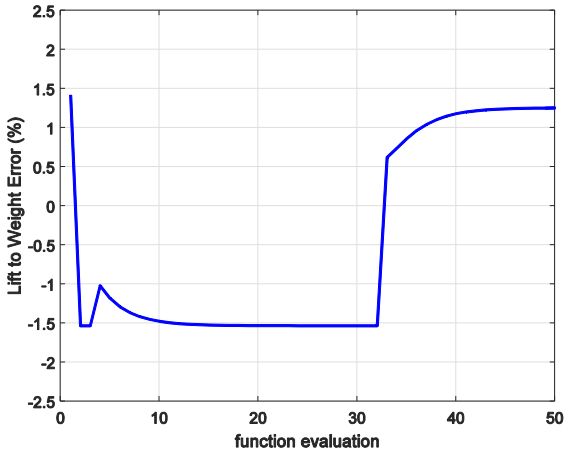

(d)

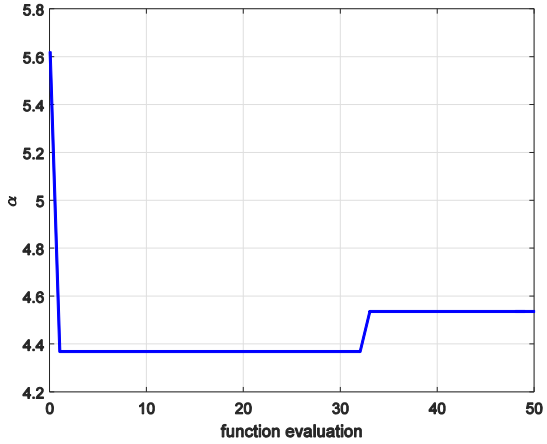

Figure 5.7 Optimization results for KittyHawk with airfoil-related degree of freedom. (a) Primary optimization results. (b) Aerodynamic coefficients. (c) Consistency error. (d) Angle of attack.

Table 5.7 KittyHawk optimized airfoil configuration characteristics.

Characteristic	Quantity
Endurance	50 minutes
C_L/C_D	9.27
Angle of attack	4.37°
Mass	27.3 kg
Improvement in endurance (actual)	30.5%
Improvement in endurance (from iteration 1)	0.0003%

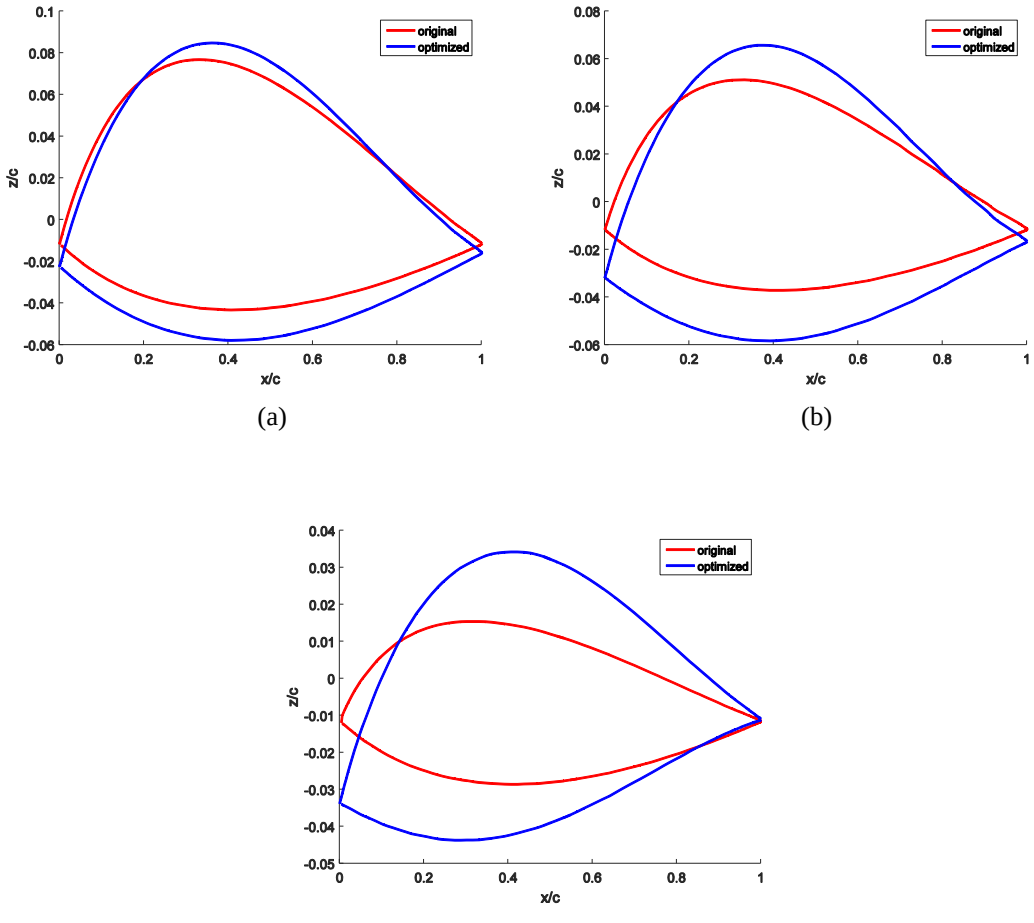

Figure 5.8 KittyHawk airfoil comparisons from airfoil optimization. (a) 54% span. (b) 72% span. (c) 90% span.

the thin airfoil sections. In addition to increased thicknesses, the leading edge of the outbound wing was pulled down, generating a negative twist. The increase in thickness is expected to increase the generated lift, but the optimizer creates geometric washout, which may counteract the benefits of the new airfoil. The effects of the new airfoils and angle of attack on the pressure distribution are shown in Figure 5.9. The contours of the upper surface pressure coefficient show that the leading edge pressure gradient has been reduced as the contour lines move aft on the aircraft. The minimum pressure region has also grown and does not reach the end of the leading edge sweep as for the original configuration. This low pressure region is where the large vortex forms as shown in Figure 5.6.

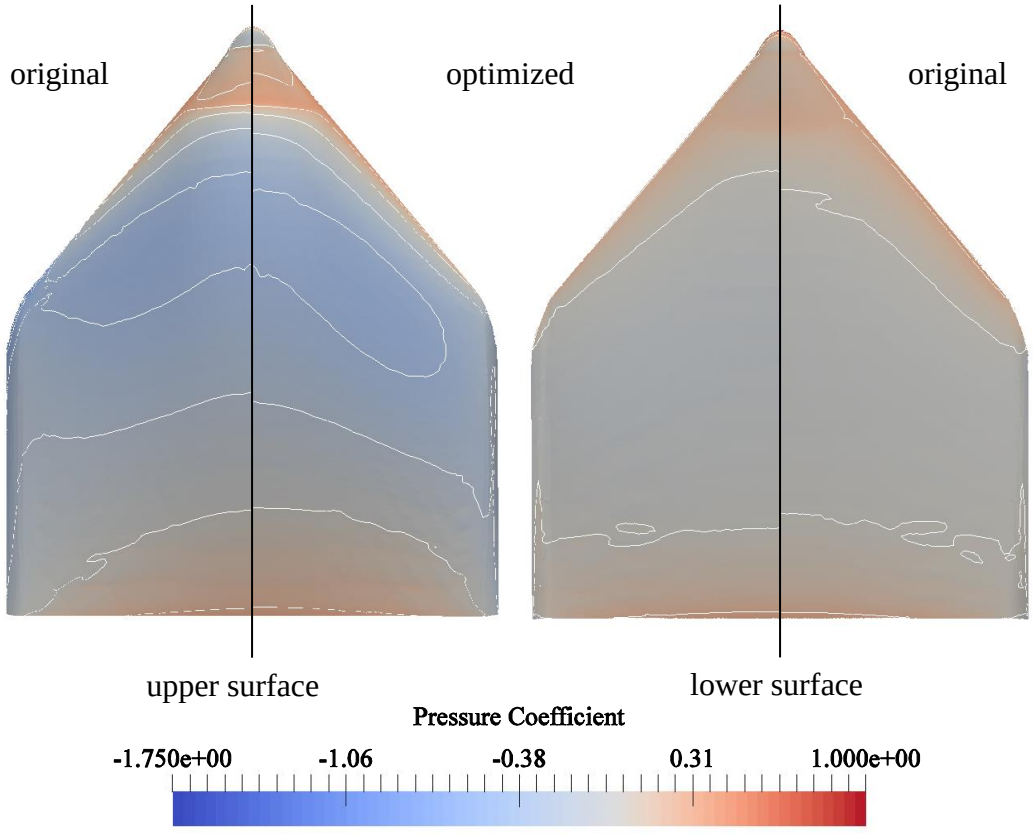

Figure 5.9 KittyHawk pressure coefficient comparisons from airfoil optimization.

The airfoil optimization was repeated with different bounds and the results were the same for the first iteration. After the first iteration, the optimizer did not find any new geometries that produced improved performance, even a small improvement as with the first airfoil optimization. In this optimization, the optimized solution was iteration 1 where the geometry was identical to the original but had reduced weight and angle of attack.

5.1.5 Three-dimensional Optimization

The final optimization of the KittyHawk was conducted with the FFD control points allowed to move in all three directions. The optimization iteration plots show similar behavior to those shown in Figure 5.4 for the planform degree of freedom, and thus are moved to Appendix D for reference. Thirty-eight configurations were searched until converging to the optimal solution with a normalized objective function value of 0.6949. The final optimized configuration loiters at 2.22° with a lift to drag ratio of 10.63. Again, as with all previous KittyHawk optimizations, there is an immediate 20% reduction in structural weight as the wing panel thicknesses are reduced. The new endurance for the aircraft is 55 minutes, a small improvement over the planform optimization with 43.9% change. The results are summarized in Table 5.8.

Table 5.8 KittyHawk optimized three-dimensional configuration characteristics.

Characteristic	Quantity
Endurance	55 minutes
C_L/C_D	10.63
Angle of attack	2.22°
Mass	28.4 kg
Improvement in endurance (actual)	43.9%
Improvement in endurance (from iteration 1)	10.3%

Like in the planform optimization, the planform of the KittyHawk is maximized, stretching the span and decreasing the sweep to the bounds of the problem as shown in Figure 5.10. In addition, the FFD points were displaced upwards along the span, creating a small dihedral as shown by the airfoil plots in Figure 5.11. In Figure 5.11 (c), the droop or high local camber of the trailing edge is caused by the small winglet on the KittyHawk. This is not the optimizer producing a large wash-in, but the result of a coarse FFD box for computational speed.

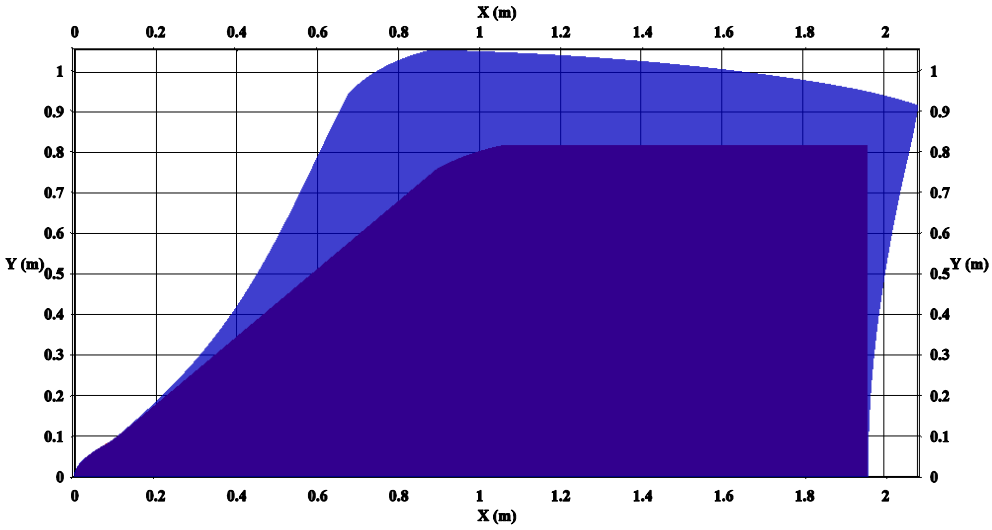

Figure 5.10 Optimized KittyHawk planform from three-dimensional optimization. Original shown in red (opaque region) and optimized shown in blue.

5.2 ONERA M6 WING

5.2.1 Configuration

The ONERA M6 wing is a popular CFD validation model used in over 100 software validations. Developed by ONERA in 1972, the wing features the symmetrical ONERA D airfoil and a moderate leading edge sweep [44]. The motivation for using the ONERA M6 wing in this work is its round leading edge found on most subsonic wing geometries. As discussed previously, airfoil optimization of the KittyHawk failed to produce significant

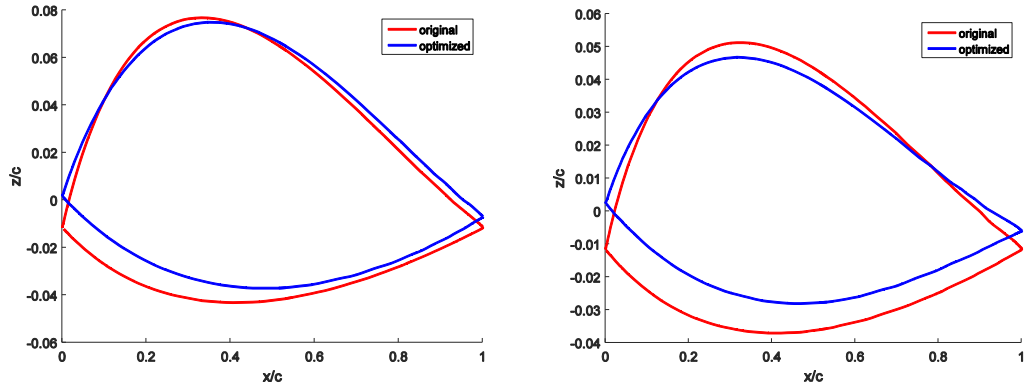

(a)

(b)

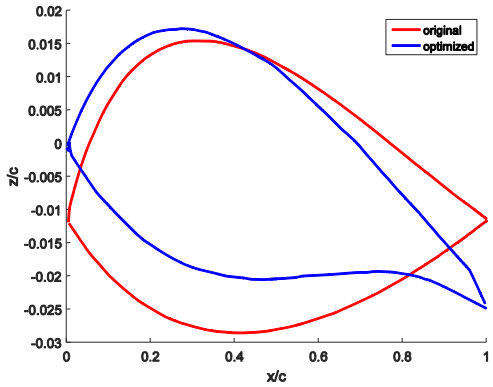

(c)

Figure 5.11 KittyHawk airfoil comparisons from three-dimensional optimization. (a) 54% span. (b) 72% span. (c) 90% span.

improvements aside from the reduction in weight. Primarily, optimizations of the ONERA M6 wing were performed to gain insight into the results of the KittyHawk airfoil optimization, but the geometry also serves as another test for the developed MDO tool.

The geometrical parameters of the ONERA M6 wing are listed in Table 5.9 and the weight breakdown is the same as shown in Table 5.4, excluding the airframe weight. For the ONERA M6 wing, the airframe weight is reduced such that the total mass is 25.7 kg. The reduction in airframe weight is done to eliminate the dramatic initial decrease as observed in the KittyHawk optimizations. The propulsion system is identical as described

Table 5.9 ONERA M6 wing initial planform characteristics.

Characteristic	Quantity
Span	2.39 m (7.84 ft)
Root chord	0.806 m (2.64 ft)
Taper ratio	0.562
Leading edge sweep angle	50°

Table 5.10 ONERA M6 initial configuration characteristics.

Characteristic	Quantity
Endurance	63 minutes
C_L/C_D	11.17
Angle of attack	4.44°
Mass	25.7 kg

in Table 5.3. The initial performance characteristics of the ONERA M6 wing are shown in Table 5.10.

5.2.2 Planform Optimization

Comparing Figure 5.12(a) to Figure 5.4(a), we see an immediate difference in the plots. Instead of a large initial decrease in weight, the ONERA M6 wing becomes heavier as the span is increased to obtain improved aerodynamic characteristics. Differences between the changes in the aerodynamic coefficients are found by comparing Figure 5.12(b) to Figure 5.4(b). For the KittyHawk, the lift and drag coefficients share the same shape, showing a tightly coupled relationship while the ONERA M6 optimization shows that drag minimization was the focus over increasing the lift. Figure 5.12(d) also shows that the change in aerodynamic coefficients for the ONERA wing is different from the KittyHawk since the angle of attack remains fixed, yet improvements are made. One reason for this could be the magnitude of the changes as the KittyHawk results are skewed

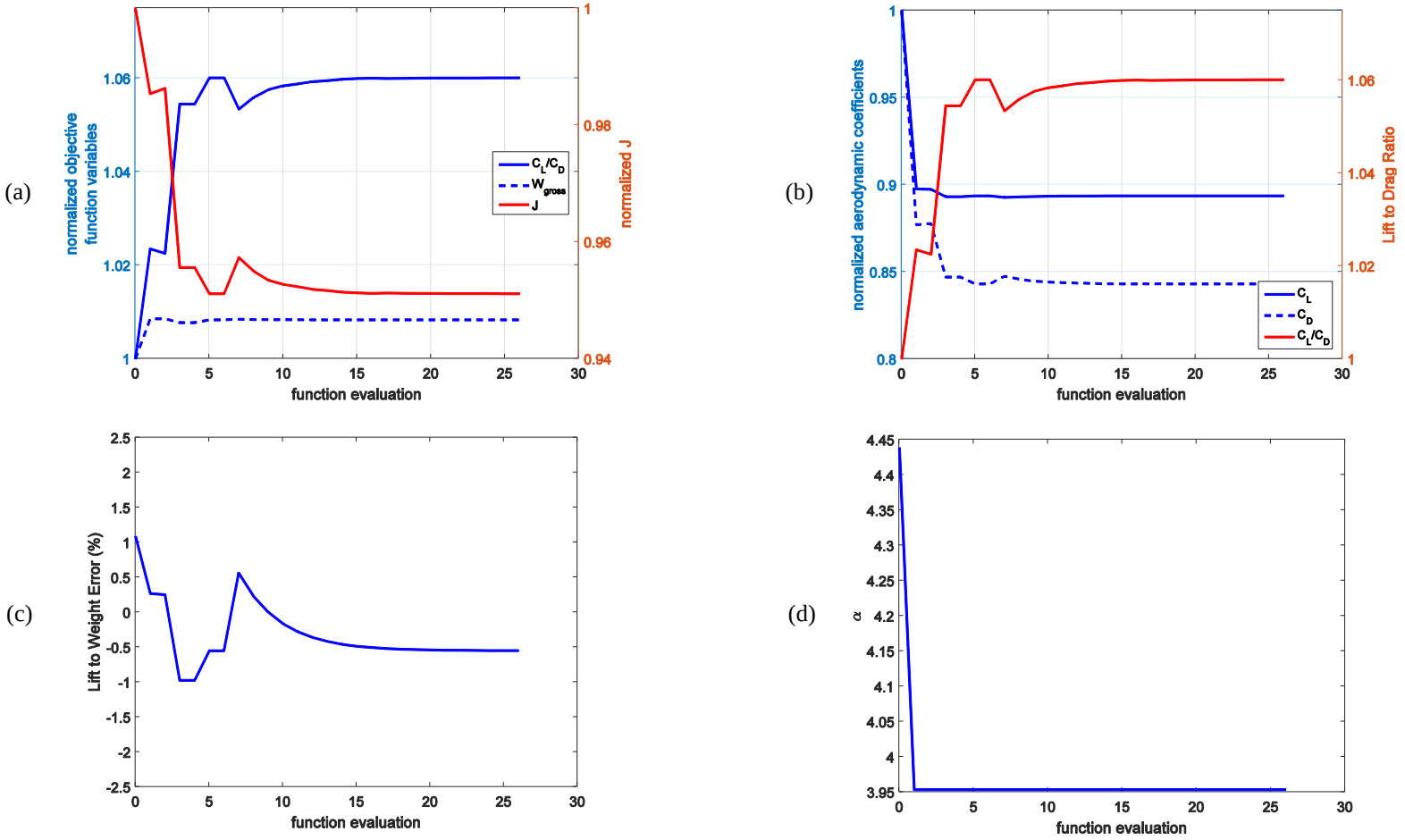

Figure 5.12 Optimization results for ONERA M6 with planform-related degree of freedom. (a) Primary optimization results. (b) Aerodynamic coefficients. (c) Consistency error. (d) Angle of attack.

by the large weight decrease, while the ONERA results are for a more reasonably weighted initial aircraft. Finally, Figure 5.12(c) shows that the solutions are again consistent for the ONERA M6 wing.

The new ONERA M6 planform yields a net improvement in endurance of 6.3%. As with the KittyHawk, the lift to drag ratio has increased along with the angle of attack. The maximum span has grown by 9% along with a slight decrease in the leading edge sweep as shown in Figure 5.13. The bounds of the wingtip FFD points were allowed to displace equal amounts, yet optimizer directly focuses on increasing the span along the latter half of the section. This movement in FFD points may be intended to produce a semi-

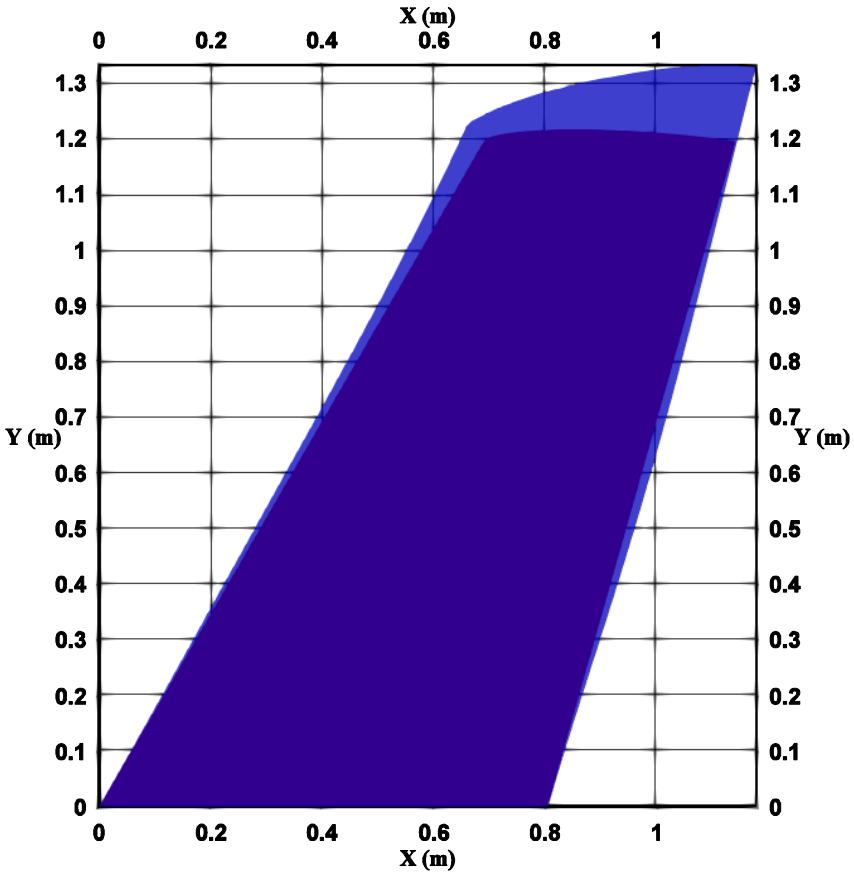

Figure 5.13 ONERA M6 planform comparison for planform optimization. Original shown in red (opaque region) and optimized shown in blue.

Table 5.11 ONERA M6 optimized planform configuration characteristics.

Characteristic	Quantity
Endurance	67 minutes
C_L/C_D	11.84
Angle of attack	3.95°
Mass	25.9 kg
Improvement in endurance	6.3%

elliptical planform which has the theoretical minimum induced drag. This may also explain why the lift coefficient remained relatively constant while the drag was further decreased. The improved performance characteristics are listed in Table 5.11 and show that the MDO tool can also effectively optimize the planforms of more conventional wing configurations.

5.2.3 Airfoil Optimization

While the planform optimizations for the KittyHawk and ONERA M6 had similar results, the airfoil optimizations were quite different. As discussed previously, the KittyHawk airfoil optimizations either increased the maximum thickness of the airfoil with washout or made no geometrical changes. The ONERA M6 airfoil optimization resulted in airfoils that remained nearly constant in maximum thickness, but had their camber increased dramatically. This change is expected, as the increased camber allows the wing to generate the necessary lift at a lower angle of attack. Along with the increased camber, there is a small negative twist down the span and a small dihedral. The airfoil comparisons for this optimization are shown in Figure 5.14. In Figure 5.15 the region allowed to deform is easily identified near the root of the wing. At the root, the concentrated low pressure region is still found as on the original wing. Further down the span, where the wing is allowed to deform, the pressure distribution becomes more distributed as the airfoils change shape. These changes improve the loiter performance of the configuration, but may

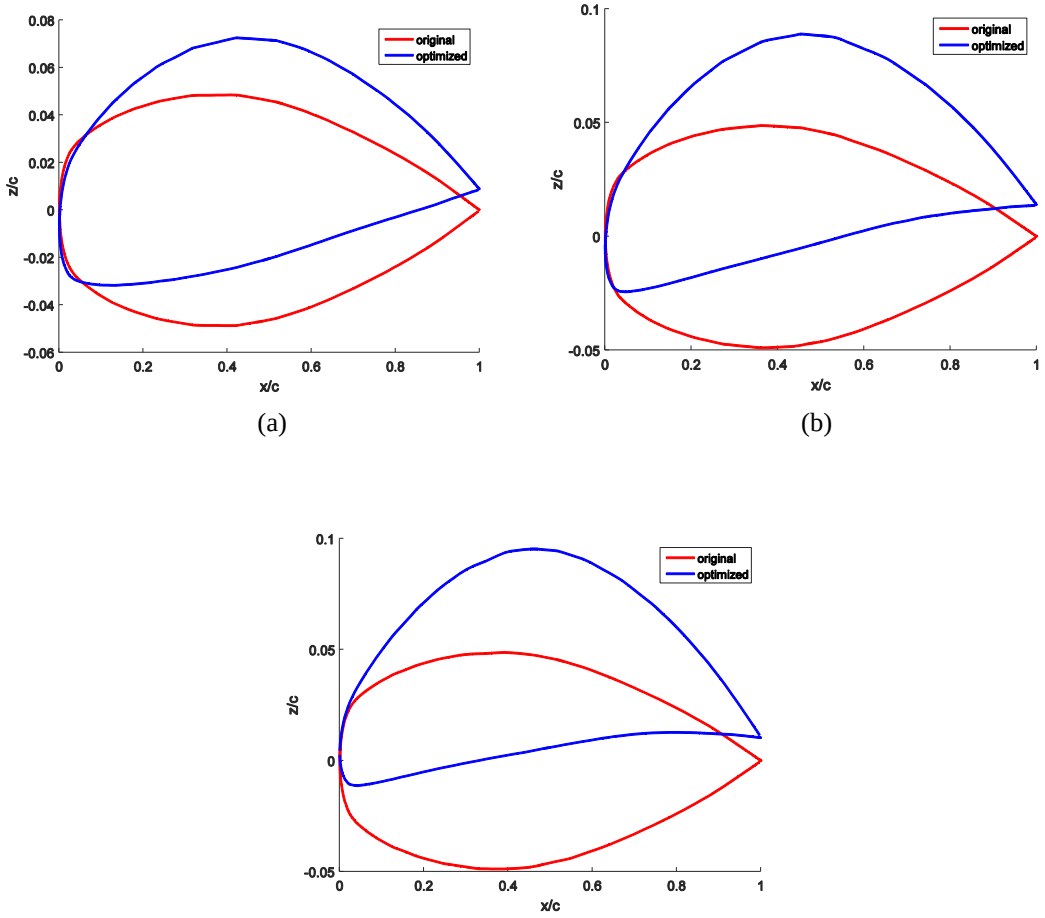

Figure 5.14 ONERA M6 airfoil comparisons from airfoil optimization. (a) 54% span. (b) 72% span. (c) 90% span.

have a negative effect during higher angles of attack due to the more adverse pressure gradient along the trailing edge.

Unlike any of the other optimizations thus far, the ONERA M6 airfoil optimization converged in only 6 iterations. The detailed iteration plots are found in Appendix E. The new camber allows the configuration to loiter at an angle of attack of 2.77° with a lift to drag ratio of 11.58. With the same weight as the initial weight, the optimized aircraft has an improvement in endurance of 4.8%. The performance summary is listed in Table 5.12.

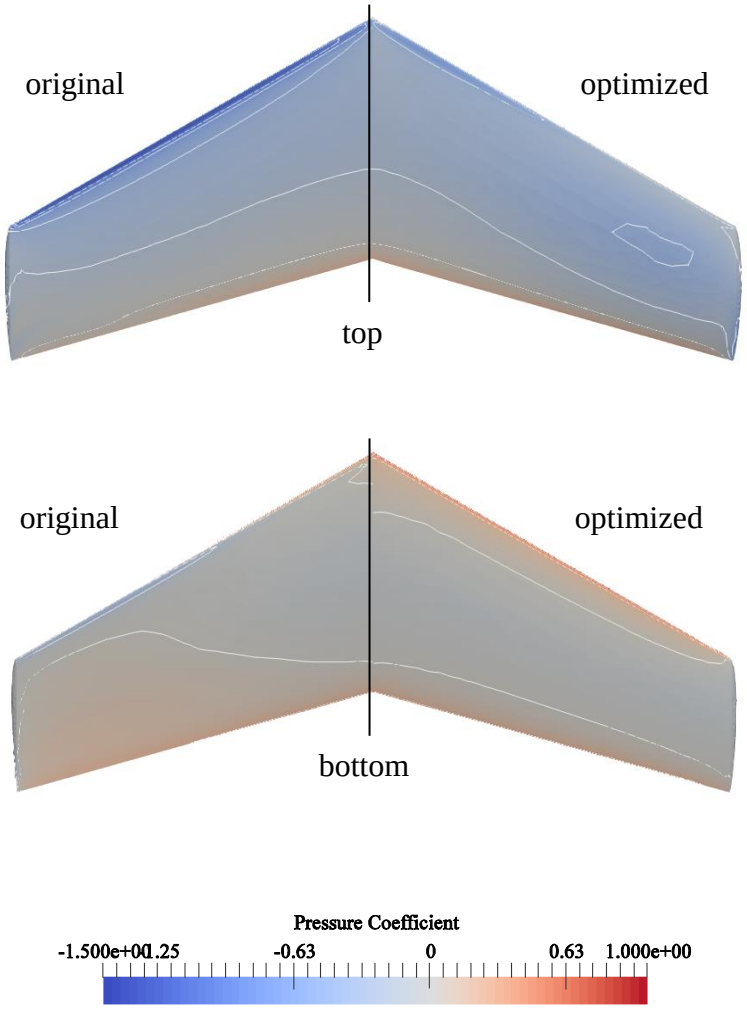

Figure 5.15 ONERA M6 pressure coefficient comparisons from airfoil optimization.

Table 5.12 ONERA M6 optimized airfoil configuration characteristics.

Characteristic	Quantity
Endurance	66 minutes
C_L/C_D	11.58
Angle of attack	2.77°
Mass	25.7 kg
Improvement in endurance	4.8%

Possibly the most significant result of the airfoil optimization is that the airfoils are clearly modified with matching performance improvements. The MDO tool can effectively perform optimizations with an airfoil-related degree of freedom on geometries with round leading edges.

5.2.4 Three-dimensional Optimization

The final ONERA M6 optimization was conducted with three degrees of freedom. As with the three-dimensional KittyHawk optimization, the optimizer is capable of making the greatest improvement to endurance by nearly doubling the improvements of the individual planform and airfoil optimizations. The optimum configuration, found with a normalized objective function value of 0.9021, has an 11.1 % improvement in endurance and loiters for 70 minutes. As with all previous optimizations, the lift to drag ratio has increased while the angle of attack decreased. The detailed optimization plots are found in Appendix E and the performance is summarized in Table 5.13.

Table 5.13 ONERA M6 optimized three-dimensional configuration characteristics.

Characteristic	Quantity
Endurance	70 minutes
C_L/C_D	12.42
Angle of attack	2.25°
Mass	25.7 kg
Improvement in endurance	11.1%

The optimized geometry of the ONERA M6 wing, shown in Figure 5.16, has suppressed features of the planform and airfoil optimized geometries. First, comparing the new geometry to that in Figure 5.13, we see an increase in span at the trailing edge. Instead of an overall decrease in leading edge sweep along the entire span as in the planform optimization, there is a section of wing near center span where the wing is displaced

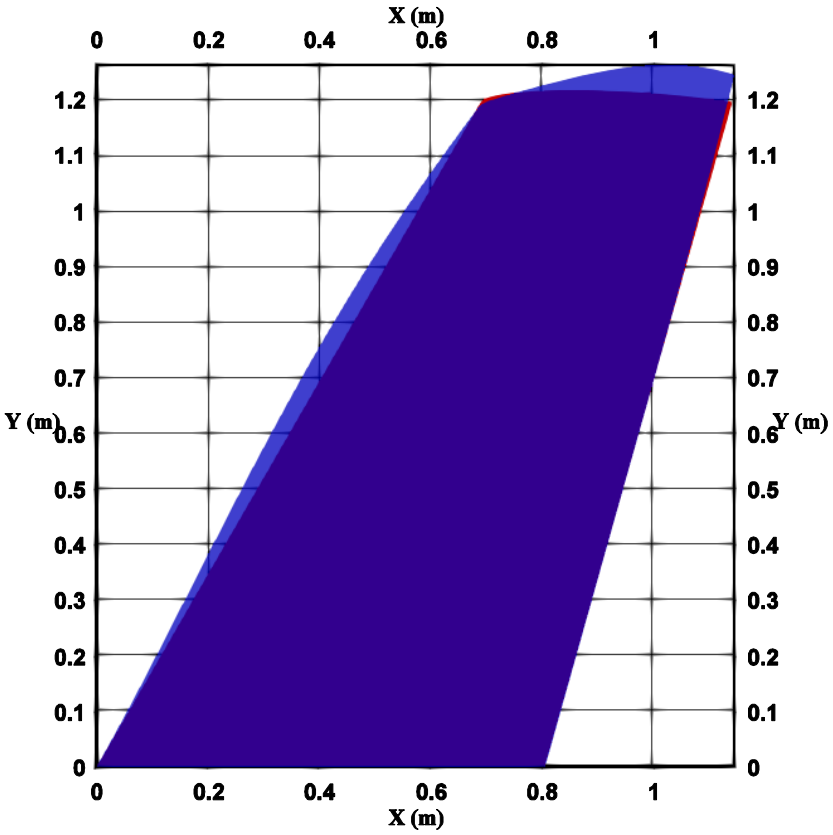

Figure 5.16 ONERA M6 planform comparison for three-dimensional optimization. Original shown in red (opaque region) and optimized shown in blue.

forward. The leading edge of the wingtip stays relatively fixed, producing another near-semi-elliptical planform. Like the airfoil optimization, the wing becomes cambered and obtains geometric twist. However, the camber at each airfoil section is reduced and the geometric twist is positive in contrast to the ONERA M6 airfoil optimization. Typically, positive twist is not used on the outboard wing sections as this may cause these sections to stall first. Most ailerons are located in this region, thus, stalling the outboard wing may cause loss of control. The new cambered airfoils and twist are shown in Figure 5.17. Overall, the planform modifications are reduced due to the airfoil changes and vice versa.

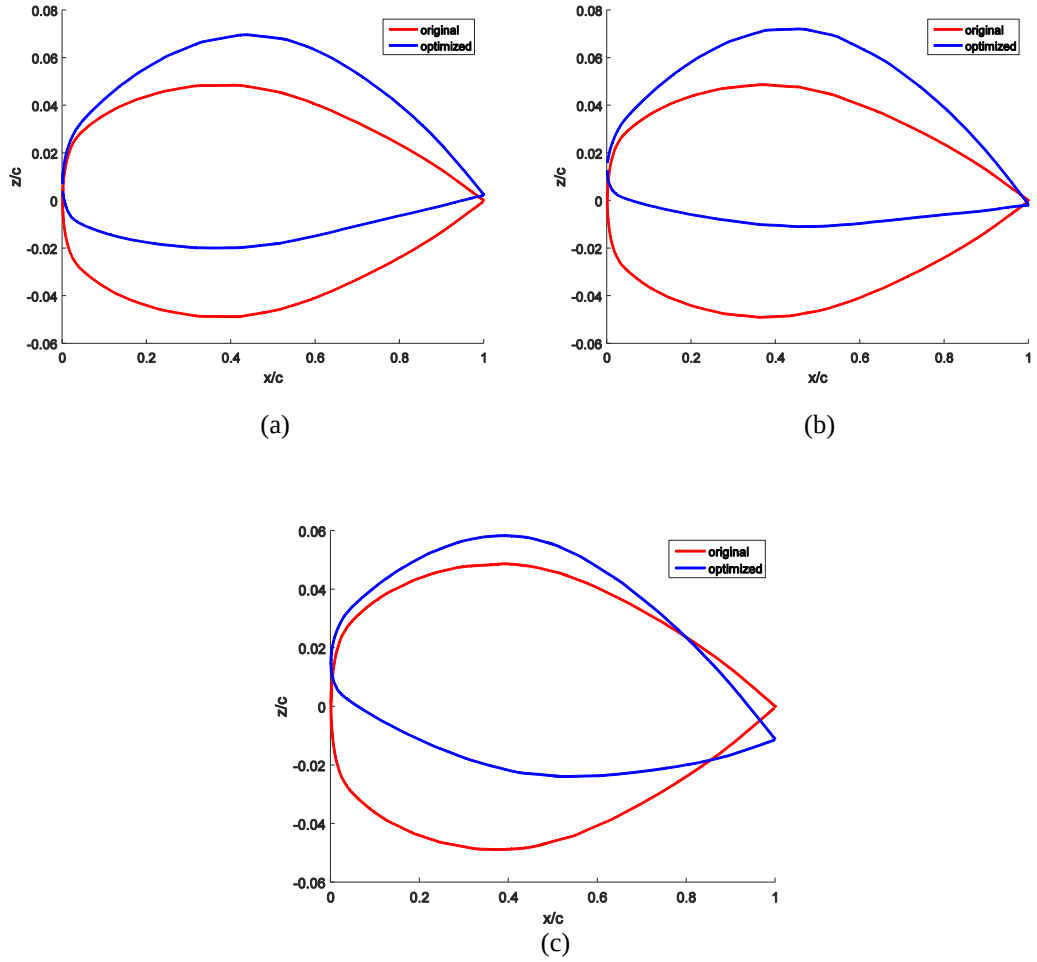

Figure 5.17 ONERA M6 airfoil comparisons from three-dimensional optimization. (a) 54% span. (b) 72% span. (c) 90% span.

5.3 MODIFIED ONERA M6

5.3.1 Configuration

The final test geometry is a modified version of the ONERA M6 wing. The original geometry was imported into a CAD system, where the model [45] was modified to have sharp leading edges as shown in Figure 5.18. The modifications to the airfoil start at 25% chord along the entire span, ending at the original leading edge and are mirrored on the upper and lower surfaces such that the initial geometry remains symmetric. While the leading edge shape changed, the modified ONERA M6 planform is identical to that of the

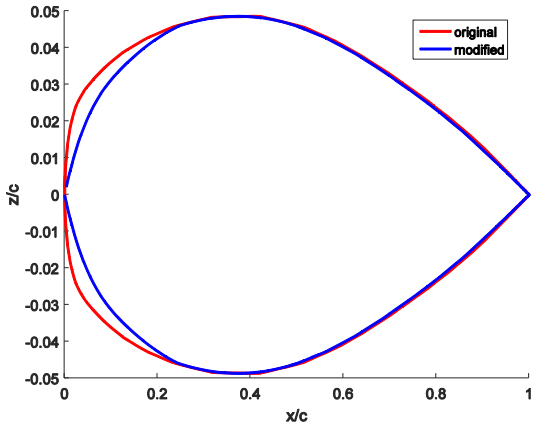

Figure 5.18 Airfoil comparison of original and modified ONERA M6.

Table 5.14 Modified ONERA M6 initial configuration characteristics.

Characteristic	Quantity
Endurance	70 minutes
C_L/C_D	12.35
Angle of attack	4.64°
Mass	25.7 kg

original geometry listed in Table 5.9. The remaining characteristics of the initial configuration are listed in Table 5.14.

The motivation for modifying the ONERA M6 geometry stems from the airfoil optimization results from the KittyHawk and original ONERA M6. In recapitulation, when investigating the KittyHawk the optimizer changed the airfoils with little effect in one run and did not modify them in another. However, the ONERA optimizations showed clear airfoil modifications and improvements. One of the key differences between the KittyHawk and ONERA M6 geometries is the leading edge shape. The modified ONERA

M6 geometry was created to help determine the effects of sharp leading edges on the optimization results.

5.3.2 Airfoil Optimization

Like the airfoil optimization for the original ONERA M6, the airfoil optimization for the modified wing converges in very few iterations, shown in Appendix F. Another similarity between the two optimizations is the optimized geometry. The optimizer increases the camber of the airfoil sections in Figure 5.19 and generates a negative twist like that shown in Figure 5.14. The optimized wing benefits from a 14.3% improvement in

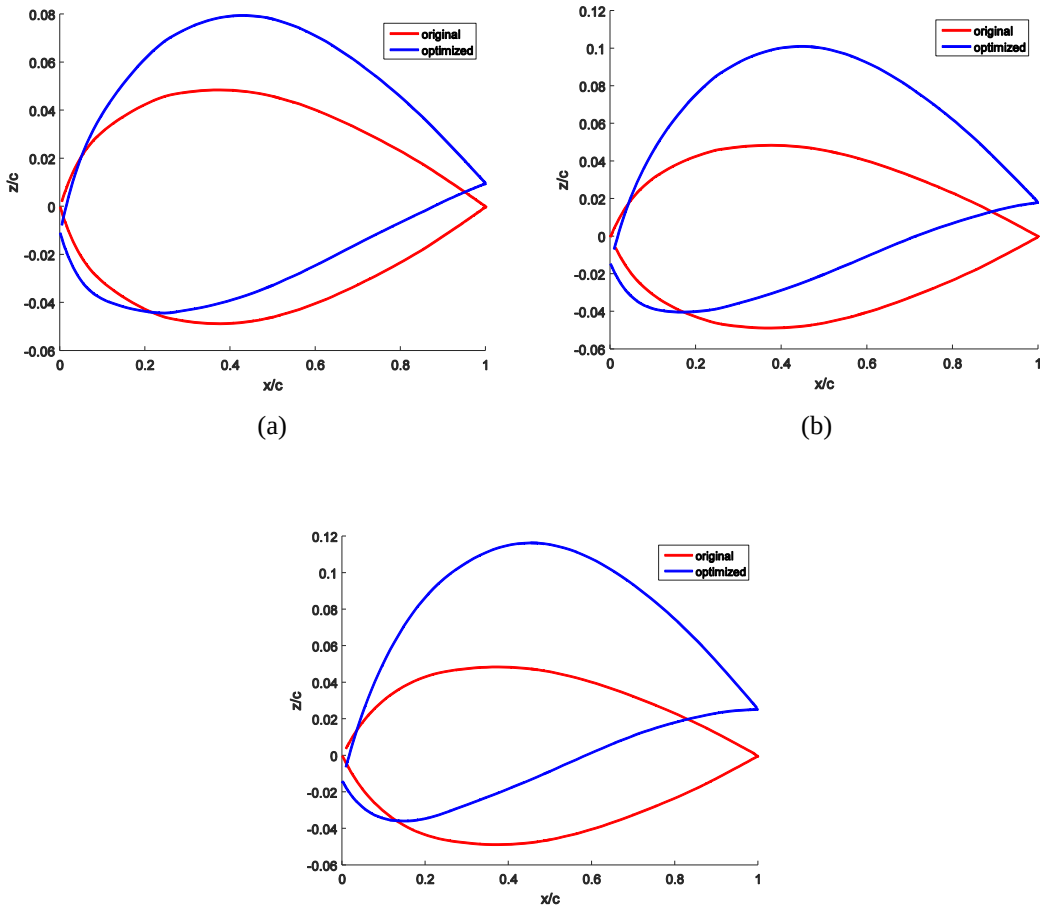

Figure 5.19 Modified ONERA M6 airfoil comparisons from three-dimensional optimization. (a) 54% span. (b) 72% span. (c) 90% span.

endurance, made possible by a new lift to drag ratio of 14.01 and a loiter angle of attack of 3.10°. The gross weight of the wing remained constant and the improved performance is summarized in Table 5.15. The results once again show that the MDO tool is effective at optimizing the geometry, but also yields the conclusion that sharp edges are not the culprit in the KittyHawk airfoil optimizations.

Table 5.15 Modified ONERA M6 optimized airfoil configuration characteristics.

Characteristic	Quantity
Endurance	80 minutes
C_L/C_D	14.01
Angle of attack	3.10°
Mass	25.7 kg
Improvement in endurance	14.3%

5.4 GEOMETRY COMPARISONS

There are five key differences between the KittyHawk and ONERA M6 geometries: planform shape, aspect ratio, wing thickness, leading edge shape, and wing tip shape. Given the results of the modified ONERA M6 optimization, it was concluded that leading edge shape is not the cause for the KittyHawk optimizations with airfoil-related degree of freedom to not produce clear and consistent results. After the modified ONERA M6 optimization, the first action was to return to the KittyHawk and double the orders of the FFD box in the chord and span directions, providing more control over the geometry. The results, shown in Figure D.4 of Appendix D, were nearly identical to the first airfoil KittyHawk case. The only significant improvement resulted from the decrease in weight and angle of attack, while the geometrical changes did not affect the performance.

The difference in the two geometries along the spanwise direction is quite drastic. Figure 5.20 shows the thickness to chord ratio and thickness for the KittyHawk and

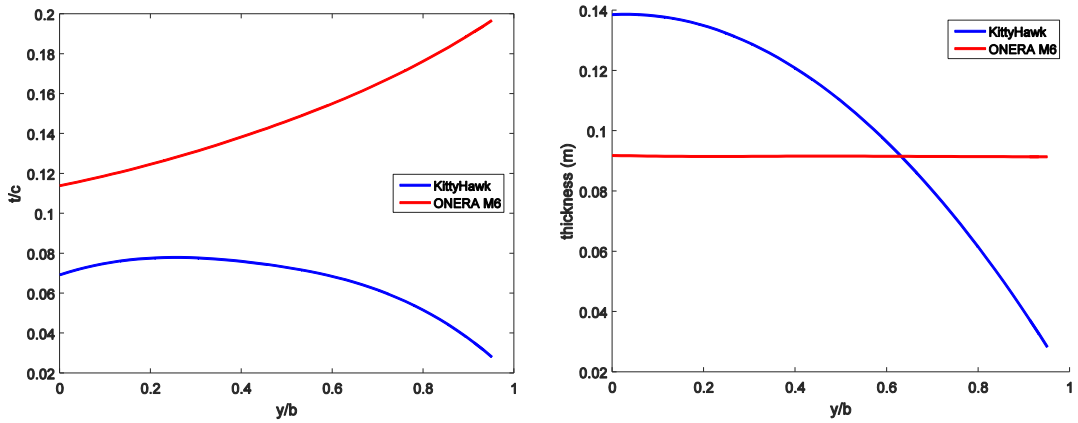

Figure 5.20 KittyHawk and ONERA M6 spanwise comparisons. (a) Thickness to chord ratio vs. nondimensionalized span. (b) Thickness vs. nondimensionalized span.

ONERA M6 along their nondimensionalized spans. From Figure 5.20(a) it is shown that the KittyHawk's airfoils reduce in thickness more quickly than in chord length, even though there is a 50° leading edge sweep. Figure 5.20(b) shows just how drastic the thickness change of the KittyHawk's airfoils is to that of the ONERA M6. The minimum measured airfoil thickness of the KittyHawk is 2.8 cm, a 79.5% reduction in thickness in only 68% of the span of the ONERA M6 wing. This may explain why the deformations made by the optimizer in the KittyHawk airfoil case were more focused on increasing thickness.

The aspect ratio of the two configurations is also very different, where the KittyHawk and ONERA M6 have aspect ratios of 1.10 and 3.76 respectively. There is more blended-body than blended-wing in the KittyHawk configuration. This causes very different spanwise flow characteristics, shown in Figure 5.21. On the KittyHawk we see that the flow changes directions further aft of the leading edge than on the ONERA wings. The initial positive spanwise flow is caused by the leading edge sweep and sharp leading

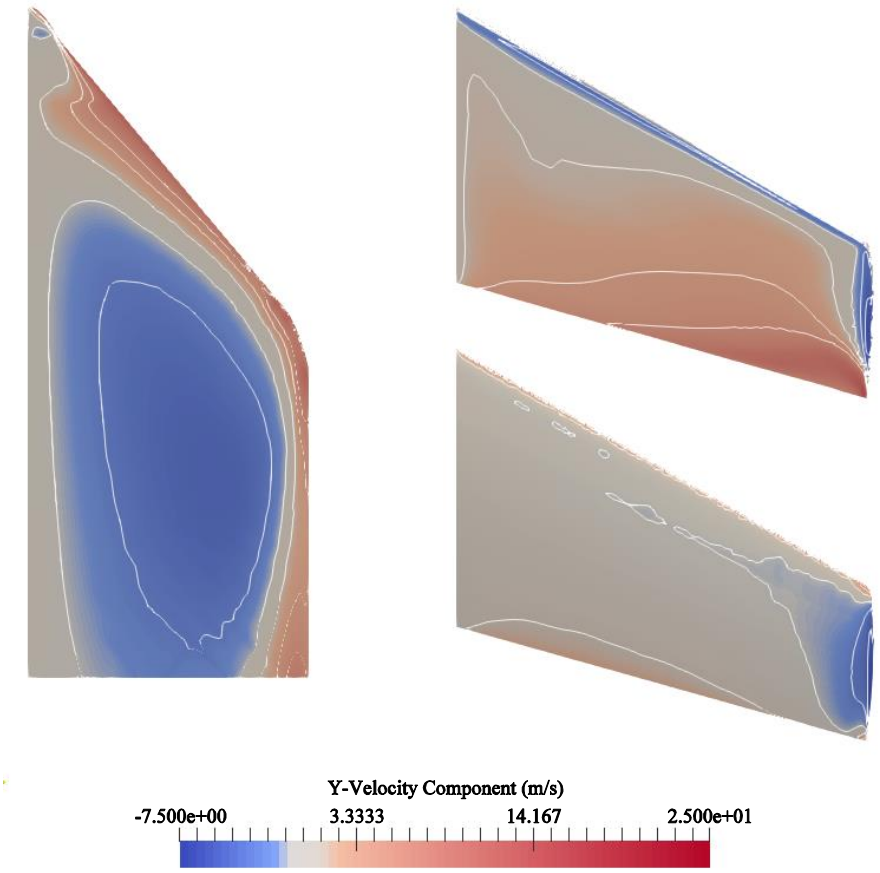

Figure 5.21 Spanwise velocity on top surface of (a) KittyHawk, (b) ONERA M6 wing, and (c) modified ONERA M6 wing. The off-white region spans between -1 and 1 m/s.

edges. The flow then makes a significant turn and flows inboard. This is thought to be caused by the flow "wrapping" around the bulbous body of the KittyHawk. Most BWB configurations have discernable wings blended into the fuselage section, unlike the KittyHawk. The flow direction transition along the wing tip of the KittyHawk has a steeper gradient and is caused by the vortex that forms on the leading edge of the tip chord "re-attaching" to the surface. The flow is not technically separating and re-attaching since the simulation is inviscid; rather, these vortices are caused by the numerical solution along the sharp edges. The vortex reattachment is caused by both the downward facing winglet and

the delta wing nature of the KittyHawk. On the ONERA wings, the opposite is shown where the outboard flow and inboard flow meet, indicating possible flow detachment in a viscous flow. Overall, the spanwise flow is outboard or chordwise for the ONERA configurations, while the KittyHawk has a large region of inboard flow. The large amount of inboard flow, small aspect ratio, and extremely thin airfoil sections may be too much for the optimizer to overcome with only an airfoil-related degree of freedom within the given boundaries of the problem. This makes the span of the KittyHawk much more sensitive than the airfoil sections.

CHAPTER 6

CONCLUSIONS AND FUTURE WORK

Using gradient-based optimization and an architecture based on MDF, a MDO tool was developed by coupling the SU2 CFD analysis suite and the wing weight estimator EMWET. Special attention was given to the inputs and sequence of the optimization modules such that the MDO tool performs analyses efficiently with a robust construction. In conclusion, the results of the optimizations conducted and discussed in Chapter 5 for the various configurations show that the newly developed MDO tool can effectively improve endurance and range performance for battery-powered aircraft. In all cases studied, planforms with both round and sharp leading edges were effectively modified. However, some concern remains as to why optimizations with an airfoil-related degree of freedom failed to significantly improve the KittyHawk's performance. Currently, the MDO tool is best suited for early preliminary design, where large changes in geometry are productive, but also permittable and allowed to be incorporated into the design.

While the optimizations conducted in this work are productive in improving the initial configurations, they are only preliminary optimizations conducted with a coarse FFD box to test and validate the methods and decisions made during the construction of the MDO tool. Performance may be further improved when the number of control points is increased, especially in the spanwise direction, allowing more of the geometry to be deformed.

Now that the base MDO tool has been developed, there is much more that can be inserted into the optimization routine. The first and simplest addition is using a full CFD domain, rather than using a symmetry plane at the root chord. This will increase run time, however, it will allow the full FFD box to deform, including the root section if desired. This may prove beneficial to geometries similar to the KittyHawk. This extra freedom would provide more control over the KittyHawk's rapid airfoil thickness decrease by allowing both the outboard and inboard sections to increase and decrease in thickness respectively. The full domain could also be used in post optimization studies for other flight segments and for stability and control studies.

The next module to be added to the MDO tool would be for stability. Longitudinal stability analyses could be performed with the current configuration using the half domain. For this module to work, the mass items of the configuration would be required to have x, y, and z-locations for the items' center of mass. With this information, longitudinal static stability constraints could be added, helping ensure that the modified geometry remains an effective and stable aircraft. This is especially important for BWB aircraft, which lack a horizontal tail, requiring more control surface deflection to trim which causes more drag, or more design finesse such as convex airfoil trailing edges. The work of Mialon et al [2] has shown that the pitching moment is the hardest constraint to satisfy, as well as having the greatest effect on the final aerodynamic performance.

REFERENCES

[1] R. H. Liebeck, "Design of the Blended Wing Body Subsonic Transport," *Journal of Aircraft,* vol. 41, no. No. 1, pp. 10-25, 2004.

[2] B. Mialon, T. Fol and C. Bonnaud, "Aerodynamic Optimization of Subsonic Flying Wing Configurations," American Institute of Aeronautics and Astronautics, 2002.

[3] D. P. Raymer, Aircraft Design: A Conceptual Approach, 5th ed., J. A. Schetz, Ed., Reston: American Institute of Aeronautics and Astronautics, Inc., 2012.

[4] Z. Lyu and J. R. R. A. Martins, "Aerodynamic Design Optimization Studies of a Blended-Wing-Body Aircraft," *Journal of Aircraft,* vol. 51, no. No. 5, pp. 1604-1617, 2014.

[5] N. G. Verhaagen, "Effects of Leading-Edge Radius on Aerodynamic Characteristics of 50 degree Delta Wings," *48th AIAA Aerospace Sciences Meeting Including the New Horizons Forum and Aerospace Exposition,* 4-7 January 2010.

[6] J. D. Anderson, Jr., Fundamentals of Aerodynamics, 4th ed., New York: McGraw-Hill, 2007.

[7] I. Gursul, R. Gordnier and M. Visbal, "Unsteady Aerodynamics of Nonslender Delta Wings," *Progress in Aerospace Sciences,* vol. 41, pp. 515-557, 2005.

[8] R. E. Gordnier and M. R. Visbal, "High-Order Compact Difference Scheme applied to the Simulation of a Low Sweep Delta Wing Flow," January 2003.

[9] J. M. Rullan, *The Aerodynamics of Low Sweep Delta Wings,* Blackburg, Virginia: Virginia Polytechnic Institute and State University, 2008.

[10] M. Hepperle, "Electric Flight - Potential and Limitations," in *AVT-209 Workshop on Energy Efficient Technologies and Concepts Operation*, Libson, 2012.

[11] B. M. Kulfan and J. E. Bussoletti, ""Fundamental" Parametric Geometry Representations for Aircraft Component Shapes," in *11th AIAA/ISSMO Multidisciplinary Analysis and Optimization Conference*, Portsmouth, 2006.

[12] B. M. Kulfan, "A Universal Parametric Geometry Representation Method - "CST"," in *45th AIAA Aerospace Sciences Meeting and Exhibit*, Reno, 2007.

[13] F. Palacios, M. R. Colonno, A. C. Aranake, A. Campos, S. R. Copeland, T. D. Economon, A. K. Lonkar, T. W. Lukaczyk, T. W. R. Taylor and J. J. Alonso, "Stanford University Unstructured (SU2): An open-source integrated computational environment for multi-physics simulation and design.," *51st AIAA Aerospace Sciences Meeting including the New Horizons Forum and Aerospace Exposition*, 2013.

[14] T. W. Sederberg and S. R. Parry, "Free-Form Deformation of Solid Geometric Models," *Association for Computing Machinery*, vol. 20, no. 4, pp. 151-160, 1986.

[15] J. R. R. A. Martins and A. B. Lambe, "Multidisciplinary Design Optimization: A Survey of Architectures," *AIAA Journal*, vol. 51, no. No. 9, pp. 2049-2075, 2013.

[16] E. J. Cramer, J. E. Dennis Jr., P. D. Frank, R. M. Lewis and G. R. Shubin, "Problem Formulation for Multidisciplinary Optimization," *SIAM Journal on Optimization*, vol. 4, no. 4, pp. 754-776, 1994.

[17] A. B. Lambe and J. R. R. A. Martins, "Extensions to the Design Structure Matrix for the Description of Multidisciplinary Design, Analysis, and Optimization Processes," *Structural and Multidisciplinary Optimization*, vol. 46, pp. 273-284, 2012.

[18] M. Drela and H. Youngren, "XFOIL: Subsonic Airfoil Development System," Massachusetts Inst. of Technology, Cambridge, 2008.

[19] N. Qin, A. Vavalle, A. Le Moigne, M. Laban, K. Hackett and P. Weinerfelt, "Aerodynamic considerations of blended wing body aircraft," *Progress in Aerospace Sciences*, vol. 40, pp. 321-343, 2004.

[20] S. Copeland, "SU2 Tools," Stanford University, 30 July 2014. [Online]. Available: http://adl-public.stanford.edu/docs/display/SUSQUARED/SU2+Tools.

[21] F. Palacios, T. D. Economon, A. C. Aranake, S. R. Copeland, A. K. Lonkar, T. W. Lukaczyk, D. E. Manosalvas, K. R. Naik, A. S. Padron, B. Tracey, A. Variyar and J. J. Alonso, "Stanford University Unstructured (SU2): Open-source Analysis and Design Technology for Turbulent Flows," in *AIAA SciTech*, National Harbor, MD, 2014.

[22] F. Palacios, T. D. Economon, A. D. Wendorff and J. J. Alonso, "Large-scale aircraft design using SU2," in *AIAA SciTech*, Kissimmee, 2015.

[23] T. D. Economon, F. Palacios, J. J. Alonso, G. Bansal, D. Mudigere, A. Deshpande, A. Heinecke and M. Smelyanskiy, "Towards High-Performance Optimizations of the Unstructured Open-Source SU2 Suite," in *AIAA SciTech*, Kissimmee, 2015.

[24] M. Drela and H. Youngren, "Athena Vortex Lattice (AVL)," Massachusetts Inst. of Technology, Cambridge, 2011.

[25] A. Elham, G. La Rocca and M. J. L. van Tooren, "Development and Implementation of an Advanced, Design-Sensitive Method for Wing Weight Estimation," *Aerospace Science and Technology*, vol. 29, pp. 100-113, 2013.

[26] E. Torenbeek, "Development and Application of a Comprehensive, Design-Sensitive Weight Prediction Method for Wing Structures of Transport Category Aircraft," Delft University of Technology, Delft, 1992.

[27] *MATLAB*, Natick, MA: The MathWorks Inc., 2014.

[28] The Division of Information Technology, "High Performance Computing Resources," University of South Carolina, [Online]. Available: https://www.sc.edu/about/offices_and_divisions/division_of_information_technology/rci/hpc_resources/. [Accessed October 2016].

[29] ANSYS, *ICEM CFD 16.0*, Cononsburg, 2014.

[30] Sandia Corporation, Kitware Inc., *ParaView 5.0.0*, Albuquerque, NM, Clifton Park, NY, 2015.

[31] S. J. Hulshoff, *CFD II Part 2: Computation and Modelling of Turbulence*, Delft: Delft University of Technology, 2015.

[32] P. R. Spalart and S. R. Allmaras, "A One-Equation Turbulence Model for Aerodynamic Flows," *Recherche Aerospatiale*, vol. No. 1, pp. 5-21, 1994.

[33] F. R. Menter, "Two-Equation Eddy-Viscosity Turbulence Models for Engineering Applications," *AIAA Journal*, vol. 32, no. 8, pp. 1598-1605, 1994.

[34] LEAP CFD Team, "Tips & Tricks: Turbulence Part 1-Introduction to Turbulence Modelling," 25 May 2012. [Online]. [Accessed 2015].

[35] P. C, *Pre-conditioners for low Mach number flows*, Bangalore: Tata Institute of Fundamental Research: Center of Applicable Mathematics, 2013.

[36] M. Uygun and K. Kirkkopru, "Numerical Solution of the Euler Equations by Finite Volume Methods: Central versus Upwind Schemes," *Journal of Aeronautics and Space Technologies*, vol. 2, no. 1, pp. 47-55, 2005.

[37] C. Viozat, "Implicit Upwind Schemes for Low Mach Number Compressible Flows," 1997.

[38] H. Bijl, A. van Zuijlen, A. de Boer and D. J. Rixen, *Fluid-structure interation: An introduction to numerical coupled simulation*, Delft: Delft University of Technology, 2008.

[39] O. Zikanov, Essential Computational Fluid Dynamics, Hoboken, New Jersey: John Wiley & Sons, Inc., 2010, pp. 118-119.

[40] J. D. Anderson, Jr., Computational Fluid Dynamics: The Basics with Applications, New York: McGraw-Hill, Inc., 1995, pp. 450-451.

[41] L. M. Soltmann, "KittyHawk prototype CFD data," Raleigh, 2014.

[42] Chomarat North America, "C_PLY BX 0/-45 150 C3.4 12K HS," Chomarat, Williamston, SC, 2015.

[43] Cytec, "MTM 45-1," Cytec Industries Inc., Woodland Park, 2012.

[44] S. Gaultier, "ONERA-M6 Wing, Star of CFD," ONERA, 28 May 2013. [Online]. Available: http://www.onera.fr/en/actualites/image-du-mois/onera-m6-wing-star-cfd. [Accessed 6 March 2017].

[45] C. Rumsey, "Turbulence Modeling Numerical Analysis 3D ONERA M6 Wing Validation Case," NASA Langley Research Center, 16 December 2016. [Online]. [Accessed March 2017].

APPENDIX A

EXAMPLE RUN FILES

aerodynamic.txt

```
%% AERODYNAMIC CONSTANTS
% ------ incompressible only ------ % must be filled in regardless
% freestream density (kg/m^3)
opt.aero.rho            =       1.1673
% freestream velocity (m/s)
opt.aero.V              =       31
% freestream dynamic viscosity
opt.aero.mu             =       1.77E-5
% ------- compressible only ------- % must be filled in regardless
% freestream Mach number
opt.aero.mach           =       0.8395
% freestream speed of sound (m/s)
opt.aero.Ssound         =       341
% freestream pressure (Pa)
opt.aero.pres           =       101325
% freestream temperature (K)
opt.aero.temp           =       288.15
% Reynolds length
opt.aero.ReL            =       1.0
% freestream Reynolds number
opt.aero.Re             =       6.5E6
% freestream angle of attack (degrees)
opt.aero.aoa            =       4.547

% incompressible(i) or compressible(c)
opt.aero.regime         =       i
% viscous(v) or inviscid(i)
opt.aero.visc           =       i
% turbulence model (NONE, SA, SST)
opt.aero.turb           =       NONE
```

case_data.txt

```
%% OPTIMIZATION CONSTANTS
% Objective Function Selection
% 1=Endurance, 2=Range
opt.case            =       1
% number of wing sections used (2-5)
opt.n_secs          =       5
% number of processors
opt.sys.n_proc      =       20
```

mesh_data.txt

```
%% MESH DATA
% body marker name
opt.mesh.mark.body          =       BODY
% farfield marker name
opt.mesh.mark.farf          =       RIGHT, TOP, BOTTOM, INLET, OUTLET
% symmetry plane marker name
opt.mesh.mark.symm          =       SYM
% original mesh name (with FFD, undeformed)
opt.mesh.mesh_in            =       mesh.su2
% "surface_grid.dat" start and end rows for import
opt.mesh.mesh_read_ind      =       56584
opt.mesh.mesh_read_ind      =       75523
```

propulsion.txt

```
%% PROPULSION CONSTANTS
% battery hour rating (hours)
opt.J.Rt        =       1
% total efficiency
opt.J.eta_tot   =       0.80
% battery output power (volts)
opt.J.V         =       37
% battery capacity (ampere hours)
opt.J.C         =       5
% number of batteries
opt.J.n_batt    =       5
% battery mass (kg)
opt.J.m_batt    =       1.1612
```

weight.txt

```
%% WEIGHT CONSTANTS (kg)
% Maximum Take-Off Weight
opt.W.MTOW          =       34.2009
% Equipment Weight (avionics, ESC, servos, wiring, pitot)
opt.W.Equip         =       2.5247
% Propulsion Weight (motor, propeller) !!! DOES NOT INCLUDE BATTERIES
opt.W.Prop          =       1.1178
% Other Airframe Weight (vertical tails, landing gear, lead balance)
opt.W.Frame         =       5.310
% Access. Weight
opt.W.Access        =       8.661
```

fmincon_options.txt

```
%% FMINCON OPTIONS
Algorithm       sqp
Display         iter-detailed
MaxIter         25
TolX            1E-4
TolCon          0.001
TolFun          1E-6

% TolCon default = 1E-6
% TolFun default = 1E-6
% TolX default = 1E-6 for all except interior point (1E-10)
% ObjectiveLimit default = -1E20
```

ffd.txt

```
%% FFD DATA
% FFD edge orders
opt.FFD.l       =       3
opt.FFD.m       =       4
opt.FFD.n       =       1

% X Constraints (by plane)
i               =
j               =       0 1
k               =

% Y Constraints (by plane)
i               =
j               =       0 1
k               =

% Z Constraints (by plane)
i               =       3
j               =       0 1
k               =

% FFD Box Name
name            =       BOX
% FFD Box Surface
surf            =       BODY
```

bounds.xlsx

xl				
-0.35	-0.305	-0.26	-0.26	-0.26
-0.35	-0.305	-0.26	-0.215	-0.17
-0.35	-0.305	-0.26	-0.215	-0.17
-0.015	-0.015	-0.015	-0.015	-0.015
xu				
0.015	0.015	0.015	0.015	0.015
0.35	0.305	0.26	0.215	0.17
0.35	0.305	0.26	0.215	0.17
0.35	0.305	0.26	0.215	0.17
yl				
0	-0.11	-0.11	-0.11	-0.025
0	-0.11	-0.11	-0.11	-0.025
0	-0.11	-0.11	-0.11	-0.025
0	-0.11	-0.11	-0.11	-0.025
yu				
0	0.11	0.11	0.11	0.3
0	0.11	0.11	0.11	0.3
0	0.11	0.11	0.11	0.3
0	0.11	0.11	0.11	0.3
zl				
-0.025				
-0.006				
zu				
0.025				
0.025				

APPENDIX B

EXAMPLE SU2 CONFIGURATION FILE

```
%%%
```

LIMITER_COEFF= 0.3
LIMITER_ITER= 999999
LINEAR_SOLVER= FGMRES
LINEAR_SOLVER_PREC= LU_SGS
LINEAR_SOLVER_ERROR= 1E-5
LINEAR_SOLVER_ITER= 5
MGLEVEL= 2
MGCYCLE= V_CYCLE
MG_PRE_SMOOTH= (1, 2, 3, 3)
MG_POST_SMOOTH= (0, 0, 0, 0)
MG_CORRECTION_SMOOTH= (0, 0, 0, 0)
MG_DAMP_RESTRICTION= 0.9
MG_DAMP_PROLONGATION= 0.9
CONV_NUM_METHOD_FLOW= ROE
SPATIAL_ORDER_FLOW= 2ND_ORDER_LIMITER
SLOPE_LIMITER_FLOW= VENKATAKRISHNAN
VISCOUS_LIMITER_FLOW= NO
TIME_DISCRE_FLOW= EULER_IMPLICIT
RELAXATION_FACTOR_FLOW= 1.0
GEO_MODE= FUNCTION
GEO_MARKER= (BODY)
GEO_NUMBER_SECTIONS= 5
GEO_ORIENTATION_SECTIONS= Y_AXIS
GEO_LOCATION_SECTIONS= (0.01, 0.738)
GEO_PLOT_SECTIONS= YES
GEO_VOLUME_SECTIONS= 101
EXT_ITER= 5000
CONV_CRITERIA= CAUCHY
CAUCHY_ELEMS= 100
CAUCHY_EPS= 1E-2
CAUCHY_FUNC_FLOW= LIFT
MESH_FILENAME= def_mesh.su2
MESH_FORMAT= SU2
SOLUTION_FLOW_FILENAME= init_flow.dat
OUTPUT_FORMAT= PARAVIEW
CONV_FILENAME= history
BREAKDOWN_FILENAME= forces_breakdown.dat
RESTART_FLOW_FILENAME= solution_flow.dat
SURFACE_FLOW_FILENAME= new_alpha_surface_flow
WRT_SOL_FREQ= 500

APPENDIX C

SUPPLEMENTAL MATERIAL FOR CHAPTER 4

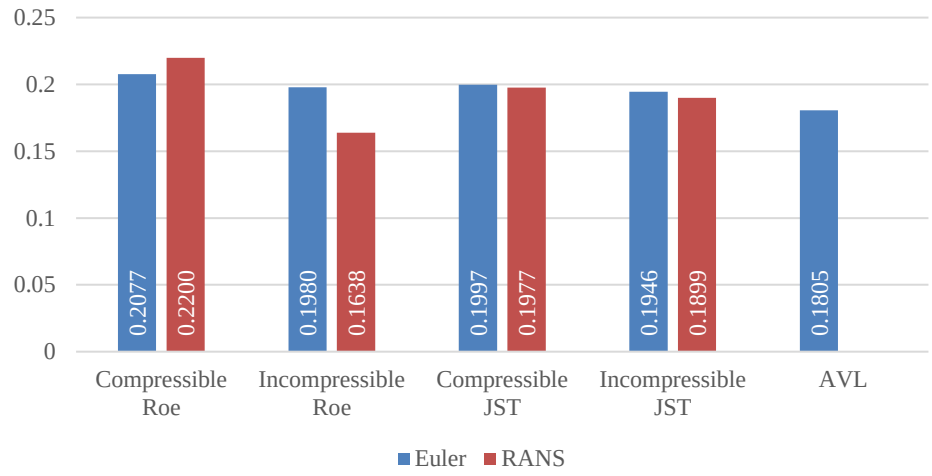

Figure C.1 Lift coefficient data from ONERA M6 simulation in Section 4.3.

The governing equations implemented in SU2 for incompressible flows are shown in Eq. (C.1) and Eq. (C.2) using Einstein notation. In Eq. (C.2) β^2 is the artificial compressibility parameter, δ is the Kronecker delta, and Fr is the Froude number. For more detailed information regarding all governing equations implemented in SU2, see Reference [13].

$$\frac{\partial \boldsymbol{U}}{\partial t} = \nabla \cdot \vec{\boldsymbol{F}}^{c} - \nabla \cdot \vec{\boldsymbol{F}}^{v} = Q \tag{C.1}$$

$$\boldsymbol{U} = \begin{bmatrix} P \\ \rho u_1 \\ \rho u_2 \\ \rho u_3 \end{bmatrix} \quad \vec{\boldsymbol{F}}_i^{c} = \begin{bmatrix} \beta^2 u_i \\ \rho u_i u_1 + P\delta_{i1} \\ \rho u_i u_2 + P\delta_{i2} \\ \rho u_i u_3 + P\delta_{i3} \end{bmatrix} \quad \vec{\boldsymbol{F}}_i^{v} = \begin{bmatrix} \cdot \\ \partial_i u_1 \\ \partial_i u_2 \\ \partial_i u_3 \end{bmatrix} \quad \boldsymbol{Q} = \begin{bmatrix} \vdots \\ \cdot \\ -\dfrac{\rho}{Fr^2} \end{bmatrix} \tag{C.2}$$

APPENDIX D

KITTYHAWK OPTIMIZATIONS

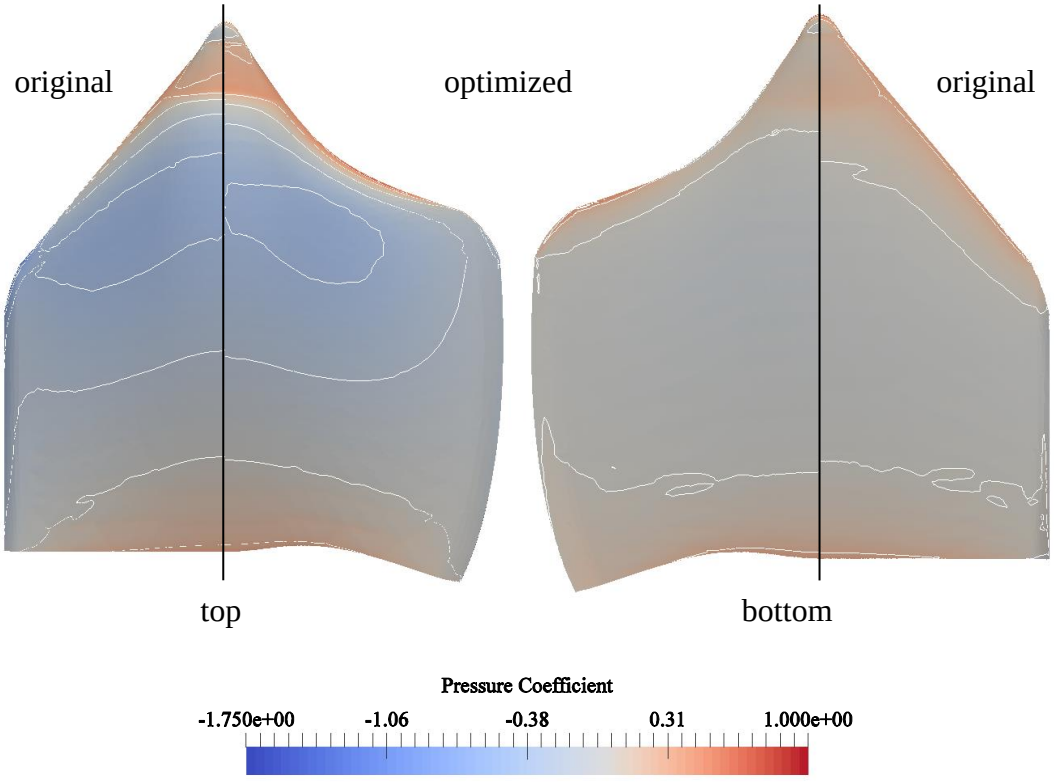

Figure D.1 KittyHawk pressure coefficient comparisons from planform optimization.

(a)

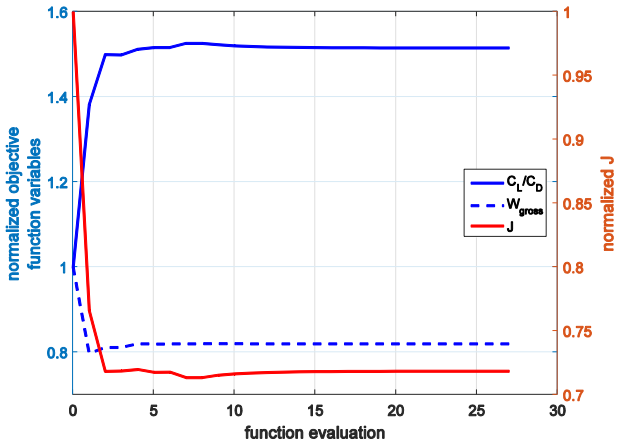

(b)

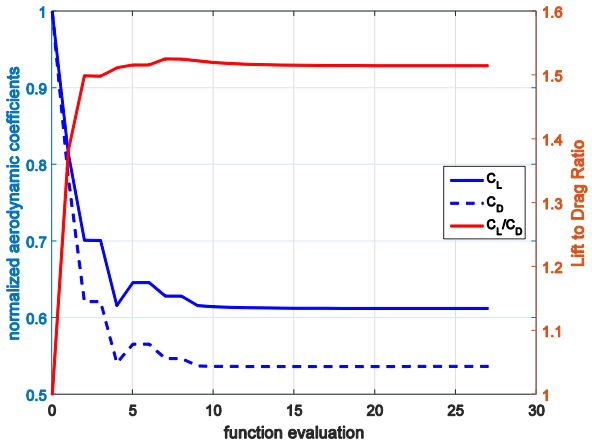

(c)

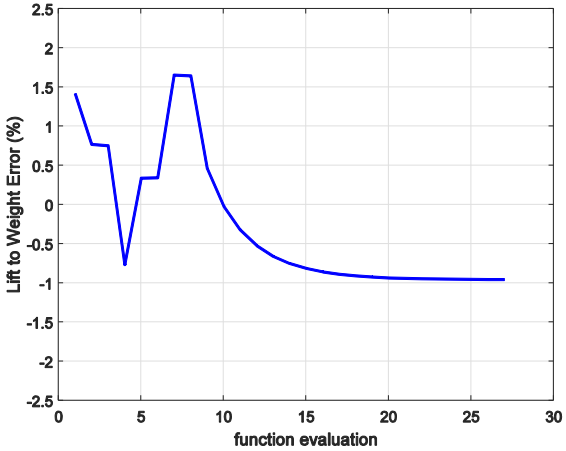

(d)

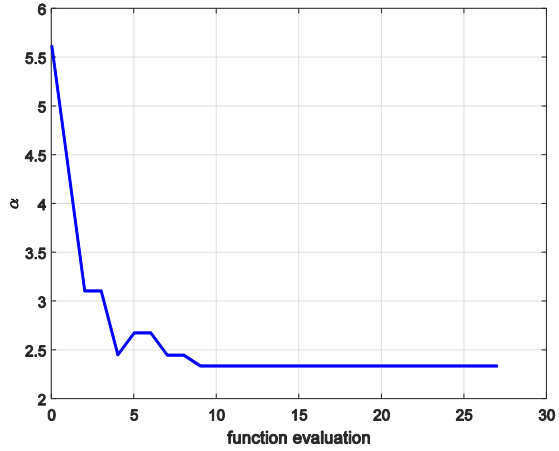

Figure D.2 Optimization results for KittyHawk with three degrees of freedom. (a) Primary optimization results. (b) Aerodynamic coefficients. (c) Consistency error. (d) Angle of attack.

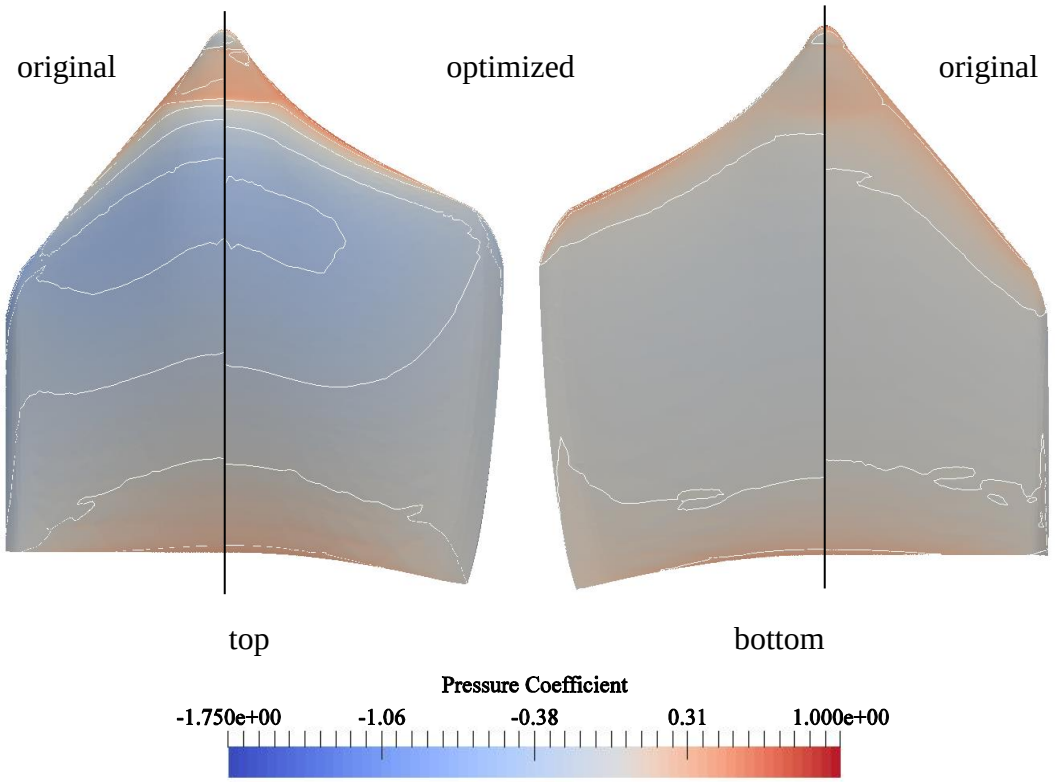

Figure D.3 KittyHawk pressure coefficient comparisons from three-dimensional optimization.

(a)

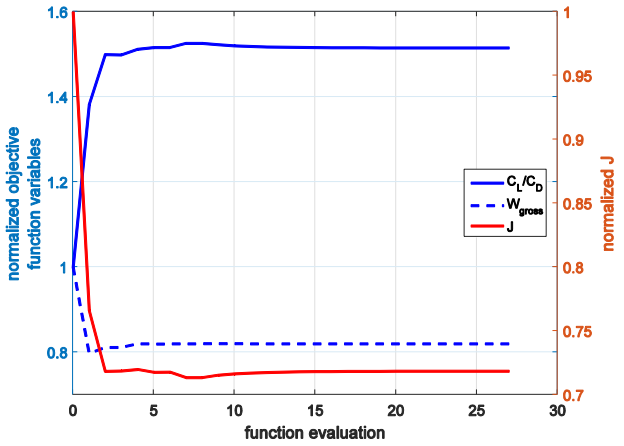

(b)

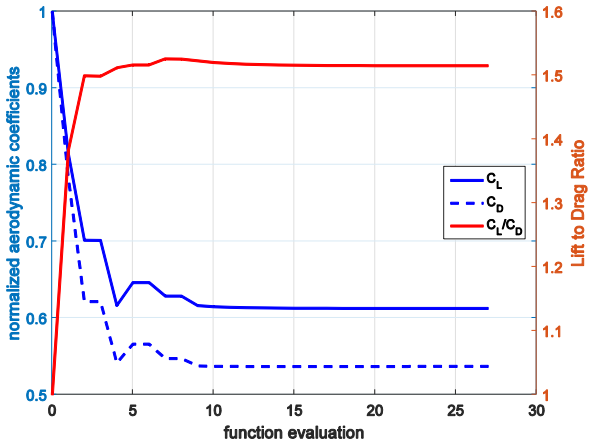

(c)

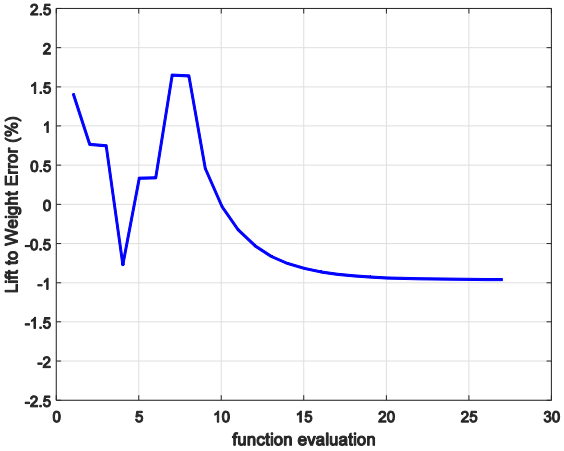

(d)

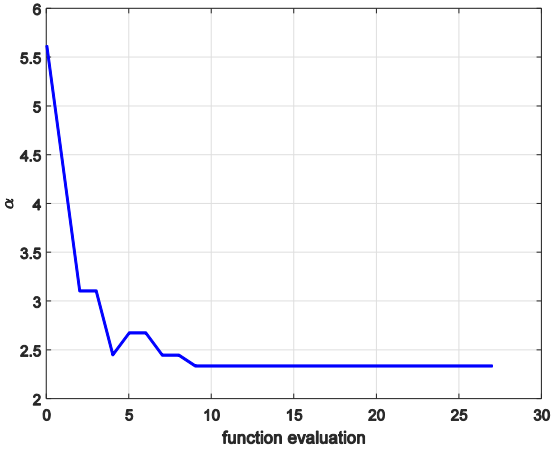

Figure D.4 Optimization results for KittyHawk with airfoil degree of freedom and refined FFD box. (a) Primary optimization results. (b) Aerodynamic coefficients. (c) Consistency error. (d) Angle of attack.

APPENDIX E

ONERA M6 WING OPTIMIZATIONS

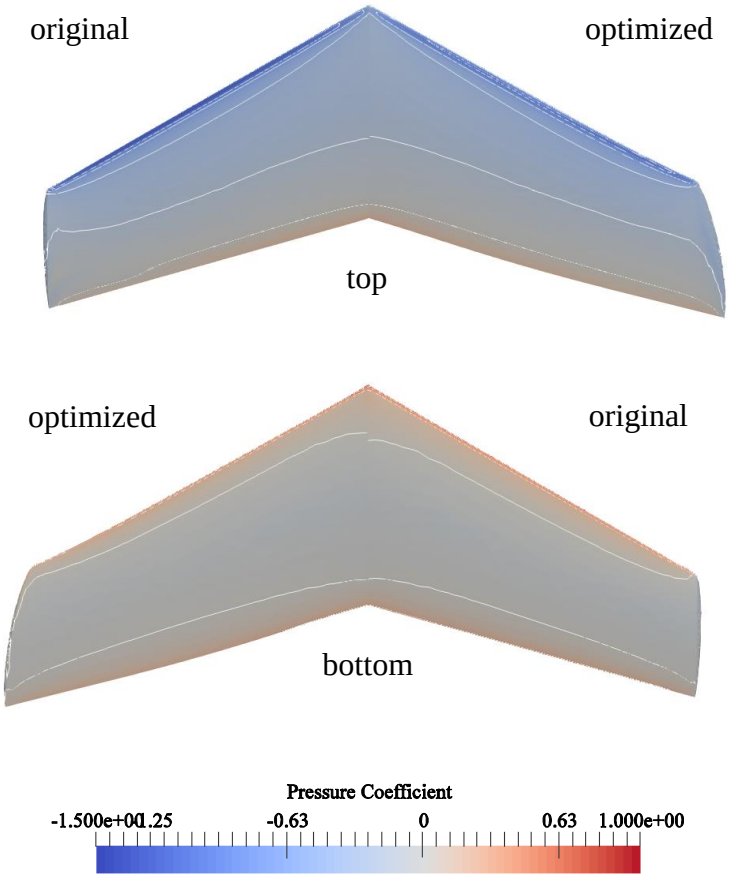

Figure E.1 ONERA M6 pressure coefficient comparisons from planform optimization.

(a)

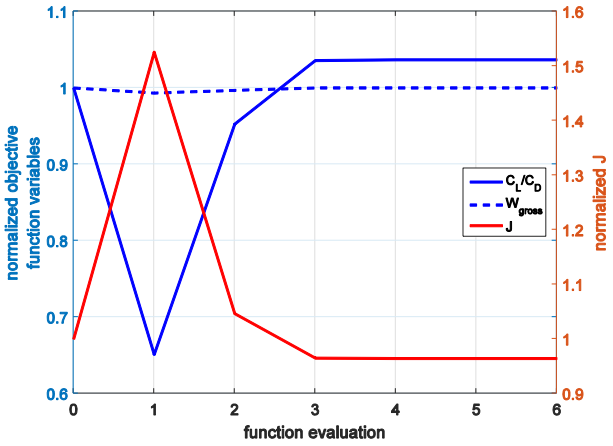

(b)

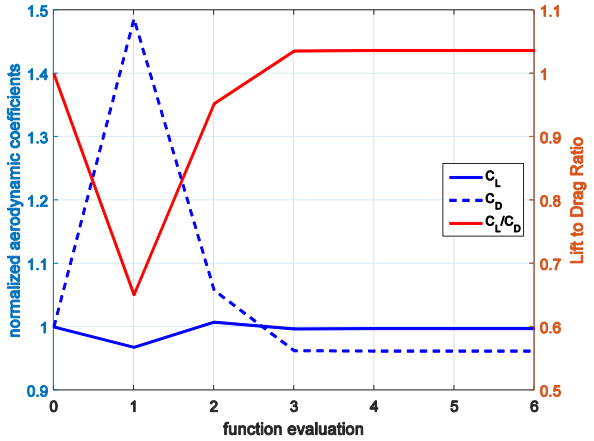

(c)

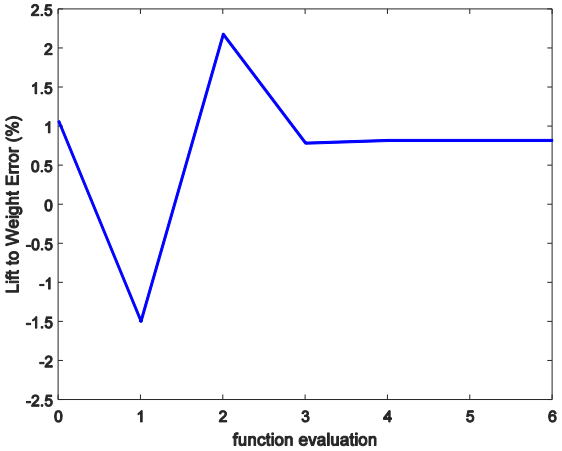

(d)

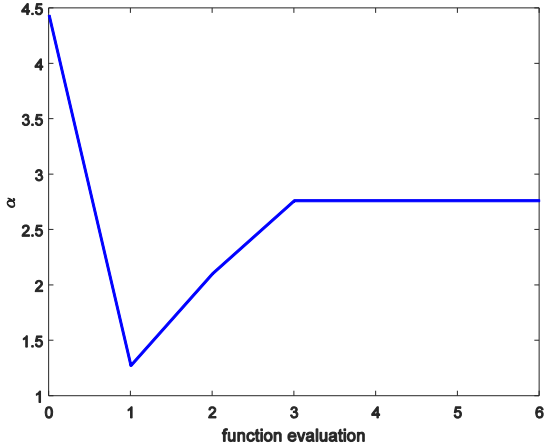

Figure E.2 Optimization results for ONERA M6 with airfoil degree of freedom. (a) Primary optimization results. (b) Aerodynamic coefficients. (c) Consistency error. (d) Angle of attack.

(a)

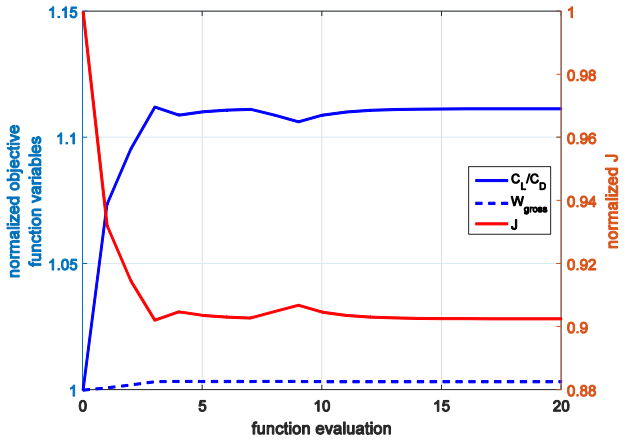

(b)

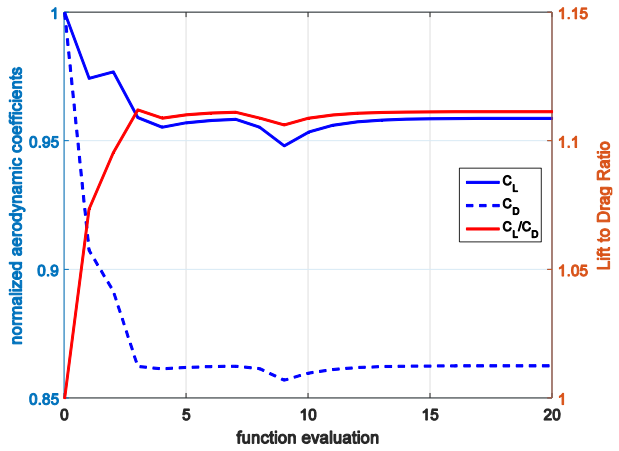

(c)

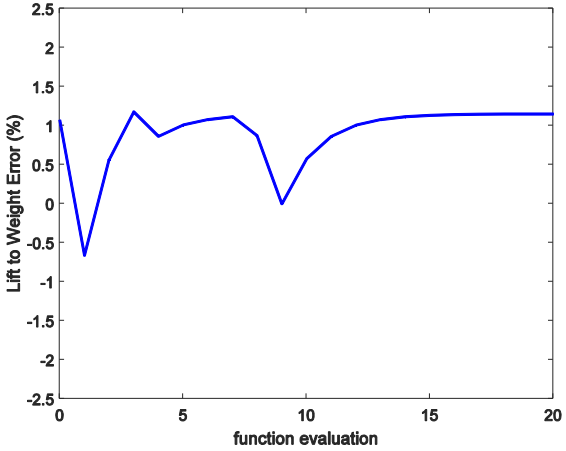

(d)

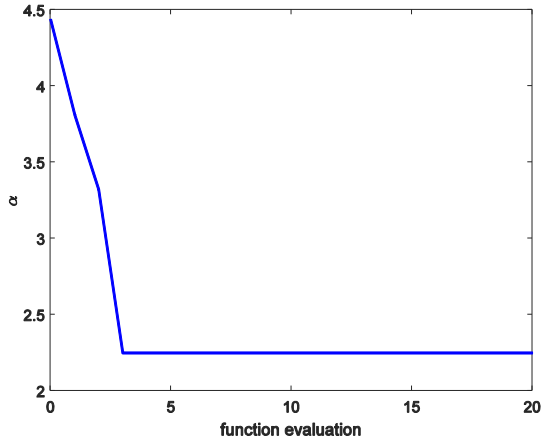

Figure E.3 Optimization results for ONERA M6 with three degrees of freedom. (a) Primary optimization results. (b) Aerodynamic coefficients. (c) Consistency error. (d) Angle of attack.

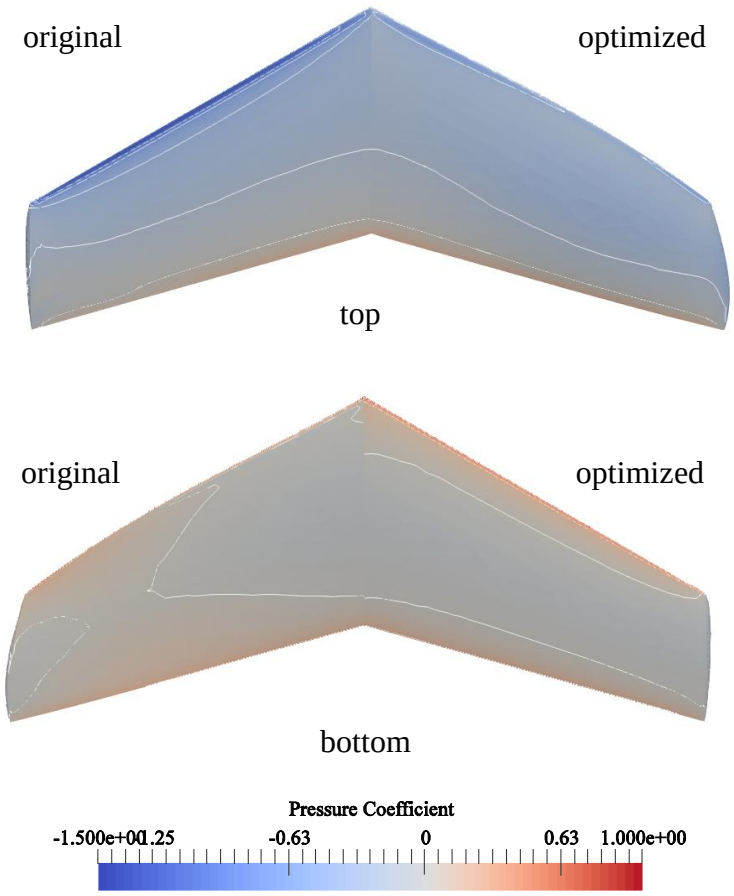

Figure E.4 ONERA M6 pressure coefficient comparisons from three-dimensional optimization.

APPENDIX F

MODIFIED ONERA M6 WING OPTIMIZATIONS

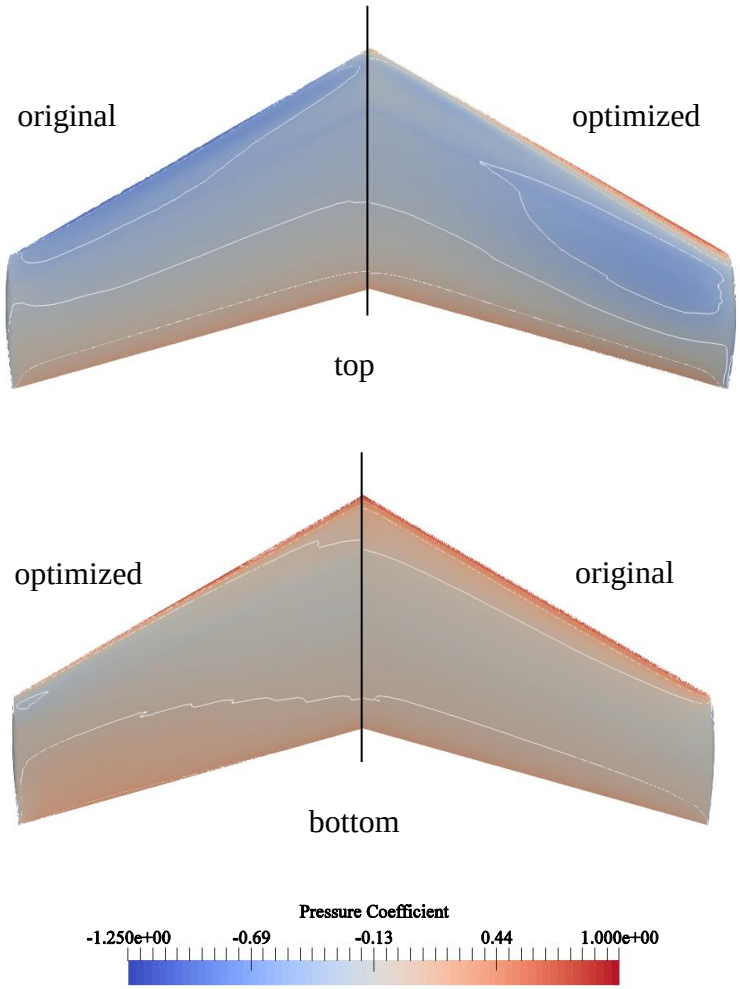

Figure F.1 Modified ONERA M6 pressure coefficient comparisons from airfoil optimization.

(a)

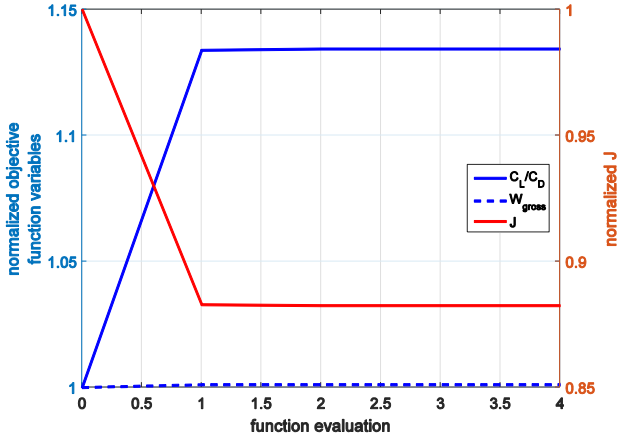

(b)

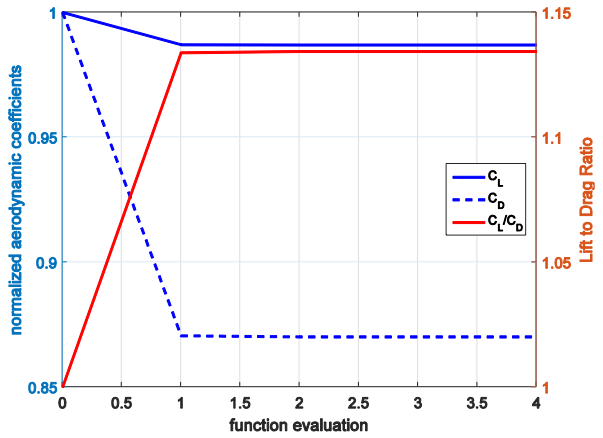

(c)

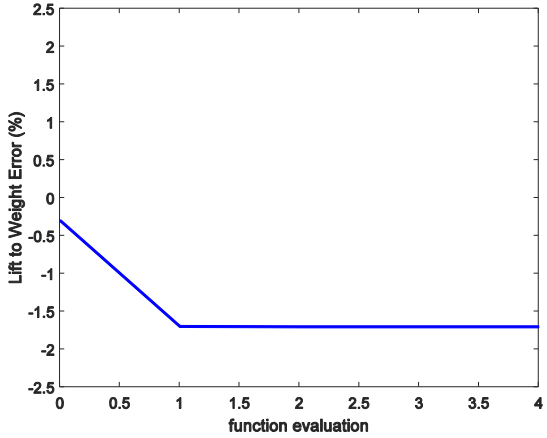

(d)

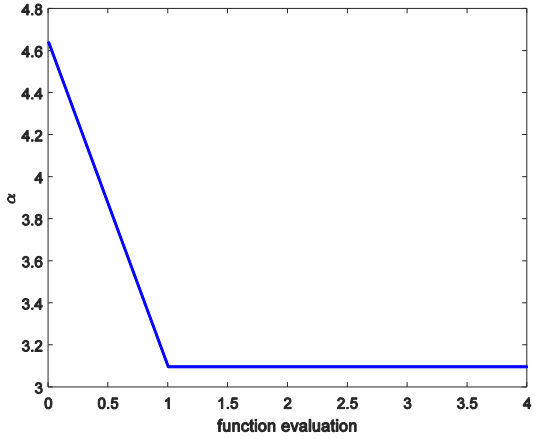

Figure F.2 Optimization results for ONERA M6 with airfoil degree of freedom. (a) Primary optimization results. (b) Aerodynamic coefficients. (c) Consistency error. (d) Angle of attack